

Dynamic DNA Origami-Based Gold Nanoparticle Dimerization:
Design and Assembly of a Hybrid Platform for Nanophotonics

Inaugural-Dissertation zur Erlangung des Doktorgrades

Dr. rer. nat.

der Fakultät für Chemie an der
Universität Duisburg-Essen

vorgelegt von

Michael Erkelenz (M. Sc.)

aus Haan

Dezember 2021

DuEPublico

Duisburg-Essen Publications online

UNIVERSITÄT
DUISBURG
ESSEN

Offen im Denken

ub

universitäts
bibliothek

Diese Dissertation wird via DuEPublico, dem Dokumenten- und Publikationsserver der Universität Duisburg-Essen, zur Verfügung gestellt und liegt auch als Print-Version vor.

DOI: 10.17185/duepublico/75401

URN: urn:nbn:de:hbz:465-20220302-111359-7

Alle Rechte vorbehalten.

Die vorliegende Arbeit wurde im Zeitraum von Oktober 2017 bis August 2021 im Arbeitskreis von Prof. Dr. Sebastian Schlücker am Lehrstuhl Physikalische Chemie I an der Universität Duisburg-Essen durchgeführt.

Tag der Disputation: 07.02.2022

1. Gutachter: Prof. Dr. Sebastian Schlücker, Fakultät für Chemie, Physikalische Chemie
2. Gutachter: Prof. Dr. Barbara Saccà, Fakultät für Biologie, Bionanotechnologie



„[Enim vero.] Non est ad astra mollis e terris via.”

Mod. aus: *Herkules furens* – *Lucius Annaeus Seneca* (1 n. Chr. – 65 n. Chr.)

Zusammenfassung

In den letzten zwei Dekaden führten revolutionäre Entdeckungen und Entwicklungen von neuen Techniken zu einem Paradigmenwechsel auf dem Gebiet der Nanotechnologie. Die einzigartige Interaktion von Edelmetall-Nanopartikeln mit Licht und deren Erforschung und Optimierung ermöglichte die schwingungsspektroskopische Detektion sogar von einzelnen Molekülen. Dies erfordert jedoch die präzise Kontrolle über die Geometrie und Anordnung von Nanopartikeln bis hinunter auf die Sub-nanometer-Ebene. Mit der Entwicklung des DNA-Origami, also dem programmierbaren Ansteuern und Falten von langen DNA -Strängen zu 3D-Formen, wurde dies im Jahr 2006 möglich.

In dieser Arbeit wurde die Entwicklung und Konstruktion einer komplexen nanophotonischen hybriden Plattform für analytische Anwendungen im Bereich der oberflächenverstärkte Raman-Spektroskopie durchgeführt, welche aus drei einzelnen DNA-Origami-Strukturen und zwei Gold-Nanopartikeln besteht. Die Grundlage für die Konstruktion besteht hierbei sowohl aus der Implementierung eines neuen Thiol-basierten Kopplungsweges von Gold-Nanopartikeln (≥ 8 nm) und DNA-Origami als auch der Detergens-basierten Stabilisierung dieser Konstrukte in üblichen Origami-Puffern. Für die nanophotonische hybride Plattform wurden zusätzlich zwei verschiedene DNA-Origami, eine 3D-Origami Box und eine planare dynamische Origami-Plattform, entwickelt und charakterisiert. Die Origami-Box wurden so entworfen, dass nicht nur eine seitenspezifische Funktionalisierung der internalisierten Gold-Nanopartikel, sondern auch eine Dimerisierung der Gold-Nanopartikel mit Nanometer-Präzision möglich ist. Die präzise Dimerisierung durch die dynamische Origami-Plattform wird durch den Austausch von einzelsträngigen DNA-Strängen erreicht, die die beiden Hälften der Plattform zueinander ziehen oder voneinander wegdrücken können.

Summary

Revolutionary discoveries and developments of new techniques have led to a paradigm shift in the field of nanotechnology in the last two decades. The unique interaction of noble metal nanoparticles with light and their exploration and optimization enabled even the vibrational spectroscopic detection of even single molecules. However, this requires precise control over the geometry and arrangement of nanoparticles down to the sub-nanometer level. This became possible in 2006 with the development of DNA origami, the programmable folding and driving of long strands of DNA into 3D shapes.

In this work, the development and construction of a complex nanophotonic hybrid platform for analytical applications in the field of Raman spectroscopy was carried out. The platform consists of three single origami and two gold nanoparticles. The basic idea of the design relies on the implementation of a new thiol-based coupling strategy for the attachment of gold nanoparticles (≥ 8 nm) to DNA origami structures as well as the detergent-based stabilization of these complexes in commonly used DNA origami buffers. For the nanophotonic hybrid platform, two different origami shapes, a 3D DNA origami box and a planar dynamic platform, were developed and characterized. The origami box was designed to allow not only site-specific functionalization of the internalized gold nanoparticles, but also dimerization of the gold nanoparticles with nanometer precision. Precise dimerization using the dynamic origami platform is achieved by the exchange of single-stranded DNA strands that can move the two halves of the platform toward or away from each other.

Table of Contents

Zusammenfassung	vi
Summary	vii
List of Abbreviations.....	x
List of Physical Parameters.....	xiii
List of Figures.....	xiv
List of Tables.....	xvi
List of Equations	xvii
1. Introduction and Aim of the Work	1
2. Theoretical Background	4
2.1. Plasmonically Active Gold Nanoparticles	4
2.1.1. Optical Properties of Materials on the Nanoscale Leading to Surface Plasmon Resonance.....	5
2.1.2. Plasmon Hybridization Model	9
2.2. DNA and DNA Nanotechnology	11
2.2.1. DNA Origami.....	13
2.3. Plasmonic Hybrid Materials.....	17
3. Material and Methods	22
3.1. Materials.....	22
3.2. Synthesis of Gold Nanoparticles	22
3.2.1. Spherical Gold Nanoparticles (AuNP)	22
3.2.2. Gold Nanocubes (AuNC).....	23
3.3. Functionalization of Gold Nanoparticles.....	24
3.3.1. Ligand Exchange	24
3.3.2. ssDNA.....	25
3.4. Computer-Aided Design of DNA Origami.....	25
3.4.1. Pandora's Box	26
3.4.2. Zelos Dynamic Platform	28
3.4.3. Hybridization of Pandora's Box onto Zelos	30
3.5. Assembly of DNA Origami	31
3.6. Incorporation of Gold Nanoparticles into Pandora's Box	32
3.7. Analysis and Purification Methods.....	33
3.7.1. UV-Vis Absorption Spectroscopy.....	33
3.7.2. Transmission Electron Microcopy (TEM).....	34
3.7.3. Agarose Gel Electrophoresis (AGE).....	34

4. Results and Discussion	36
4.1. Finite Difference Time Domain (FDTD) Simulations of Electrical Field Enhancements in AuNP and AuNC Dimers	36
4.1.1. Surface-Enhanced Raman Scattering	37
4.2. Synthesis and Characterization of AuNP/AuNC with Different Size, Shape and Surface Functionalization	42
4.2.1. Spherical Gold Nanoparticles.....	42
4.2.2. Gold Nanocubes	44
4.2.3. Functionalization and Characterization.....	47
4.3. Colloidal Stability of Gold Nanoparticles in Origami Buffer Systems with High Ionic Strength and Its Enhancement by Surface-Active Molecules.....	50
4.4. Assembly of Pandora’s Box.....	55
4.5. Incorporation of Gold Nanoparticles and Gold Nanocubes with Different Sizes in Pandora’s Box	60
4.5.1. Incorporation via Hybridization.....	60
4.5.2. Incorporation via Thiol Chemistry.....	63
4.6. Purification of Gold Nanoparticle-Origami Conjugates	65
4.7. Zelos Assembly and Characterization	68
4.7.1. Characterization of the Dynamics	70
4.8. Assembly of the Origami Superstructure and the Nanophotonic Platform	74
4.8.1. AuNP Dimerization with Pandora hybridized onto Zelos	76
5. Conclusion and Outlook	79
6. References	81
A. Appendix	94
I. Supplementary Information	94
II. Lists of Equipment, Materials and Chemicals.....	107
III. List of DNA Sequences.....	109
a. Staple Strand Sequences	109
b. Scaffold Strand Sequence.....	122
B. Acknowledgements	125
C. List of Publications and Poster Presentations	126
D. Curriculum Vitae	128
E. Declaration	130

List of Abbreviations

Table 1: List of used abbreviations

%	Percentage
λ_{\max}	Wavelength of the (plasmon) peak
2D	Two-Dimensional
3D	Three-Dimensional
A4F	Asymmetric-flow field-flow fractionation
AA	Ascorbic acid
AFM	Atomic force microscopy
AGE	Agarose gel electrophoresis
AuNC	Gold nanocubes
AuNP	Gold nanoparticles
b(s)	Base(s)
bp(s)	Base pair(s)
BSPP	Bis(p-sulfonatophenyl)phenylphosphine dihydrate dipotassium salt
c	concentration
CCD	Charge coupled device
CTAB	Cetyltrimethylammonium bromide
d	days
DGC	Density gradient centrifugation
Di-water	Deionized water
DNA	Desoxyribonucleic acid
ds	Double-stranded
EDTA	Ethylendiamintetraacetat
EF	Enhancement factor
e.g.	Example given
et al.	<i>Et alii</i>
EtBr	Ethidium bromide
FAM	6-Carboxyfluorescin
FDTD	Finite difference time-domain
Fig.	Figure

List of Abbreviations

h	Hours
HAuCl ₄	Tetrachloroauric acid
H ₂ O	Water
k	Kilo (10 ³)
L	Liter
LSP(R)	Localized Surface Plasmon (Resonance)
m	Milli (10 ⁻³) / Meter
min	Minutes
M	Molar (mol/L)
MΩ	Megaohm
MeOH	Methanol
M-FRET	Metal-enhanced Förster resonance energy transfer
MgCl ₂	Magnesium Chloride
n	Nano (10 ⁻⁹)
NaCl	Sodium chloride
NaBH ₄	Sodium borohydride
OD	Optical density
o.n.	Over night
PBS	Phosphate buffered saline
PEG	Polyethylene glycol
PSS	Polystyrene sulfonate
rcf	Relative centrifugal force
RT	Room temperature
Scaffold	p8064 phage genome derivate
SERS	Surface-enhanced Raman scattering
ss	Single-stranded
Tab.	Table
TAMRA	Tetramethylrhodamine
TCEP	Tris(2-carboxyethyl)phosphine
TEM	Transmission Electron Microscopy
TRIS	Tris(hydroxymethyl)aminomethane
UV	Ultraviolet

List of Abbreviations

V	Volt
Vis	Visible spectrum (380-750 nm)
μ	Micro

List of Physical Parameters

Table 2: List of used physical parameters

0 °C	0 Degree Celsius	273,15 K
Da	Unified atomic mass in <i>Dalton</i>	$1.661 \cdot 10^{-27}$ kg
V	Voltage	$(\text{kg} \cdot \text{m}^2) / (\text{A} \cdot \text{s}^2)$
t	Time	s

List of Figures

Figure 1: Photographs of the <i>Lycurgus cup</i>	4
Figure 2: Scheme of localized surface plasmon resonance in a gold nanoparticle.....	6
Figure 3: Spherical gold nanoparticle with excited plasmon and induced dipole based on the quasi-static model.	7
Figure 4: Effect of the size and the surrounding medium, either being polar or non-polar, on the dipolar charge distribution affecting the overall LSPR energy.....	9
Figure 5: Plasmon hybridization model for a dimer of spherical gold nanoparticles in the quasi-static approximation.	10
Figure 6: Structure of the DNA double helix according to the Watson-Crick base-pairing.	12
Figure 7: First approach of short oligonucleotides for creation of artificial DNA nanobiotechnological structures.	13
Figure 8: Scaffold-based DNA origami concept.....	14
Figure 9: Possible DNA origami packing motives and cross-over rules.	16
Figure 10: Early published hybrid nanostructures for SERS.....	18
Figure 11: Advanced hybrid nanostructures for metal-enhanced FRET (M-FRET) and SERS nanolenses.	19
Figure 12: Recently published hybrid materials for biomedical applications and single-molecule SERS detection.	21
Figure 13: Schematic representation of AuNP synthesis	23
Figure 14: Schematic representation of the synthesis of ultra-small AuNC	23
Figure 15: Schematic representation of AuNC synthesis	24
Figure 16: Scheme of Pandora's box design.	27
Figure 17: Scheme of the dynamic DNA origami platform called Zelos.....	28
Figure 18: Scheme of the toehold-mediated strand displacement of Zelos.....	30
Figure 19: Hybridization concept of Pandora's box onto Zelos.	31
Figure 20: Scheme of the thermal annealing ramp	32
Figure 21: FDTD simulations of SERS enhancement factors $ E_{loc4} $ of 18 nm AuNC dimers.....	39
Figure 22: FDTD simulations with resulting SERS enhancement factors $ E_{loc4} $ of 18 nm AuNP dimers	40
Figure 23: Representative TEM images of AuNP with different sizes.....	44
Figure 24: Representative TEM images of AuNC with different sizes.....	46
Figure 25: TEM images of 10 nm AuNP with different surface modifications.....	49
Figure 26: UV-Vis extinction spectroscopic for probing colloidal stability.....	51
Figure 27: Molecular structure and charges of surfactants (CTAB, SDS, Tween20) and surface-active molecules (BSPP, citrate).....	54
Figure 28: Magnesium-screening of Pandora's box assembly.....	56
Figure 29: TEM images of negatively stained Pandora's boxes	57
Figure 30: Staple-screening of Pandora's box assembly.....	59
Figure 31: Incorporation of 10 nm AuNP into Pandora's box by base hybridization.	62
Figure 32: Internalization of gold nanoparticles with different sizes and shapes into Pandora's box.	64
Figure 33: TEM images of unpurified colloids after conjugation	65
Figure 34: AGE purification and TEM imaging of nanoparticle-origami conjugates.....	67
Figure 35: Magnesium screening of Zelos.....	69
Figure 36: Characterization of Zelos dimensions (43 bp and 0 bp distance).	70
Figure 37: Characterization of Zelos' dynamic properties.	71
Figure 38: FRET-based determination of the variation in Zelos' gap size.....	73
Figure 39: Hybridization of Pandora's Box onto Zelos.....	75

Figure 40: Representative TEM images of AGE-purified Pandora's box-AuNP..... 77

Figure 41: TEM images of the three different species appearing during hybridization of Pandora's box-AuNP conjugates onto Zelos. 78

List of Tables

Table 1: List of used abbreviations.....	x
Table 2: List of used physical parameters.....	xiii
Table 3: Incorporation yields of differently sized and shaped gold nanoparticles into Pandora’s box via thiol chemistry.....	64
Table 4: List of used equipment.....	107
Table 5: List of used consumables.....	107
Table 6: Chemicals & reagents.....	107
Table 7: Buffer solutions.....	108

List of Equations

(1) Complex frequency-dependent dielectric function	6
(2) Description of the plasma frequency by using the Drude parameters.....	7
(3) Clausius-Mossotti relation	7
(4) Resonance condition for dipole excitation in a metal nanoparticle	8
(5) Beer-Lambert law.....	33
(6) Local refractive index description	48
(7) Derjaguin-Landau-Verwey-Overbeek theory for two equally sized spherical particles	52

1. Introduction and Aim of the Work

Parts of the following chapter will be published in chapter one (*Fundamentals of Nanobiophotonics for Diagnostics and Therapy*) of volume 5 of the series: *World Scientific Reference on Plasmonic Nanomaterials* (2022, World Scientific Publishing Company). [1]

Nanotechnology means the manipulation of matter on the nanoscale and was intentionally mentioned for the first time in Richard Feynman's famous talk *There's plenty of room at the bottom* at Caltech in 1959. [2] This talk pioneered revolutionary ideas, such as the miniaturization and building of small machines for the physical manipulation of single atoms at the nanoscale. With about half a century anticipation, Feynman predicted the advantages as well as the challenges of chemistry and physics on the nanoscale and how they can impact applied sciences. The prefix "Nano" comes from the Greek word *νάνος* (*nános*) which means dwarf and is one in a billion of a given physical quantity. Transferred to meter, this means 1 nm is equivalent to 10^{-9} m. The term *nanotechnology* itself was defined and used the first time in 1974 by Norio Taniguchi [3] and it became known to a wide audience through Eric Drexler in 1986 [4].

Nowadays, nanotechnology has arrived in multiple scientific fields like supramolecular chemistry, molecular biology, and biomedicine and even in commercial products of our everyday life. [5-8] Prominent examples are catalysts in cars, titanium dioxide nanoparticles in sunscreen, antimicrobial materials imprinted with silver nanoparticles or gold nanoparticles (AuNP) visible as colored band in pregnancy tests. [9, 10] This wide range of applications is based on the unique physicochemical properties of materials at the nanoscale. [11] These special properties are the result of surface effects that - at nanosized regimes - become dominant with respect to the bulk state. For example, when considering the surface-to-volume ratio of a nanoparticle, this value increases with decreasing diameter, meaning that a nanoparticle of 20-100 nm size exhibits less than 20 % of all atoms at the surface, whereas a smaller nanoparticle 1-2 nm in size displays up to 50 % of all its atoms at the surface. [12] Especially, noble metal nanoparticles like gold or silver are used in applied sciences due to their unique interaction with light resulting in special optical properties. These special features are mainly derived by the so called *plasmonic* behavior of AuNP. Light irradiation of a gold nanoparticle can induce a collective oscillation of the conductive band electrons if the frequency of the incident light is resonant to the plasma frequency of the nanoparticle. This oscillation leads to various effects including changed light absorption and scattering from the particle itself but also from molecules on its surface. Plasmonic effects are utilized for catalysis, sensing of analytes and more. Especially, the vibrational spectroscopic

detection of molecules based on their light scattering properties can be enhanced by factors up to 10^{11} using plasmonic gold nanoparticles. [13]

To return to the visionary talk of Feynman, one of his main questions was: *how can we manipulate materials or even atoms on the nanoscale?* A possible solution to this problem relies on the rearrangement of atoms by *tiny hands*. Today several methods exist for manipulating objects at the atomic scale, including the atomic force microscope (AFM), scanning tunneling microscopy (STM) and optical tweezers. [14] Today typically two approaches of generating nanosized objects are used, namely, the *top-down* and the *bottom-up* approach. *Top-down* strategies are based on bulk materials and reducing their size by grinding, milling, or ablating of nanostructures by using laser light. Also, the imprinting of structures and information in bulk materials with resulting nano-effects by using photolithography falls into this category. *Bottom-up* strategies are based on the self-assembly of atoms or nanoparticles into complex structures with emergent properties. The nucleation of a solution of metal ions into metal nanoparticles using either physical or chemical driving forces is a classic example of such a strategy.

As we can now generate nanosized objects with unique and beneficial properties, the next question to address is how we can manipulate these objects. One promising solution relies on the use of DNA nanotechnology. [15] As widely known, the DNA molecule is the depositary of the genetic information encoded in our cells in the form of four nucleobases, namely, the purines adenine (A) and guanine (G) as well as the pyrimidines thymine (T) and cytosine (C) [16]. The main feature of the DNA molecule is its programmability. Indeed, given a strand of a certain sequence, the complementary strand that is required to form the double helix is uniquely defined by the base-pairing rule, which states that A binds to T and G binds to C (and vice versa). DNA nanotechnology builds on this simple idea to realize DNA objects in a predictable fashion and with a level of sophistication that has been particularly boosted after the invention of the DNA origami method in 2006 by Paul Rothemund. [17] Especially in the last decade, complex nano-scaled hybrid structures consisting of DNA origami and specifically arranged AuNP were designed and assembled. These plasmonic hybrid nanomaterials provide new tools for basic scientific research at the nanoscale and enable unique control over the properties of plasmonic materials.

The objective of this thesis is the design, assembly, and characterization of a hybrid plasmonic platform for nanophotonic applications. In fact, the designed hybrid structure consists of three different DNA origami, two 3D origami boxes and one 2D rectangular dynamic breadboard (about 15 MDa in total), as well as two spherical gold nanoparticles (AuNP) or cubic gold nanoparticles (AuNC). First, computational FDTD simulations were used to evaluate the generated plasmonic effect with respect to the enhanced scattering of a molecule placed on the detection side of the hybrid platform (Section

4.1). Next, AuNP and AuNC with different sizes were synthesized, characterized, and functionalized for their incorporation in the hybrid platform (4.2). Since, the optimal conditions for gold nanoparticle (low ionic strength) and DNA origami (high ionic strength) handling are exactly the opposite, section 4.3 covers the stabilization of AuNP in DNA origami buffer systems by using surface-active molecules. The design and assembly of the DNA origami boxes used in this thesis (herein referred to as Pandora's box) is described in section 4.4 followed by the incorporation of the differently sized and functionalized gold nanoparticles using the widely used base hybridization approach as well as a new developed thiol chemistry-based approach (section 4.5). After successful incorporation of gold nanoparticles, the resulting structures must be purified for further hierarchical assembly into high-order structures as described in section 4.6. Two AuNP are then installed onto a planar DNA origami breadboard and their mutual distance is controlled in a dynamic fashion through a DNA-based region (section 4.7). The final section of this thesis is about the assembly of the whole DNA origami super structure with and without AuNP and determination of the final structure yield (section 4.8).

2. Theoretical Background

Parts of the following chapter will be published in chapter one (*Fundamentals of Nanobiophotonics for Diagnostics and Therapy*) of volume 5 of the series: *World Scientific Reference on Plasmonic Nanomaterials* (2022, World Scientific Publishing Company). [1]

In this chapter, the fundamentals of materials on the nanoscale with focus on gold nanoparticles and their intrinsic plasmonic properties are described (section 2.1). Furthermore, section 2.2 will give a short overview about the history of DNA nanotechnology and the development of DNA origami in the last two decades. Finally, plasmonic hybrid materials with different applications developed in the last years will be described.

2.1. Plasmonically Active Gold Nanoparticles

Spherical gold nanoparticle colloids are, in contrast to the bulk form, not yellowish but reddish in color. This property of gold nanoparticle colloids is perhaps the most impressive effect of gold at the nanoscale at the first glance. However, behind this oddity, used since ancient times, there is much more than meets the eye. A famous example for their ancient use is the Lycurgus cup manufactured by the late Romans in the 4th century. Perhaps accidentally, gold nanoparticles with a size between 50 and 100 nm were embedded in the glass giving rise to this impressive dichroic effect. The color of this cup illuminated from behind is red, whereas the cup appears greenish if illuminated from the front. Anyway, it is not known if this dichroic effect was intentionally evoked or not and how the ancient goldsmith achieved this. [18]



Figure 1: Photographs of the Lycurgus cup. The cup was manufactured in the 4th century by the late Romans and was photographed with light coming from behind (left) and from front (right). Special color properties of the glass are derived by light scattering (green) and light absorption (red) of embedded gold nanoparticles. (British Museum, London, Creative Common license BY-NC-SA 4.0)

Since Michal Faraday synthesized gold nanoparticles in a controlled manner in 1857 and described the product of his synthesis as “a beautiful ruby or amethystine fluid” by using a “weak solution of gold [. . .] and a little of phosphorus in ether” multiple bottom-up approaches have been developed and the reaction mechanisms has been investigated. [19] However, he was the first who recognized the reduction of solubilized gold to exceedingly fine particles suspended in a liquid phase. Beside his wet chemical synthesis, his main interest was in the color and thus the special optical properties of colloidal gold nanoparticles at the nanoscale.

2.1.1. Optical Properties of Materials on the Nanoscale Leading to Surface Plasmon Resonance

For the rational design of a complex plasmonic nanostructure the optical properties of materials on the nanoscale must be considered as also small changes can have big impact on the resulting structure. Especially, the plasmonic properties of nanoparticles have been physically described before and can be simulated to estimate the final plasmonic behavior. The optical properties of noble metal materials on the nanoscale with respect to their scattering and absorption is visible as colored appearance and has been theoretically described for the first time by Gustav Mie in 1908. [20] In his pioneering work, he developed the theory for a plane electromagnetic wave interacting with a spherical nanoparticle. In fact, this was the first mathematical formulation of the scattering and absorption of spherical nanoparticles which are the key parameters for the field of *plasmonics*. The term *plasmonics* is a hybrid of plasma oscillation and electronics. [21] A plasmon is a quasi-particle formed by the interaction of an electromagnetic wave with a noble metal surface or a noble metal particle as shown in **Figure 2**. In particular, the incident light interacts with the overall conduction band electrons, in case of gold, specifically the delocalized 6s electrons. In case of a metal surface, the plasmon can propagate along the interface of the conductor and the dielectric medium, whereas in case of a metal nanoparticle non-propagating electron density waves are generated. The first case is called *surface plasmon*, although the latter is called *localized surface plasmon* (LSP). The excitation of the electrons takes place when the frequency of the incident light ω is resonant to the plasma frequency ω_p of the metal $\omega = \omega_p$.

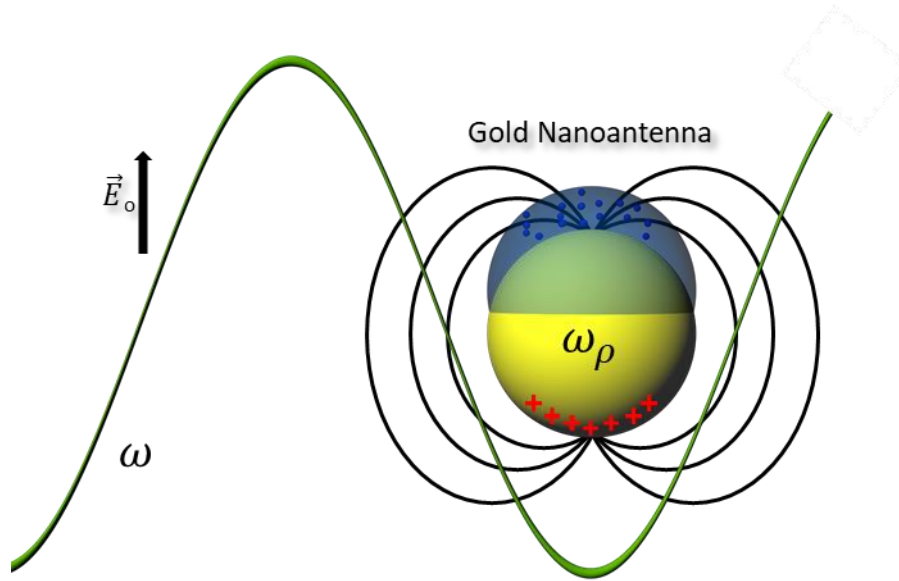


Figure 2: Scheme of localized surface plasmon resonance in a gold nanoparticle. The incident electromagnetic wave ω interacts with the gold nanoparticle at resonant conditions ($\omega = \omega_p$) leading to a driven, damped collective oscillation of the conduction band electrons. This collective oscillation is called a plasmon. The formation of a dipole lead to induction of a local electromagnetic field around the nanoparticle.

To understand this excitation and the origin of the plasma frequency of gold nanoparticles we must consider the overall behavior of electrons in a noble metal crystal lattice. In 1900, Paul Drude was able to transfer the theory of gases to metals and established the term *electron gas*. [22] He defined electrons as freely moving point-like charge carriers within a crystal lattice of positive counter ions. These free moving charges, called a plasma, and their behavior was mathematically described by Drude. As mentioned before, the freely moving electrons of a conductive metal are called conduction electrons and are by its nature delocalized. They cannot be assigned to distinct lattice ions and can interact with electromagnetic waves as described within the framework of classical Maxwell equations. [23, 24] With the Drude model, the optical properties of bulk materials can be described by using the frequency-dependent relative permittivity $\epsilon_r(\omega)$. The relative permittivity is a material-specific quantity which describes the decrease of an electric field by a dielectric medium, for example, between the two plates of a capacitor compared to vacuum. With the complex frequency-dependent dielectric function $\epsilon(\omega) = \epsilon_r \epsilon_0$, many properties of metals can be described. Incident electromagnetic irradiation results in the driven, damped harmonic oscillation of the electron gas system. Within the Drude model the dielectric function can be expressed as:

$$\epsilon(\omega) = \epsilon_\infty - \frac{\omega_p^2}{\omega(\omega + i\gamma)} \quad (1) \text{ Complex frequency-dependent dielectric function}$$

where γ is the relaxation rate (damping process), ω_p the plasma frequency and ω the frequency of the incident electromagnetic wave. The contribution of the conduction band electrons as well as the valence electrons is implemented by ϵ_∞ and should be 1 if only the free moving conduction band electrons are involved in the oscillation. The plasma frequency of a metal, which means the excitation of the conduction band electrons by incident light resulting in an oscillation, can be derived by using the Drude parameters:

$$\omega_p = \sqrt{ne^2/\epsilon_0 m}$$

(2) Description of the plasma frequency by using the Drude parameters

with n and m being the density and effective mass of the conduction band electrons, respectively.

With this description of the plasma frequency origin using the Drude model and the model of a driven, damped harmonic oscillation, the nature of a generated plasmon can be understood. If resonant conditions are present, the incident electromagnetic wave leads to the formation of the LSP and thus to the formation of a dipole moment proportional to the electromagnetic field. In gold colloids, the resonant excitation of the LSP at the plasma frequency ω_p falls into the visible region (350–700 nm, $\sim 10^{14}$ – 10^{15} Hz), giving rise to their reddish color. In the case of gold nanoparticles much

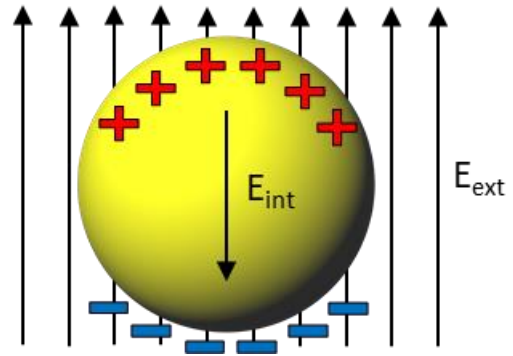


Figure 3: Spherical gold nanoparticle with excited plasmon and induced dipole based on the quasi-static model.

smaller than the incident resonant light, the phase of the oscillating electromagnetic field is nearly constant over the nanoparticle. Due to this constant phase, the *quasi-static approximation* as schematic shown in **Figure 3** within the Clausius-Mossotti relation can be used to describe the polarizability of a gold nanoparticle with radius R :

$$\alpha = \epsilon_0 3V \frac{\epsilon_r - 1}{\epsilon_r + 2}$$

(3) Clausius-Mossotti relation

This expression also contains the dielectric function of the sphere relative to the surrounding medium $\epsilon_r = \epsilon'_r + i\epsilon''_r = \epsilon_{metal} / \epsilon_{medium}$ and the sphere volume V . Resonance occurs for:

$$Re(\epsilon_r) = \epsilon'_r = -2 \quad (4) \text{ Resonance condition for dipole excitation in a metal nanoparticle}$$

The overall penetration depth of electromagnetic waves into metal in the visible spectrum is around 25 nm. If resonant conditions as described before are given, the free electron gas or plasmon starts to oscillate. However, if the frequency of the incident light is higher than the plasma frequency ($\omega_p < \omega$), the electrons are not able to react fast enough due to their inertia, and the light is transmitted. Contrary, if the frequency of the incident light is lower than the plasma frequency ($\omega_p > \omega$), the electrons screen the electromagnetic field, resulting in the reflection of the light.

As mentioned before, the plasma oscillation lifetime is limited because of multiple damping processes. Decay channels can be radiative or non-radiative damping mechanisms, respectively, which lead to a plasmon lifetime of around ~ 10 fs. Radiative damping is a scattering process where the incident electromagnetic wave is re-emitted with the same wavelength (elastic scattering). Elastic scattering of light by nanoparticles is used in nanoparticle-based diagnostics, e.g., correlated darkfield microscopy and optical coherence tomography. [25] Conversely, non-radiative damping mechanisms are based on light absorption followed by Landau damping, electron-electron scattering and electron-phonon coupling. The generated phonons, which are quasi-particles of the lattice vibrations, can dissipate their energy via interaction with molecules of the surrounding medium. It is noteworthy, that also these effects are used in current therapeutic approaches like the photothermal therapy based on gold nanorods. [26-28] Anyway, beside the reduced lifetime of the plasmon, the damping processes also lead to a decreased mean free path of an electron inside the metal to ~ 50 nm. [5]

Beside the impact of the incident light as well as material-dependent constants for plasmon formation or damping processes which influence the plasmon lifetime, also the size, geometry, and environment of the plasmonic nanoparticle are important parameters. These key parameters affect the location of the LSPR mode in the electromagnetic spectrum. For each case, the underlying effect can be attributed to the restoring force after formation of the dipole and described by Coulomb's law as shown in **Figure 4**. The restoring force is proportional to the product of the charges, namely the delocalized electrons and the positive charged atomic cores, and inversely proportional to the square of the distance between the charges inside the nanoparticle. [29, 30] A smaller restoring force results in a

larger resonance frequency and accordingly a larger excitation wavelength. With decreasing particle size a shift of the LSPR mode to smaller wavelength is visible due to the higher restoring force. It has to be mentioned here, that also the geometry plays an important role in the formation of the plasmon, since additional oscillation axes (e.g., gold nanorods) lead to the appearance of additional plasmon modes in absorption spectra of colloids.

Likewise the size, also the environment around the nanoparticle affects the location of the LSPR mode in the electromagnetic spectrum. [31] Transferring AuNP from a non-polar dispersion medium, e.g. cyclohexane (refractive index $n = 1.43$), to a polar medium, e.g. dimethyl sulfoxide (refractive index $n = 1.48$), consequently shift the plasmon mode from 520 nm to 542 nm as shown experimentally. [31] Similarly, to the size effect on the LSPR mode, the detectable shift can be explained by using the simple picture of a dipolar resonance. Polar molecules interacting with the dipolar surface charges counter the charge of the formed dipole and stabilize it. This dipole stabilization leads to smaller restoring forces resulting in longer excitation wavelengths.

To take these overall effects into account is of great importance if gold nanoparticles are implemented in plasmonic hybrid devices due to their changed plasmonics upon functionalization with ssDNA, ligands, or upon dimerization.

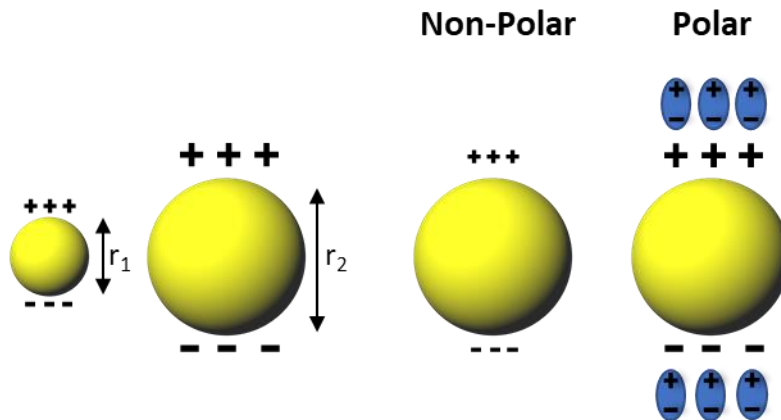


Figure 4: Effect of the size and the surrounding medium, either being polar or non-polar, on the dipolar charge distribution affecting the overall LSPR energy.

2.1.2. Plasmon Hybridization Model

As described in the previous section, the LSPR of a particle can be influenced by several factors like the size and the geometry of gold nanoparticles as well as the polarity and the refractive index of the surrounding medium. Despite this, the LSPR can also be strongly influenced by other nanoparticles in close proximity. The reason is the coupling of resonance modes which manifest themselves in new

modes. This dimerization of nanoparticle lead to so called “hot spots” in the dimer gap and its strength is proportional to the decreasing gap size. [32] Molecules placed in those hot spots reveal a strong coupling to the electric field resulting in high scattering signals of the vibrational molecular fingerprint. [21] Of course, the enhanced scattering signal intensity of molecules on the surface of noble metal surfaces and nanoparticles is not only limited to dimerized nanoparticles but also present on monomers with different sizes and geometries (e.g., core-shell nanoparticles, nanostars, nanorods, nanocubes, etc.) and made of different materials (e.g., gold, silver, copper, etc.). [33-38] This enhancement effect is used in surface-enhanced Raman scattering (SERS) for the vibrational spectroscopic detection of chemical reactions, receptor-ligand interactions as well as a technique for biomedical imaging to give only few examples. [39, 40] Using dimerized gold or silver nanoparticles enables the detection of even single molecules, making SERS to an ultra-highly sensitive spectroscopic method for several applications. [41-43]

The nanoparticle dimerization and coupling of plasmon modes can be described by using the plasmon hybridization model as shown in **Figure 5**. [44, 45] The two nanoparticles with their induced dipole moments (Ψ_1 , Ψ_2) can plasmonically couple to optically detectable, so called bright modes, if they are in parallel, pointing in the same direction (σ and π^*). The other modes with no net dipole moment are called dark modes (π and σ^*).

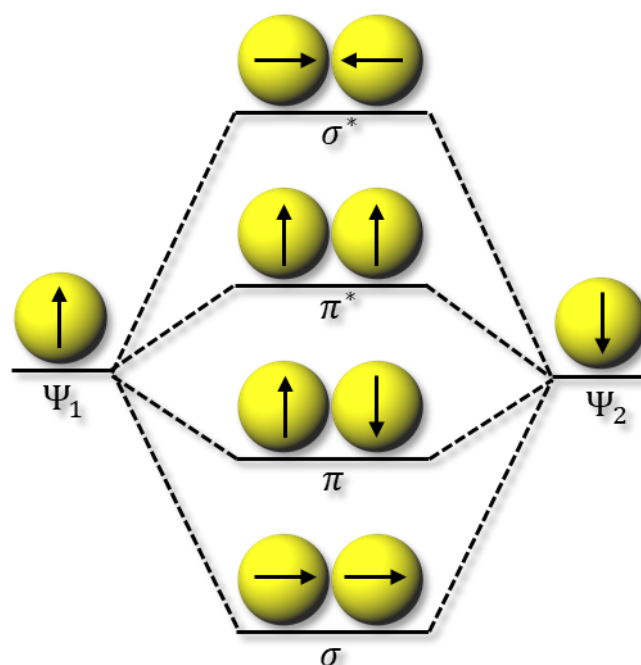


Figure 5: Plasmon hybridization model for a dimer of spherical gold nanoparticles in the quasi-static approximation. The possible dipole moments are represented by arrows. Coupling of plasmon modes results in new modes including bright modes σ and π^* as well as dark modes π and σ^* . Bright modes can be excited by the applied electric field and lead to new visible plasmon modes upon dimerization of gold nanoparticles.

2.2. DNA and DNA Nanotechnology

DNA or Deoxyribonucleic Acid is the carrier of genetic information. This knowledge is not long-dated but was acquired by Oswald Avery, Alfred Hershey and Martha Chase only in 1944 and 1952, respectively. [46, 47] In fact, DNA was first described by the Swiss biochemist Johannes Friedrich Miescher in 1869, who extracted, under slightly acidic conditions, a substance from leucocytes he called *nuclein*. [48] He investigated the overall properties of this mysterious substance which was not degradable by proteases, was rich on phosphorus, not soluble at acidic but soluble at alkaline conditions. [48] However, the chemical building blocks of DNA, called *nucleobases* were first chemically described by Albrecht Kossel, Hermann Steudel and Emil Fischer in the late 19th century. [49-51] In 1910, Albrecht Kossel was awarded with the Nobel price of physiology and medicine for the structural investigation of the four nucleobases. This groundbreaking work was the fundament for the structural elucidation of the DNA double helix by James Watson and Francis Crick (Cavendish Laboratory, Cambridge University) in 1953 with experimental data from Rosalind Franklin (King's College London) gained with X-Ray scattering. [52]

Nowadays, the physical and chemical properties of the DNA are well-known. The DNA consists of nucleotides which are built up by a phosphate, a sugar deoxyribose as well as a nucleobase, as shown in **Figure 6**. DNA is mostly occurring in the right-handed B-Form. The phosphate backbone of the DNA is strongly negatively charged and the chemical linkage between phosphate groups and deoxyribose molecules gives rise to the directionality of each DNA strands, which – by convention – is indicated from the 5'- to the 3' position of the sugar moiety. Indeed, each deoxyribose consists of five carbon atoms which are numbered from 1' to 5'. The nucleobase is bound at the 1'-carbon atom, the 3' has a OH-group and the 5' is connected with a phosphate by a phosphodiester bonding. The OH-group at the 3'-carbon is responsible for the conjugation to the phosphate of the next nucleotide. The information carried by the DNA is encoded by the nucleobases Adenine (A), Thymine (T), Cytosine (C) and Guanine (G). These four different bases, categorized in purines (A, G) and pyrimidines (T, C), can interact with each other in different ways; however, in its common B-form double helix, the DNA molecule relies on the establishment of hydrogen bonds between the nucleobases, A-T and C-G. This, together with the strong base stacking between parallel aligned nucleobases (π - π interactions), explains the mechanical stiffness of the DNA double helix (persistence length, ~50 nm). [53, 54] These interactions include electrostatic as well as van der Waals interactions and are responsible for the helical twist of 34.3° per base. [53, 55]

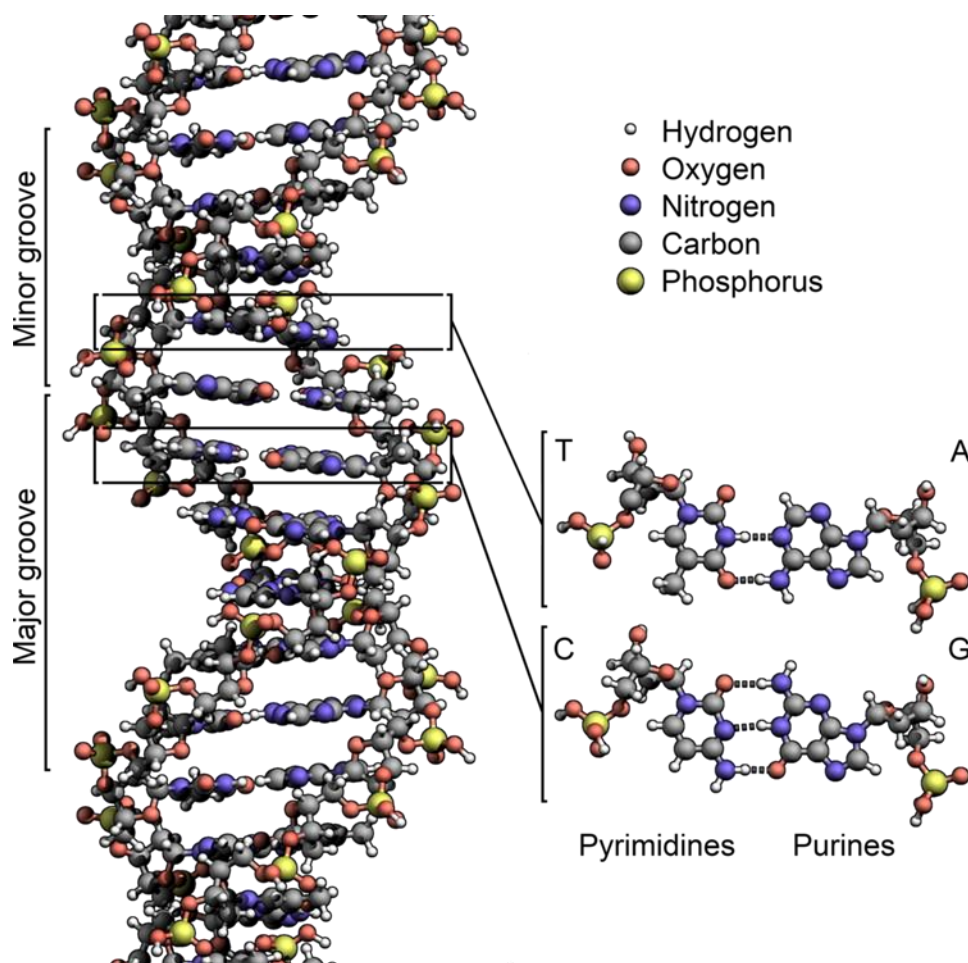


Figure 6: Structure of the DNA double helix according to the Watson-Crick base-pairing. The DNA structure reveals the non-covalent bonding by hydrogen bonds of complementary bases on the same level. Specifically, Adenine and Thymine as well as Cytosine and Guanine form hydrogen bonds. The phosphate-deoxyribose backbone forms the outer layer. Further, the minor (1.2 nm) and major (2.2 nm) groove of the helical structure is shown. The overall diameter of a dsDNA strand is ~ 2 nm and one helical turn is performed every 10.5 bases. (Graphical illustration by Richard Wheeler, Wheeler Lab, London, Creative Common Licence BY-SA 3.0)

DNA nanotechnology was first developed by Nadrian Seeman in 1982. In his pioneering work, Seeman proposed a theoretical approach for building DNA objects from DNA and one year later he demonstrated the feasibility of his idea by designing short double-stranded oligonucleotides that self-assemble into the immobile nucleic acid junction shown in **Figure 7**. [56, 57] The motif is composed of four oligonucleotides and resembles the structure published by Robin Holliday in 1964. [58] The original idea of Seeman was to use such DNA motifs to create artificial crystals and upon incorporation of a protein at each DNA junction, a periodic lattice of proteins would be obtained, as shown in **Figure 7**, B. This should help gathering structural information about the proteins using X-ray crystallography. During the last four decades, DNA design evolved to a high level of sophistication,

enabling to build complex 3D structures which are difficult to obtain by using short oligonucleotides. Particularly, the use of a scaffold-based approach (also called origami) demonstrated to be particularly efficient and became the method of choice for the construction of finite-sized DNA nanostructures. This method will be described in the following section.

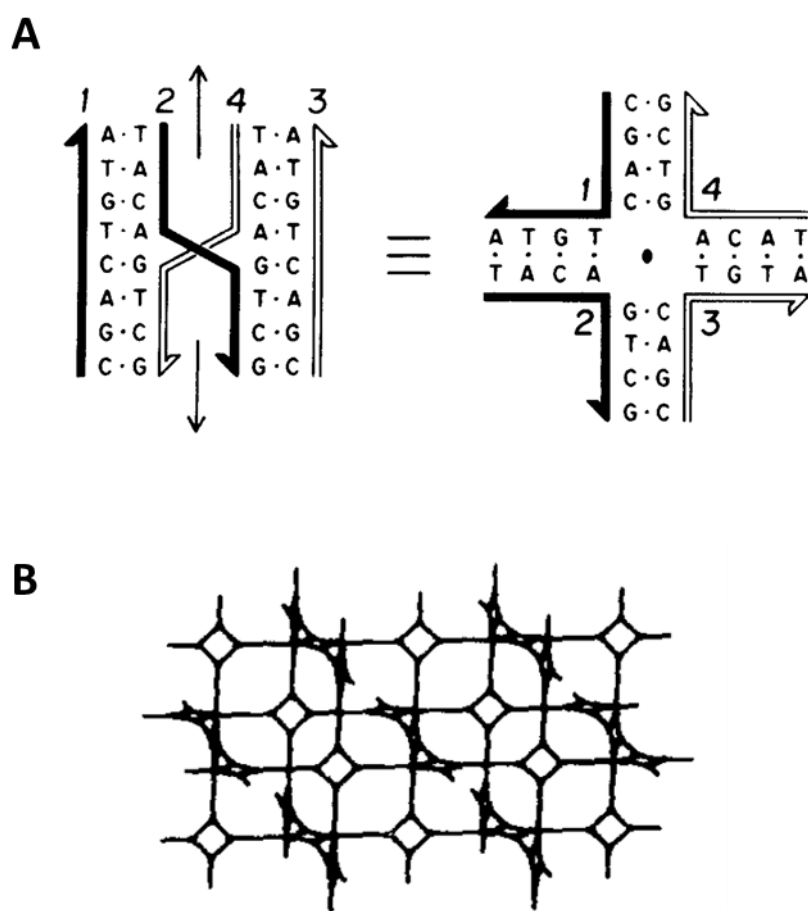


Figure 7: First approach of short oligonucleotides for creation of artificial DNA nanobiotechnological structures. (A) Recombinant junction with the formed Holiday structure (left). Identical structure with the four-fold backbone symmetry. (B) Hierarchical assembly of multiple structures (A, right) to complex 3D networks using sticky ends of the oligonucleotides. Reprinted from [56], with kind permission from Springer Nature.

2.2.1. DNA Origami

Origami, or “折り紙” (oru = folding, kami = paper) in Japanese characters, is the art of folding a 2D piece of paper in a complex 3D shape and was invented nearly a millennium ago in Japan. Similar to this concept, the art of folding is used in the field of DNA nanotechnology to give a 1D single-stranded DNA (ssDNA) molecule a specific, complex and desired 2D or 3D shape for further nanotechnological

utilization. The resulting structure is called DNA origami. This technique was published and described by Paul Rothemund at the Caltech Laboratory in California in 2006. [17] In his ground-breaking work, he used a long ssDNA bacteriophage genome from the phage M13mp18 and hundreds of short oligomeric ssDNA molecules to connect distinct segments of the circular genome as shown in **Figure 8**. [59] The phage genome itself is called *scaffold*, whereas the short connecting oligomers are called *staple strands*. The connection of the distinct scaffold locations is achieved by Watson-Crick base-pairing and the formation of Holliday junctions, also called “cross-overs”, between antiparallel adjacent helices. By routing the scaffold in a predictable way, complex structures can be generated. Especially, the development and further improvement of the solid-phase synthesis of DNA enabled the fast and cost-efficient synthesis of short oligonucleotides, facilitating the spreading of the DNA origami technique. [60, 61]

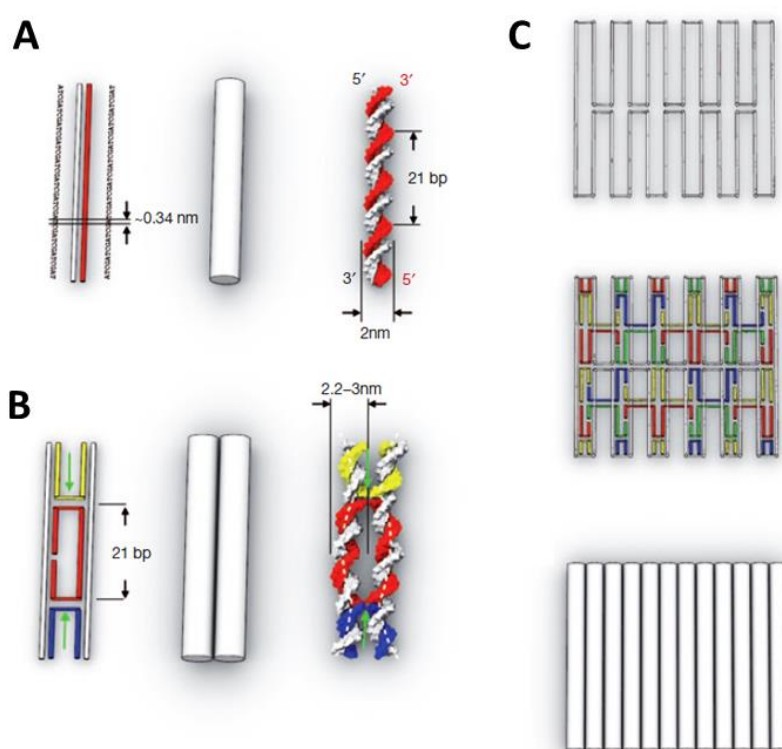


Figure 8: Scaffold-based DNA origami concept. (A) Base pairing of scaffold (white) and staple strand results in double stranded DNA with antiparallel orientation. Dimensions of one single base (0.34 nm) as well as helix diameter (2 nm) and sequence length for one helical turn (21 bp) are depicted. DNA double helices are schematically drawn either as colored lines, greyish cylinders or rendered as B-form double-stranded DNA. (B) Two neighboring double-stranded helices can be connected by holiday junctions (cross-overs) induced by U-turns of the used staple strands. (C) Scaffold routing of 2D DNA origami platform consisting of one single double-stranded DNA layer. Reprinted from [59], with kind permission by Springer Nature.

The rigidity and assembly yield of the resulting 2D or 3D DNA origami structure can be enhanced by various means and a set of “design rules” have been published on this topic. [17, 59, 62-65] First of all, DNA origami structures can be designed according to a “honeycomb” or “square” lattice arrangement of the helices, as shown in **Figure 9** (A, B). Correspondingly, the distance between consecutive cross-overs varies in the two arrangements such to enable adjacent helices to be connected one to the other with an angle of 120° or 90° (**Figure 9**, C). [59] Considering that the B-form of double-stranded DNA has an helical pitch of about 10.5 bp per 360° turn, one dsDNA helix will be connected to three neighboring helices in a honeycomb lattice arrangement by placing one crossover every 7 bp (240°). In contrast, the square lattice with the intrinsic fourfold symmetry allows cross-overs every 5.25 bp (ca. 90°). The geometry of the square lattice leads to inner tension forces and twisting which needs to be corrected by omitting one single base every 50 bp. In the original paper from Paul Rothemund, staples have a length of 32 bases and consist of three binding domains respectively 8-16-8 bp long. In this way, three antiparallel helices can be connected one another within a single DNA origami layer. [17] In literature, it is recommended to use staple strands with an average length between 18-49 bases and keep the melting temperature of the used staples within the same range to favor correct formation of the target structure. [63] Additionally, the presence of unpaired scaffold loops or T5 to T10 staple elongations at the edges of the origami structure prevent multimerization by blunt-end stacking. Finally, the annealing temperature and duration of the thermal ramp as well as the cation concentration (Mg^{2+}) used during assembly has to be carefully evaluated and optimized for each DNA origami shape, as aggregation or kinetic trapping of misfolded intermediate states can dramatically decrease the assembly yield. [65]

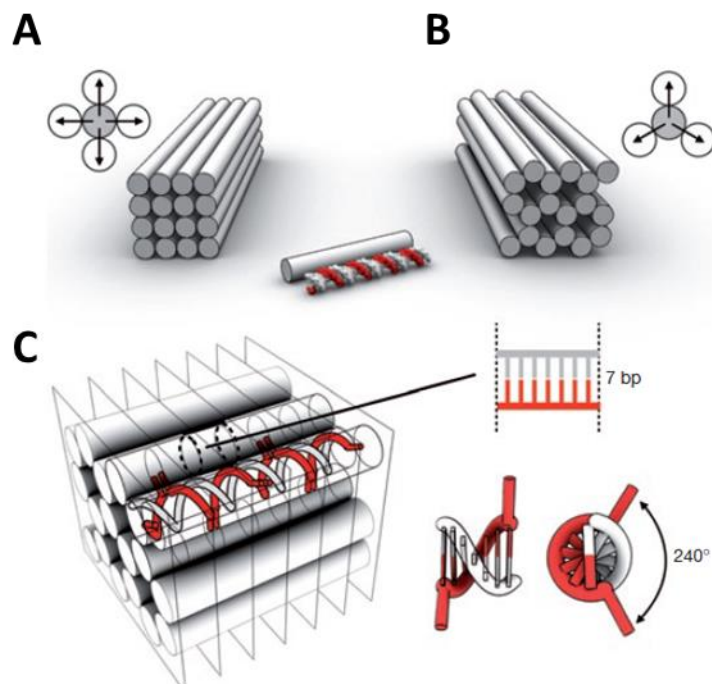


Figure 9: Possible DNA origami packing motives and cross-over rules. Scheme of DNA origami designed in square lattice (A) and honeycomb lattice (B). (C) Cross-over distance of 7 bp for interhelical connection in honeycomb lattice based on the given helical rotation of 240° . Reprinted from [59], with kind permission by Springer Nature.

As it is a challenging task to design a DNA origami based on the rules described before, multiple softwares for computer-aided design (CAD) were developed during the last decades. [66] The first CAD software tool named SEQUIN was developed by Ned Seeman to design the immobile Holliday junction and later versions have been developed to assist the user in the design and visual representation of small DNA motifs. [67] A user-friendly and open-source software named caDNAno for designing 2D and 3D DNA origami was published in 2009 by Shawn Douglas and William Shih. [68] The intuitive interface of this software and its free-accessibility enabled the rapid implementation of the DNA origami technique in many laboratories around the world, making it possible to design a moderately complex structure in a few hours. By importing the scaffold sequence, the staple sequences can be exported for ordering or solid-phase synthesis. A plug-in application is then used for rendering the 2D chart into a 3D model, employing the AutoCAD Maya 2015 software. The structural integrity of a designed DNA origami can be modeled with the online tool CanDo. [59, 68, 69] By using the CaDNAno base pair-map, a mechanical and structural model of the origami is predicted based on the bend, twist and stretch stiffness of ssDNA and dsDNA as well as implemented cross over and backbone nicks. [69]

2.3. Plasmonic Hybrid Materials

The following chapter gives an overview of the field of plasmonic hybrid materials with selected publications. This summary will give an idea of the multiple applications of these hybrid materials and in which directions the ongoing research is developing.

The special feature of DNA origami structures is the possibility to locate molecular objects in space with a precision of few nanometers. When combined with the special optical properties of plasmonic nanoparticles, advanced hybrid nanomaterials can be generated, as testified by numerous studies in the past decade. The arrangement of plasmonic nanoparticles with a sub-nanometer resolution is still challenging and led to new insights in various fields, e.g., plasmon hybridization, plasmonic chirality, surface-enhanced fluorescence spectroscopy or surface-enhanced Raman scattering (SERS) to name only few of them. Likewise, the potential applications of such materials range from detection of analytes using circular dichroism spectroscopy, to single molecule analysis using SERS or enhanced fluorescence imaging. The underlying effect of all these approaches and applications is the photoinduced creation of a highly localized electric field which can interact with molecules placed within the field. The degree of interaction is related to the strength of the electric field which in turn depends on the particle material, geometry, size and coupling state of the electrical field. Consequently, numerous combinations and designs are possible.

One of the first DNA-origami based hybrid nanostructure was published by Liedl and co-workers in 2012. [70] In this work, the authors describe the construction of a DNA origami pillar decorated with nine gold nanoparticles arranged in a right- or left-handed helical fashion along the entire structure, thus leading to an object with an optical circular dichroism signature. A few years later in 2014, Keyser and co-workers published a hybrid nanostructure for SERS detection, consisting of two 40 nm AuNP dimerized via a DNA origami slit, as shown in **Figure 10**, A. The AuNP were functionalized with ssDNA and attached to the DNA origami via staple hybridization. The small gap distance (~ 3.3 nm) between the two NPs resulted into their plasmonic coupling as evidenced by a new plasmonic coupling mode. The small gap distance of the AuNP dimer results in a local field enhancement ("hot spot"). This allowed to detect the Raman reporter Rhodamin 6G present on the AuNP surface at the single-particle level. Similar results were published in the same year by Feldmann and co-workers. [71] By using a different sheet-like origami design with SYBR Gold molecules intercalated in the minor groove of the double helix, they dimerized 40 nm AuNP. The controlled dimerization resulted in 6 nm gap distances and the formation of a hot spot. By estimation of the molecules inside the hot spot, they predicted SERS enhancement factors (SERS EF) of 3.1×10^5 and compared them with FDTD calculated EF values (max. 2×10^6). Similar to Liedl and co-workers, they showed the potential of these kinds of hybrid materials for enhanced spectroscopy. However, these first hybrid materials reveal a lack of control

over the number of reporter molecules placed inside the hot spot and the overall presence of DNA in the gap.

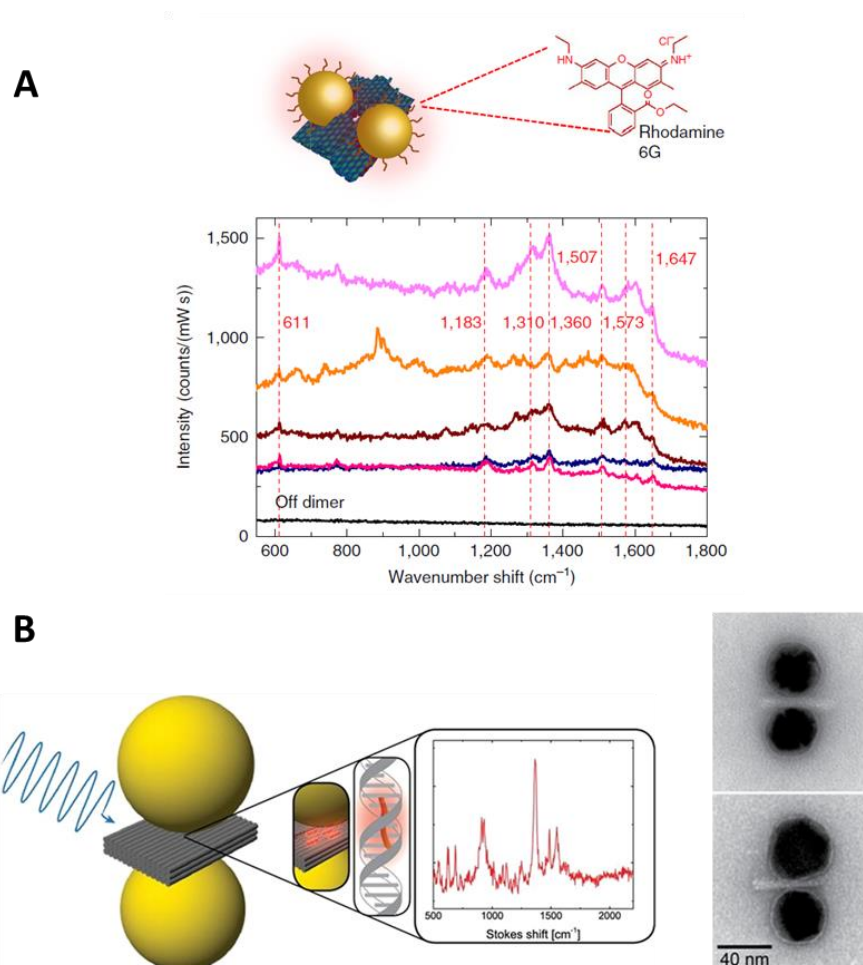


Figure 10: Early published hybrid nanostructures for SERS. Dimerization of 40 nm AuNP by using DNA origami and staple hybridization enable controlled interparticle gaps of ~ 3.3 nm (A) [72] as well as ~ 6 nm (B) [71] resulting in plasmonic coupling and SERS detection of Rhodamin 6G and SYBR Gold intercalated in the double helix. Reprinted with kind permission.

The local enhanced electric field of a hot spot was also used for improving the optical response of a fluorophore in metal-enhanced fluorescence (M-FRET). By increasing the radiative decay rate and decreasing the lifetime of a fluorophore, the quantum yield and thus the overall fluorescence of fluorophores can be increased. [73, 74] These effects were used in multiple publications. In 2015, Xu and co-workers dimerized two gold nanorods (AuNR) on a DNA origami breadboard resulting in a hot spot formed by the AuNR tips as shown in **Figure 11**, A. [75] By using different gap distances ranging from 6.1 nm to 26 nm, the authors were able to enhance the fluorescence of ATTO-655 molecules diffusing into the gap. From the low fluorophore concentration (~ 50 nM) and the small hot spot volume, the authors concluded that single-molecule fluorescence detection is visible as burst-like

signals upon diffusion into the gap. Using this method, up to 470-fold fluorescence enhancement was observed. However, no control over the relative orientation and number of fluorophores inside the gap can be achieved using this design.

As mentioned above, the geometry and arrangement of gold nanoparticles have a big impact on the plasmonic coupling and the formation of the local enhanced field. In 2017, Bald and co-workers showed the potential of gold nanolenses for manipulating the electrical field (**Figure 11**, B). The collinear arrangement of self-similar gold nanoparticles in a chain-like manner can lead to a cascade enhancement of the electric field and the formation of a strong hot spot. By using labeled oligonucleotides, the Raman reporter dye (TAMRA) was placed on different nanoparticles of the nanolens and the SERS signal strengths of the various constructs were compared. Theoretically calculated EF values for nanolenses published before showed gigantic enhancement factors around 10^{13} , however, in this first approach by Bald and co-workers, EF values of $\sim 10^6$ were reached experimentally.

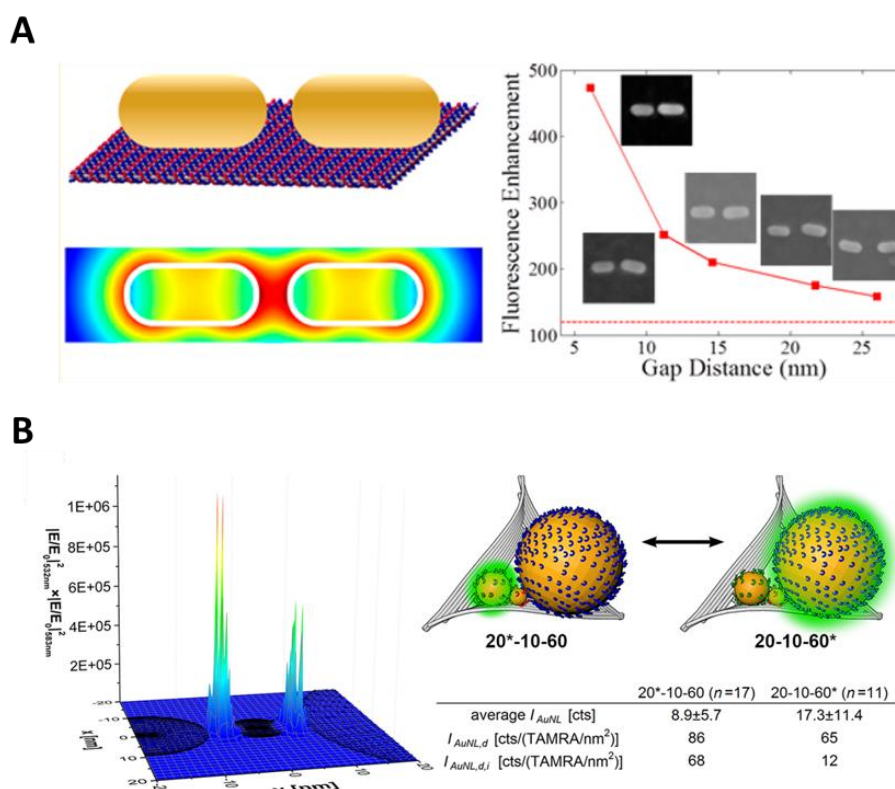


Figure 11: Advanced hybrid nanostructures for metal-enhanced FRET (M-FRET) and SERS nanolenses. (A) Two AuNR are dimerized on a DNA origami breadboard with different gap distances ranging from 6.1 nm to 26 nm for enhanced fluorescence of ATTO-655 placed inside the formed hot spot. [75] (B) Complex arrangement of differently sized AuNP on a DNA origami triangle for the formation of a gold nanolens. Due to the geometrical arrangement, a cascaded field enhancement leads to high SERS EF values and high signal strength of reporter molecules inside the hot spots. [76] Reprinted with kind permission.

More recently, advanced hybrid materials were published which bear the potential for a biomedical application and also exhibit higher control over the number and position of reporter molecules and proteins inside the hot spot as shown in **Figure 12**. In 2018, Liedl and co-workers designed and tested a AuNR-based hybrid nanostructure for detection of picomolar viral RNA concentrations in human serum as shown in **Figure 12, A**. [77] The nanodevice is based on the structural reconfiguration of two dimerized AuNR resulting in a strong circular dichroism signal. Although the used RNA concentrations are 10 times higher than those commonly present in the serum of infected people, the work demonstrates the successful realistic application of a plasmonic hybrid nanostructure.

The detection of a single molecule using SERS was described more than 20 years ago separately by Nie and Emory as well as Kneipp and co-workers in 1997. [78, 79] As written by Bald and co-workers in a recently published paper in 2021, the ultimate detection limit in physical chemistry is the detection of a single molecule. [41] By the dimerization of two 60 nm gold spheres with a DNA origami fork, they were able to achieve this ambitious aim using a hybrid nanomaterial. Gap distances of around ~ 1.17 nm enabled SERS enhancement factors of $\geq 10^9$ under non-resonant conditions, which is assumed to be the lower limit for single-molecule detection. By placing different Raman reporters with resonant and non-resonant excitation inside the hot spot, the authors were able to demonstrate in both cases the SERS detection of single molecules. Besides this reporter-based approach, the authors also demonstrated the detection of single proteins placed in the hot region. Of course, the large size of the proteins used (namely, cytochrome C and horseradish peroxidase (HRP)) precludes their full accommodation within the hot spot (in that case 27 nm^3 for ~ 3 nm gap distance). However, characteristic vibrational bands of the proteins, e.g., a porphyrin stretching band at 1370 cm^{-1} as well as the heme group of the HRP at 1580 cm^{-1} , could be detected. On the other hand, placing a large protein partially inside the gap and gaining valuable information about the structure or function of the protein from this set-up is still an open challenge that should be addressed in the future.

To conclude, it can be said, that hybrid nanomaterials are promising candidates for the enhancement of optical readouts due to the plasmonic character of noble metal nanoparticles. The controlled dimerization of nanoparticles by DNA origami can enable the detection of even single molecules for diagnostic applications. However, the small gap sizes and currently used techniques, like the staple strand hybridization for dimerization of plasmonic nanoparticles, lead to hot spots that are not fully accessible. This is one of the major tasks addressed in this thesis.

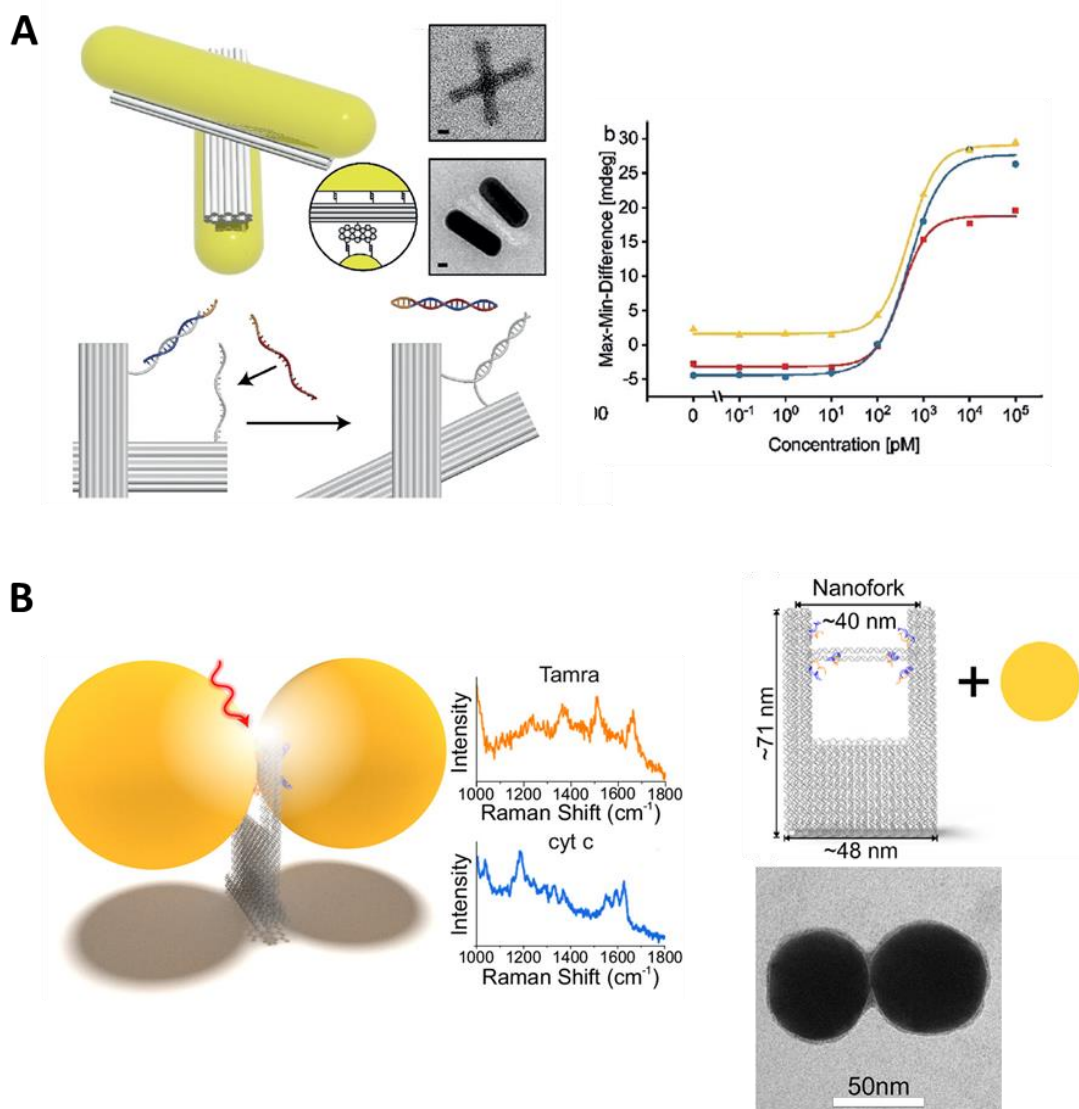


Figure 12: Recently published hybrid materials for biomedical applications and single-molecule SERS detection. (A) Dimerized gold nanorods enable the picomolar detection of specific RNA sequences in biological samples by using a reconfigurable DNA origami design (scalebar = 20 nm). Upon RNA binding the conformational change of the structure leads to strong circular dichroism. [77] (B) DNA origami nanofork used for AuNP dimerization and detection of single molecules and proteins placed inside the hot spot. [41] Reprinted with kind permission (A) and under Creative common license BY-NC-ND 4.0 (B).

3. Material and Methods

3.1. Materials

All equipment, materials as well as chemicals used in this thesis are listed in the appendix (See II. Lists of Equipment, Materials and Chemicals).

3.2. Synthesis of Gold Nanoparticles

If not stated differently, the concentration of the colloidal AuNP and AuNC was determined by using UV-Vis extinction spectroscopy as described by Hendel *et al.* 2014. [80] The size and volume of the AuNP and AuNC derived from statistical analysis of TEM images of the colloids were used to calculate the mean value of the volume and the gold atoms per nanoparticle. In combination with the Au(0) concentration, the molar nanoparticle concentration was determined.

3.2.1. Spherical Gold Nanoparticles (AuNP)

The synthesis of spherical AuNP was carried out by following a modified protocol published by Park *et al.* 2018. [81] A scheme of the synthesis concept is shown in **Figure 13**. Briefly, 8 nm CTAC-capped AuNP were synthesized in aqueous solution at 30 °C by first preparing 1-2 nm CTAB-capped gold nanoclusters. 9.75 mL CTAB (100 mM) was mixed with 250 µL of 10 mM HAuCl₄ inside a 25 mL sample glass vial with snap-caps (VWR). After 30 s of sonication the resulting yellowish solution was stirred at 1,200 rpm followed by the one-shot addition of 600 µL of freshly prepared ice-cold 10 mM NaBH₄ solution. The brownish solution was stirred at 400 rpm for 3 min after addition and incubated at 30 °C for 1 h prior to use. Next, 8 nm AuNP were synthesized by sequentially mixing 20 mL CTAC (200 mM) with 15 mL AA (100 mM) and 500 µL of the gold clusters under mild stirring at 300 rpm. The growth process starts when 20 mL HAuCl₄ are added in one shot. After 15 min of constant mixing, the resulting reddish colloid was centrifuged twice (64,000 rcf, 46 min) and redispersed in DI water for further functionalization or 20 mM CTAC for growth of AuNC. The synthesis of AuNP with a larger diameter (12 nm, 15 nm) was achieved by changing the concentration of the used HAuCl₄ solution (0.75 mM, 2.9 mM) during the growth process.

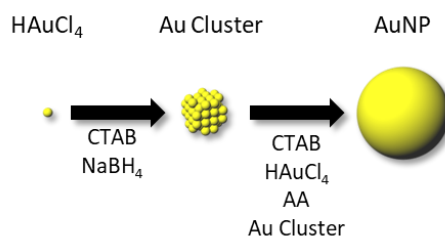


Figure 13: Schematic representation of AuNP synthesis resulting in AuNP with a diameter between 8 and 15 nm.

3.2.2. Gold Nanocubes (AuNC)

The synthesis of ultra-small AuNC was carried out using a seedless CTAB-based protocol. A scheme of the synthesis concept is shown in **Figure 14**. Briefly, in a 100 mL round-bottom flask, 40 mL of DI water, 16 mL CTAB (100 mM), 150 μ L NaBr (120 mM) and 500 μ L HAuCl₄ (10 mM) were mixed sequentially under mild stirring at 500 rpm and 30 °C. Next, 4.75 mL of AA (100 mM) was added. When the yellowish solution turned transparent, 50 μ L of freshly prepared and ice-cold NaBH₄ (10 mM) was one-shot added under vigorous stirring at 1,000 rpm. The resulting solution was stirred for 5 min and incubated o.n. at 30 °C prior to purification by DGC.

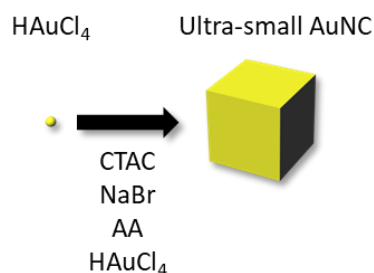


Figure 14: Schematic representation of the synthesis of ultra-small AuNC resulting in AuNC with 10 nm edge length after purification by DGC.

The DGZ for isolation of 10 nm AuNC was performed in 20 mM CTAC with a glycerin gradient (20%, 15%, 10%, 5%). After the layer-by-layer stratification of the gradient in a 15 mL centrifugation tube (Falcon, Fisher-Scientific) a concentrated sample of the ultra-small AuNC colloid was carefully pipetted on the top of the gradient and the sample was centrifuged at 4,864 g (4.25 h). The middle fraction of the resulting colloidal gradient was carefully taken, diluted 1:1 with CTAC (20 mM), centrifuged twice at 21,000 g (25 min) and resuspended in DI water for further functionalization.

The synthesis of small AuNC was carried out following a modified protocol published by Park *et al.* 2018. [81] A scheme of the synthesis concept is shown in **Figure 15**. Briefly, 18 nm AuNC were synthesized by mixing sequentially 6 mL CTAC (100 mM) with 30 μ L NaBr (5 mM), 600 μ L CTAC

stabilized AuNP (8 nm diameter, 22.7 nM, synthesis see 3.2.1) and 390 μL AA (10 mM) under stirring at 500 rpm in a sample glass vial with snap-cap. Next, 6 mL of HAuCl_4 (0.5 mM) was added in one shot and the resulting colloid was stirred for 25 min. Finally, twice centrifugation at 20,600 g for 30 min and redispersion in Di water for further functionalization was performed. For the synthesis of 16 nm AuNC 800 μL AuNP and 30 μL NaBr (2.5 mM) were used, respectively.

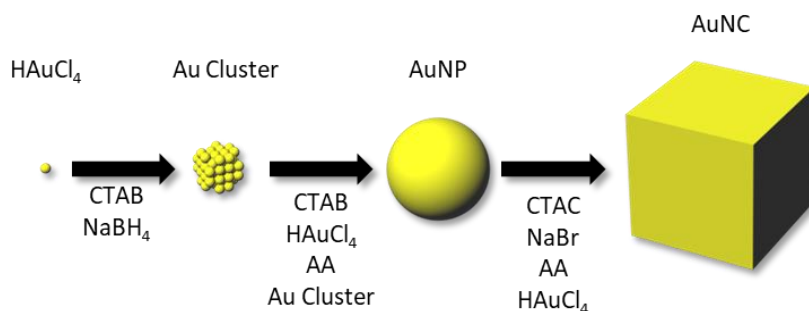


Figure 15: Schematic representation of AuNC synthesis reported by Park *et al.* 2018 resulting in AuNC with an edge length ≥ 16 nm.

3.3. Functionalization of Gold Nanoparticles

3.3.1. Ligand Exchange

The synthesized gold nanoparticles must be stabilized with different surface-active molecules for evaluation of the colloidal stability under DNA origami buffer conditions, which show a high ionic strength. Centrifugation and resuspension steps are described as ‘washing steps’ in the following protocols. Stability of gold nanoparticles were verified by UV-Vis spectroscopic analysis of the plasmon peak. Ligand exchange procedures of the micelle-forming and surface-active cationic CTAC and CTAB bilayer on the nanoparticles were carried out as follows:

Exchange by SDS was performed by centrifugation and resuspension of the synthesized nanoparticles in 0.5 wt % SDS. After incubation o.n., the colloid was centrifuged and resuspended by sonication (30 s) four times in 0.5 wt % SDS. Finally, the colloidal OD was adjusted to 1 by dilution with 0.5 wt % SDS.

Exchange by citrate was performed following a modified protocol described by Mehtala *et al.* 2014. [82] A typical process with a colloid ($\text{OD} = \sim 2.5$) consists of five centrifugation and resuspension steps (21,000 g, 25 min). Excess CTAB or CTAC in the supernatant is removed prior to the ligand exchange after the synthesis by two washing steps as described before (3.2) resulting in a final concentration of < 1 mM. The colloid was then washed three times with 0.15 wt % PSS followed by

two additional washing steps using 5 mM citrate. Finally, the colloidal OD was adjusted to 1 by dilution with 5 mM citrate.

Exchange by BSPP was performed following a modified protocol described by Yao *et al.* 2020. [83] Briefly, 5 mL nanoparticle suspension was mixed with 1.5 mg BSPP and incubated under mild shaking (300 rpm) o.n. followed by slow addition of NaCl (solid) until a color change from red to slightly purple can be noticed. Afterwards, the mixture was washed by centrifugation at 7,000 g for 5 min and resuspended in 300 μ L BSPP ($0.15 \text{ mg} \cdot \text{ml}^{-1}$) containing 50 vol. % MeOH to remove residual CTAC/CTAB on the nanoparticle surface. Finally, the last washing step removes excess of BSPP by centrifugation and the colloid is adjusted to OD 1 by resuspension in DI water.

3.3.2. ssDNA

Gold nanoparticles functionalized with thiolated ssDNA were produced as reported by O'Brien *et al.* 2015. [84] The method is based on a surfactant-assisted salt-aging mechanism to maximize the ssDNA density on the gold nanoparticle surface. The excess of thiolated ssDNA used in the following protocol is based on the approximated area of $1.8\text{-}3.1 \text{ nm}^2$ occupied by a dsDNA cylinder on the AuNP surface. [85] Briefly, 177 μ L (1 mM) thiolated and protected ssDNA were deprotected by incubation with 100x molar excess of TCEP in DI water for 30 min followed by purification with NAP-5 and NAP-10 desalting columns. The volume was reduced by cut-off filtration (3 kDa) to $\sim 50 \mu$ L and added to 1 mL gold nanoparticles (100 nM) stabilized with 0.5 wt % SDS followed by incubation at RT for 2 h. Afterwards, the nanoparticle colloid was diluted to 0.01 M PBS (pH = 7.4) and stepwise every 30 min NaCl (5 M) was added until 0.05 M, 0.1 M, 0.15 M, 0.2 M, 0.25 M and 0.3 M NaCl was finally reached. To ensure the maximum loading density of ssDNA on the nanoparticle surface, the colloid was incubated on a shaker at 300 rpm o.n.. Afterwards, the colloid was diluted 1:1 with 0.5 wt % SDS and washed two times with 0.2 wt % SDS and a third time followed by resuspension in 100 μ L 0.01 wt % SDS. The concentration of the gold nanoparticles was determined by UV-Vis spectroscopic analysis.

3.4. Computer-Aided Design of DNA Origami

The DNA origami structures used in this thesis were designed by Richard Kosinski using caDNAno (v2.2.0) and Autodesk Maya (2015). For visualization of the 3D models Autodesk Maya 2018 and 2020 were used. The terminology used in this thesis is based on the images of DNA origami structure as shown in the caDNAno files (3.4.1 and 3.4.2). If not stated otherwise, the staples are named as follows: The first number in bold denotes the helix from which the staple starts, with the number in brackets that stays for the position of the 5'-terminus of that staple within the helix. Similarly, the 3'-end of the

same staple is indicated by two numbers: the first in bold stays for the helix position within the origami and the second number in brackets indicates the position of the 3' terminal base along that helix. Basically, the caDNAno chart is mapped with xy coordinates, with each xy point corresponding to one nucleobase: the y-axis indicates the number of the helix within the origami and the x-axis indicates the position of the nucleobase on that helix. The design of the origami used in this thesis is based on a derivative of the bacteriophage M13mp18 ssDNA called p8064. To avoid local weak points and breaking of the 3D-structure, a twist correction was performed for the planar platform.

3.4.1. Pandora's Box

The incorporation of gold nanoparticles for their programmed placement and site-specific functionalization as a plasmonic building block requires the design of a lidless DNA origami box, that we called Pandora's box. The Pandora's box is a bilayered DNA origami structure consisting of duplexes organized in a square-lattice and is made up of four walls and one core plate as shown in **Figure 16 (A)**. Dimensions are derived by sequence length and number of connected helices and based on values published in literature.[86] Overall, Pandora's box has a calculated height of 25.4 nm, an outer width of 31.7 nm and an inner width of 21.3 nm, respectively. The scaffold strand is arranged in a way that four walls of rectangular shape are formed which consist of eight helices each with a length of 95 bases (**Figure 16 (B)**). Contiguous walls are connected by staples and remaining unpaired scaffold at the edges of each upfolded wall is passivated using staples with poly-T overhang to avoid unspecific dimerization of boxes during assembly and to enlarge the overall assembly yield. The base of the box is made up of four convergent triangular sections obtained by arranging the scaffold in six helices, each getting shorter towards the center. The longest helix, which connects the core plate to the walls, is 87 bp long whereas the helix in the center is 11 bp long. To stabilize the short helices in the center of the core plate, one 56 bases long staple strand is used which contains short poly-T sequences to avoid tensile stress. The binding of gold nanoparticles necessitates the implementation of protruding staples inside Pandora's box for either hybridization of ssDNA-coated gold nanoparticles with complementary strands, or the placement of thiolated oligonucleotides inside the DNA cavity for direct covalent bonding to the gold surface (**Figure 16 (C)**). Achieving high incorporation yields is possible and can be correlated to the number of thiols inside Pandora's box (i.e. 0, 4, 8, 16 or 28 thiols). To minimize the number of distinct thiolated oligos, the protruding strands (red) pointing inside the box have the same nucleobase sequence, called cF9(16). The thiolated oligonucleotides (blue), called F9(16)-SH, are complementary to the protruding arms and thus form duplexes with the terminal thiol groups oriented towards the center of the box.

Detailed caDNAno images (**Figure S 1**) as well as the scaffold and staple sequences can be found in the appendix (III. List of the DNA sequences).

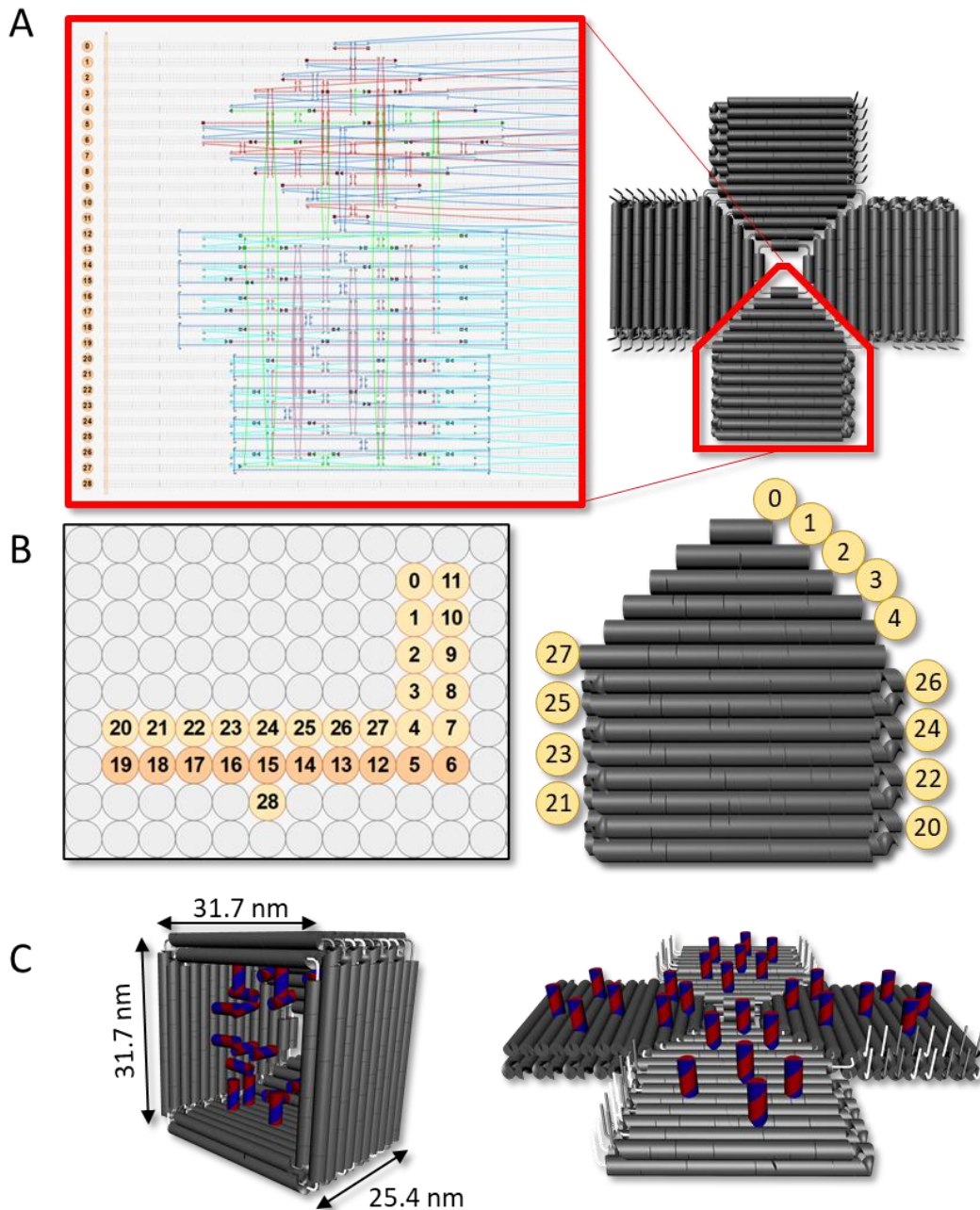


Figure 16: Scheme of Pandora's box design. (A) Scaffold and staple pathways in caDNAno of one of the four building blocks of Pandora's box (folded down) marked in red. (B) Helical structure from a side view in caDNAno with corresponding numbering in one building block. (C) Complete assembly of Pandora's Box with dimensions derived from the number of helices and base length. Multiple thiolated anti-handles were placed inside the cavity by replacing staple strands of the core and walls by complementary protruding handles (red)

3.4.2. Zelos Dynamic Platform

The dynamic arrangement of gold nanoparticles inside Pandora's box requires the design of a platform which is herein referred to as Zelos. Zelos was realized as a bilayer platform consisting of two parts connected by eight helices (four above and four below the inner cavity). These helices enable the dynamic actuation of the device, as shown in **Figure 17** (A). The square lattice bilayer consists of 20 parallel helices (**Figure 17** (B)) each with a length of 214 bp. Overall, the dimensions of the platform are 72.8 nm in length and 58.1 nm in width. Additionally, four staples of each half can be replaced by handles to enable the hybridization with two facing Pandora's boxes, as described later. To prevent unspecific base-stacking between the helices at the opposite sides of the gap, the terminal ends of these helices were modified with poly-T overhangs. The same concept is used at both short edges of the rectangular shape to prevent origami-to-origami stacking.

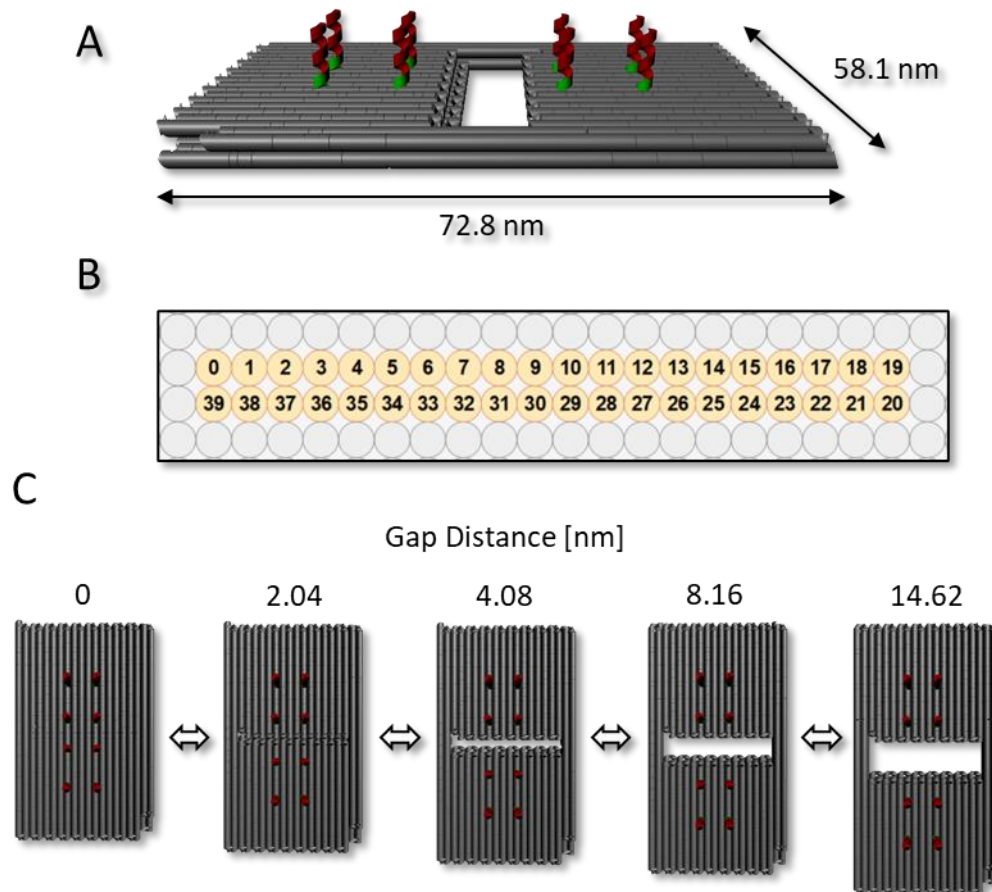


Figure 17: Scheme of the dynamic DNA origami platform called Zelos with four protruding staple strands on each moiety of the platform (A). The dynamic gap formed by eight helices which separate the platform halves and length can be varied by staple strand displacement reaction. (B) Depiction of the helical structure derived from caDNAno. (C) Gap distances used in this thesis and achieved by toehold-mediated staple-displacement.

Detailed caDNAno images (**Figure S 2**) as well as the scaffold and staple sequences can be found in the appendix (III. List of the DNA sequences).

The dynamic properties of Zelos are achieved through toehold-mediated strand-displacement reactions as shown in **Figure 18**. By using staples of different sequence lengths hybridized to portions of the scaffold within the gap, different edge-to-edge distances with base pair-wise stepping can be achieved. In this thesis, staples of 0, 6, 12, 24 and 43 bases were used (also referred to as fuels), enabling to achieve a distance between the two halves of Zelos which is correspondingly equal to 0, 2, 4, 8 and 14.6 nm, as shown in **Figure 17** (C). In the following, the process is described in detail for the change of gap distance from the maximal to the minimal value achievable, i.e. from 14.6 nm to 0 nm. In the initial state (14.6 nm), the eight helices of the central seam connecting the two halves of Zelos are made of a 43 bp-long duplex portion that spans the inner gap and two stretches about 15 bp-long that are inserted within the DNA origami structure to ensure connection of the two halves (**Figure 18** (A)). Additionally, each staple (green strand) that is hybridized to the ss-region of the scaffold (black strand) contains a toehold of eight bases, which is necessary to initiate the strand-displacement reaction. Upon addition of excess of anti-fuel strands that are fully complementary to the fuel staples, the staple-displacement reaction leads to unpaired scaffold in the gap (**Figure 18** (B)). This intermediate state is characterized by an undefined distance between the two halves of Zelos and can be transformed into another state of predefined distance by the addition of another set of fuel strand (**Figure 18** (C)). To avoid mechanical stress in the eight connecting helices induced by the different scaffold orientation at varied distances, one unpaired scaffold base was implemented in the design at the end of each fuel-staple as shown in **Figure 18** (A).

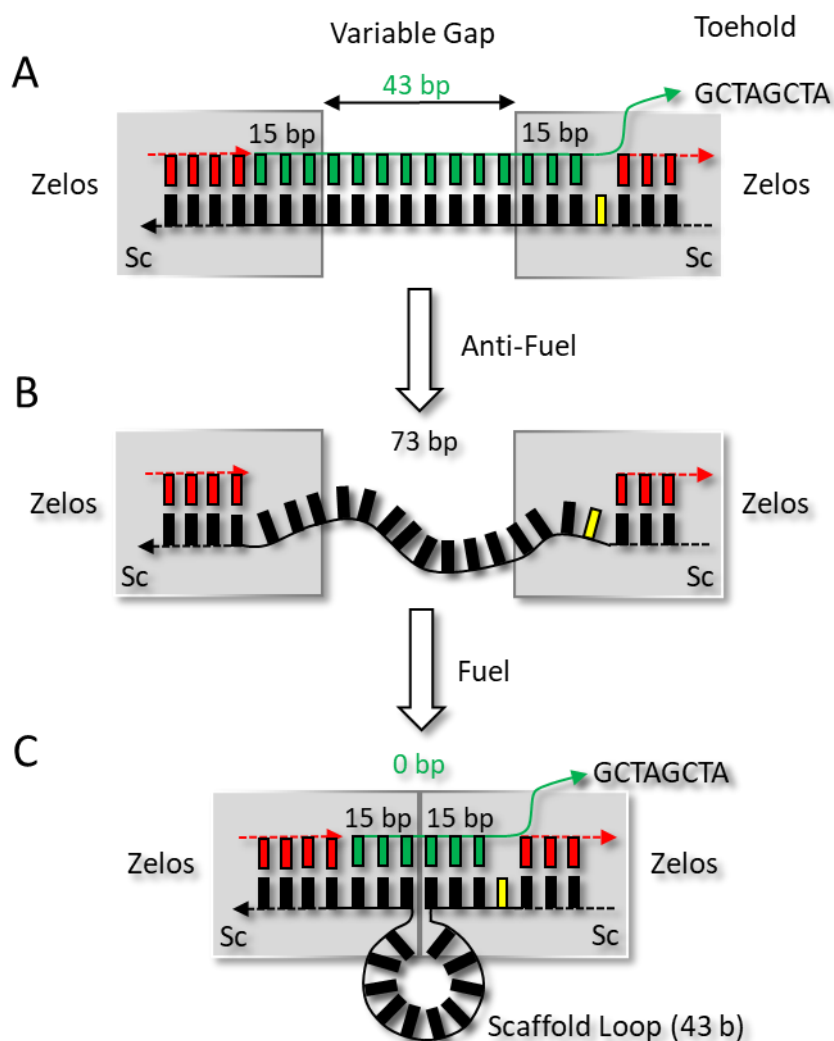


Figure 18: Scheme of the toehold-mediated strand displacement of Zelos DNA origami platform with implemented mechanism for variation of the gap distance. Depicted is one of eight helices for distance control. (A) Maximum gap distance of 14.62 nm is achieved by forming a duplex with the total scaffold of Zelos in the variable gap region. Shown are the scaffold (black) with the unpaired base to avoid mechanical stress (yellow), staple strands (red) and the fuel staple (green) consisting of two 15 bp anchor regions and the distance-determining region in between. (B) toehold-mediated removal of the 43 bp staple by adding anti-fuel staple leads to a single-stranded scaffold in the gap with non-defined distance. (C) The added fuel staple (e.g., 0 bp) hybridizes with the scaffold and form a scaffold loop of ssDNA while pulling both Zelos moieties together.

3.4.3. Hybridization of Pandora's Box onto Zelos

The hybridization of Pandora onto Zelos was carried out using four protruding strands on each half of Zelos. Those strands hybridize inside one specific wall of the DNA origami box as shown in **Figure 19**. For this purpose, complementary oligonucleotides in the Pandora design have been omitted (**4[59]13[51]**, **7[93]13[83]**, **24[59]17[51]**, **24[91]17[83]**). Hybridization of Pandora without AuNP was performed with threefold molar excess of AGE-purified Pandora (20 nM) with respect to AGE-purified

Zelos (10 nM) at 30 °C with an incubation time of one to seven days. If Pandora-gold nanoparticle conjugates were used, lower concentrations (Pandora 0.6 nM, Zelos 0.15 nM) and a fourfold Pandora excess was used and the hybridization time was extended by 7 days. Hybridization took place in 0.5xTEMg with MgCl₂ concentrations varying between 0 mM and 50 mM.

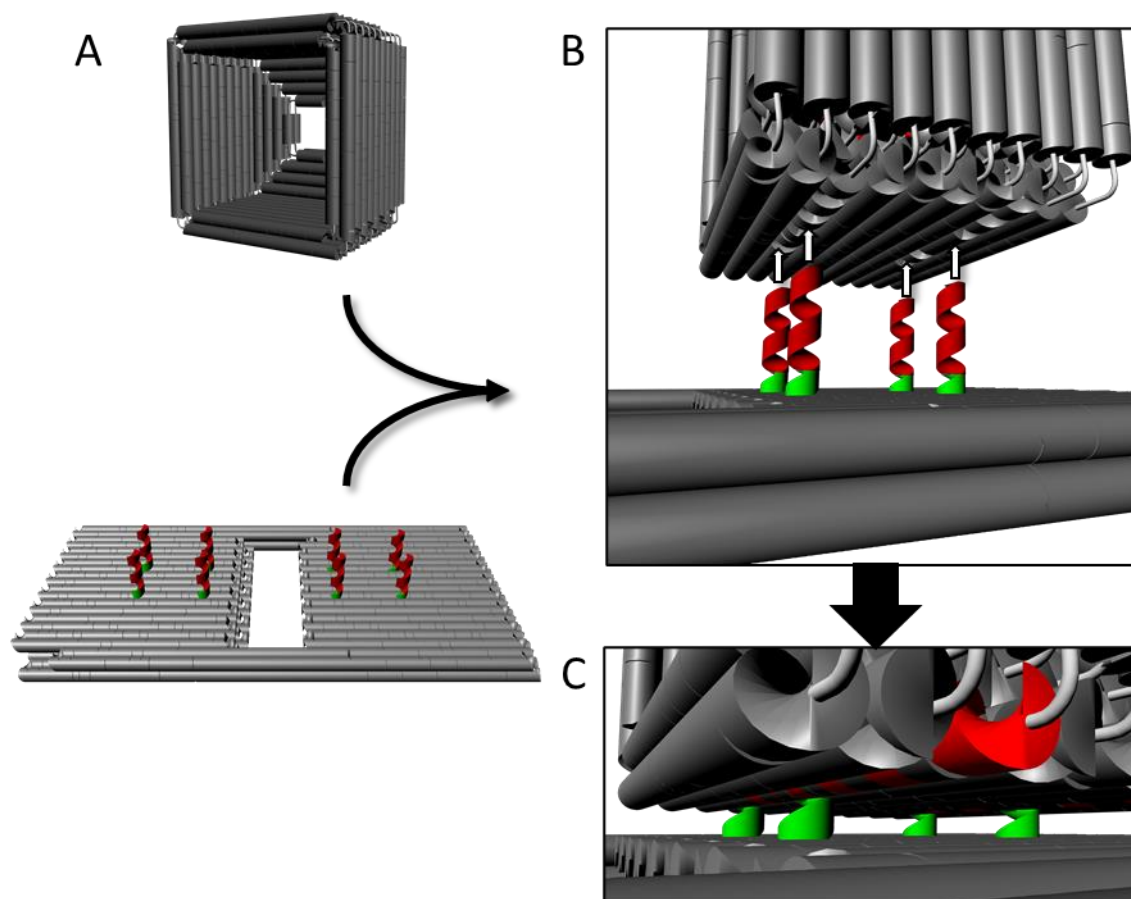


Figure 19: Hybridization concept of Pandora's box onto Zelos. If the box approximates to the four protruding staples (red) located onto each moiety of Zelos, hybridization with the complementary free scaffold sequences (each ~30 bases) of staples omitted during assembly can take place. To increase the hybridization yield by minimizing the electrostatic repulsion of the negatively charged phosphate backbone of the DNA, a 3T-spacer (green) was included

3.5. Assembly of DNA Origami

The one-pot assembly of the DNA origami used in this thesis was carried out using a derivate of the M13mp18 phage genome as scaffold, namely p8064. Briefly, the p8064 scaffold strand (10 nM) was mixed to a tenfold excess of each staple strand (100 nM) in 1xTEMg 12.5 buffer containing 20 mM tris base, 2 mM EDTA, 12.5 mM MgCl₂ at pH 7.6. The thermal annealing protocol is based on the highest melting temperature of duplex DNA domains and was carried out as shown in **Figure 20**. To increase

the assembly yield, a staple-screening with changed staple excess with respect to the scaffold concentration as well as a Mg-screening with Mg concentrations varying from 0 mM MgCl₂ to 22 mM MgCl₂ was performed (section 4.4, 4.7).

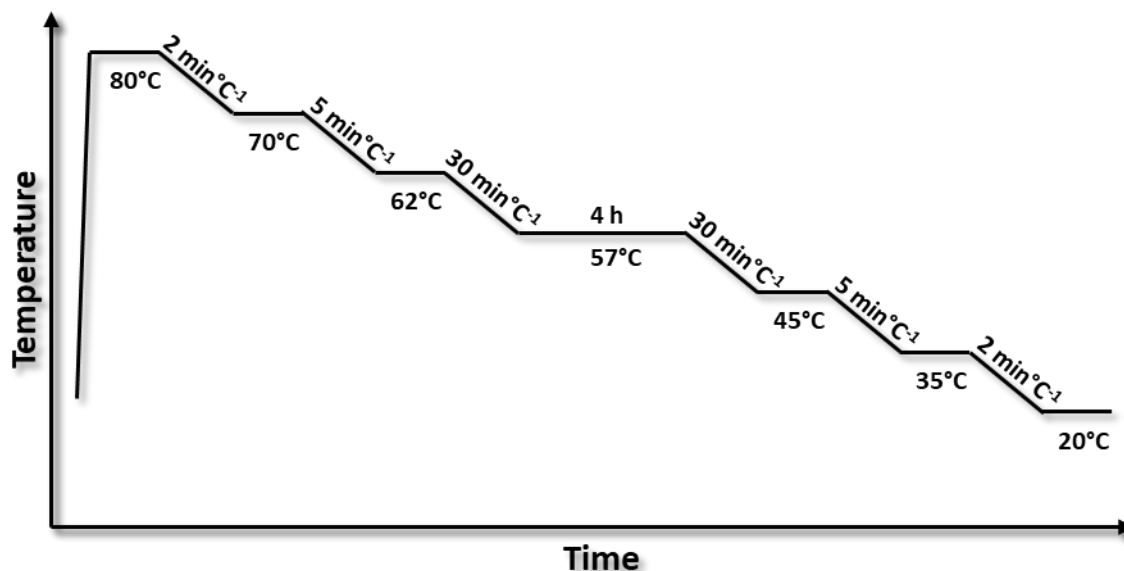


Figure 20: Scheme of the thermal annealing ramp used for assembly of Pandora's box and Zelos.

3.6. Incorporation of Gold Nanoparticles into Pandora's Box

The incorporation of gold nanoparticles into Pandora's box was carried out by utilizing two different mechanisms; first the hybridization-based duplexing of complementary ssDNA strands, one localized on the surface of the gold nanoparticle and one localized as protruding strand inside the box and a second procedure that relies on the thiol chemistry-based covalent conjugation of bare gold nanoparticles to thiols presented in the box cavity. [87]

The **hybridization-based approach** was carried out as follows:

Briefly, 2.5x molar excess of ssDNA conjugated gold nanoparticles synthesized as described in chapter 3.3.2 were mixed with Pandora (10 nM) in 0.5x TE[Mg] [6.25 mM] and incubated o.n. at 300 rpm shaking. Binding yield was analyzed by TEM of 1:1 diluted sample.

The **thiol chemistry-based approach** was carried out as follows:

Briefly, 1 mL Pandora (15 nM) containing between 0 and 28 thiolated oligonucleotides was deprotected in 0.5 mM TCEP for 45 min followed by removal of unreacted TCEP with cut-off purification (100 kDa, Amicon Ultra-15). Cut-off purification was carried out as described by manufacturer until remaining TCEP concentration was ≤ 50 nM calculated by simple dilution factors.

The purified origami were then mixed with 20x molar excess of Tween20 stabilized gold nanoparticles in 0.5x TE[Mg] [6.25 mM] with final concentration of 0.2 wt % Tween20. The mixture was inverted several times and incubated at RT for 24 h prior to further analyzation by TEM. To remove excess gold nanoparticles after successful incorporation AGE purification was used as described in chapter 3.7.3.

3.7. Analysis and Purification Methods

3.7.1. UV-Vis Absorption Spectroscopy

UV-Vis extinction spectroscopy is an optical method for evaluation of the interaction of light with molecules with different sizes ranging from low-molecular (e.g., TAMRA, small peptides) to macromolecular size (e.g., proteins) as well as nanoparticles. The interaction is based on scattering and absorption processes, where the extinction (absorption and scattering) of the light irradiated onto a sample is measured. By using extinction spectroscopy, the concentration c in mol/L of solutions and colloids can be determined if the extinction coefficients ϵ , the extinction E and the optical path length d in cm is known. The Beer-Lambert Law can be used as follows:

$$E = \log \frac{I_0}{I} = \epsilon \cdot c \cdot d \quad (5) \text{ Beer-Lambert law}$$

The double beam UV-Vis spectroscopic analysis was performed in the range of 190-350 nm (deuterium lamp) and 350-1100 nm (halogen lamp) in polystyrene cuvettes measuring the gold nanoparticle sample against the solvent reference cuvette.

In the case of DNA light is absorbed specifically at 260 nm which can be used to calculate the concentration by using approximate conversion factors of 50 $\mu\text{g}/\text{OD}_{260}$ for duplex DNA and 33 $\mu\text{g}/\text{OD}_{260}$ for single-stranded DNA. For analysis of origami structures 2 μL solutions were used for nanodrop UV-Vis absorption spectroscopy.

The characterization of gold nanoparticles with respect to their size, shape, functionalization, concentration, and stability can also be achieved by UV-Vis absorption spectroscopic analysis. Optical resonance of gold nanoparticles resulting in the absorbance by the localized surface plasmon is in the visible area of the electromagnetic spectrum (380-750 nm).

3.7.2. Transmission Electron Microscopy (TEM)

Nanostructures like gold nanoparticles and DNA origami cannot be resolved by light microscopy due to their size on the nanometer scale. This limitation is described by the Abbe' diffraction limit and is roughly about $\lambda/2 = 200$ nm for λ at 400 nm. [88] To overcome the diffraction limit in the visible region of the light, transmission electron microscopy (TEM) is used, which is based on accelerated electrons instead of a light source. The limiting wavelength of electrons grounds on their mass and their speed as described by Louis de Broglie. [89] They have a wavelength of ~ 3.7 pm at an acceleration voltage of 100 kV. Thus, resolutions on the atomic scale can be reached. The image itself is created by illumination of a sample in vacuum with an electron beam produced by a LaB₆ or tungsten filament cathode, respectively. While transmitting the specimen, the electrons can be partially scattered depending on the electron density and the thickness. Elements with higher atomic number and thus more charged scattering centers reveal a stronger interaction with the incident electron beam. For the transfer of specimen information to the electron beam, inelastic (e.g., electron-electron scattering with detectable energy loss) and elastic scattering (e.g., electron-nuclei scattering, very little or no energy loss) events of single electrons are important. After transmitting the specimen, the beam can be transformed in an image by using a phosphorus coated screen or a fiber optic coupled with a CCD camera.

For the visualization of gold nanoparticles, beside the removal of excess surfactants or buffer which crystallize while drying of the sample, no further staining procedure is necessary. The mass contrast of gold nanoparticles is sufficient for visualization with TEM. In contrast, the imaging of less electron-dense structures like DNA origami requires staining with high-Z elements like uranium, tungsten, or lead. For DNA origami, commonly aqueous solutions of uranyl acetate or uranyl formate is used. A typical staining procedure was carried out as follows:

6 μ L of a solution with 1 nM DNA origami were applied on a glow discharged (30 s, 15 μ A, 25 mbar) copper grid, covered with a continuous formvar-carbon film (Quantifoil, copper 400 mesh) and incubated for 60 s. Afterwards, the grid was blotted and 6 μ L of 1 wt % uranyl formate were added, incubated for 60 s and blotted for a second identical staining step. Finally, after the staining solution was blotted, the grid was air-dried. TEM imaging was carried out with an EM 910 (ZEISS) and a JEM 1400+ (JEOL) instrument, respectively, at 120 kV.

3.7.3. Agarose Gel Electrophoresis (AGE)

Agarose gel electrophoresis is a molecular biological method for size-dependent and/or charge-dependent separation of macromolecules. For separation, a 3D polymer matrix is used, consisting of

agarose molecules crosslinked into bundles. Molecules loaded in the pockets of the gel are moving along an applied electrical field through the gel and separated by their electrophoretic mobility. The pore size of a gel depends on the percentage of agarose used to form the matrix and can be estimated to be about 100-500 nm in a 1 wt % gel. [90]

AGE was used for purification and characterization of DNA origami structures after the assembly as well as for the analyzation and purification of AuNP binding inside Pandora's box.

If not stated differently, AGE purification was performed by using 1 wt % agarose in TBEMg 11 buffer (40 mM Tris, 20 mM boric acid, 2 mM EDTA, 11 mM MgCl₂, pH 8.0) and a 150 mL boiled-up solution was casted in a gel casting station and cooled down for 1.5 h to RT. Afterwards, the casting station was stored at 4 °C for 1 h prior to use. Immediately before starting the electrophoresis, the origami samples (10-100 nM) were mixed 1:10 with loading dye buffer (90 vol. % glycerol, 10 vol. % 10x TEMg 11) and loaded into the gel chambers. When gold nanoparticle colloids were analyzed or purified then 0.2 wt % Tween20 was added to the gel and the running buffer during electrophoresis. As control samples for analytical gels either the same amount of origami or 10 µL (10 nM) was loaded as well as a 1 kb DNA-ladder and scaffold (p8064). The gel itself was placed in an ice-water bath. The parameters for the electrophoresis are as follows: runtime 2 h, 80 V at 4 °C. In case that fluorophore labeled origami structures were used, imaging was performed prior to staining. If this was not the case then staining of gels were performed with 1:10,000 EtBr in TBEMg 11 buffer for at least 10 min followed by the imaging with the imaging system Typhoon FLA 9000 at a resolution of 25 µM/pixel or 50 µM/pixel.

The resulting origami bands, indirectly visible by EtBr staining during imaging or the reddish gold nanoparticle bands visible by naked eye, can be extracted from the gel using commercially available Freeze 'N Squeeze spin columns. Briefly, desired bands were cut out from the gel and placed inside the spin column followed by freezing at -20 °C for 5 min and centrifugation at 5,000 g at 10 °C for 10 min. The recovered intact origami structures or origami-gold nanoparticle conjugates from the centrifugation tube were analyzed by TEM and used for further experiments.

4. Results and Discussion

In last decades biosensing applications gained more and more attraction and developed into an important tool for personalized medicine and point-of-care diagnostics. Biosensing itself is used for the detection of chemicals, macromolecular substances (e.g., peptides, proteins, etc.) or in general external stimuli and is based on one biological as well as one physicochemical component. In commercially available systems like lateral-flow assays, the sensing itself is achieved by antibodies and the read-out is done by eye and relies on the physicochemical properties of gold nanoparticles. Strong absorption and scattering capability of nanoparticles are key factors in these biosensing techniques and can be used to detect antigens. Despite this common concept, both components can be varied in manifold ways. However, the readout itself can be of different nature and much more complex and sensitive than the simple visualization by naked eye. The special properties of gold on the nanoscale, namely the plasmonic activity, enable the use of different optical and spectroscopic techniques for the detection of readout signals. Relevant examples are surface-enhanced Raman scattering (SERS) [41, 42, 72, 91, 92], metal-enhanced Förster resonance energy transfer (M-FRET) [75, 93, 94] or switchable plasmonic chirality [77, 95]. The development of DNA origami by P. Rothemund in 2006 [17] enabled the spatial placement of gold nanoparticles with nanometer precision and initiated a paradigm shift in the field of biosensing. Ideally, a molecular biosensor should be able to generate a strong output signal allowing to detect single molecules. [41] This can be achieved by using the plasmonic properties of gold nanoparticles and especially gold nanoparticle dimers which feature a strong plasmonic coupling and strong electromagnetic field if their mutual distance is small enough (hot spot). The controlled arrangement of nanoparticle dimers at small nm-distances and the placement of molecules in the hot spots of those dimers can be therefore used to increase the Raman scattering signals by several orders of magnitude and even enable the detection of single molecules.

4.1. Finite Difference Time Domain (FDTD) Simulations of Electrical Field Enhancements in AuNP and AuNC Dimers

Finite difference time-domain (FDTD) or Yee's method is a numerical method for modeling the electromagnetic response of a system which involves the calculation of the approximate solutions of Maxwell's equations. [96] It is a widely used technique to examine the interaction of light and matter on the nanoscale and can be used to simulate the interaction of dielectric and metal micro/nano structures with an incident electromagnetic field. It is a time domain method, which allows us to simulate the response of the system in a broad range of frequency values in a single simulation and hence is especially useful in scenarios where the resonant frequencies of the system are unknown.

A FDTD simulation is set up by defining a computational domain, which is basically the region over which the solutions of Maxwell's equations are calculated. The structure for which the optical response is to be simulated is placed inside this computational domain. The structure's material properties are defined through its permittivity, permeability, and conductivity values over the wavelength range of interest. Subsequently, an electromagnetic field source is specified, which is used to illuminate the computational domain. The entire computational domain is then segmented (meshed) into distinct cells. The solutions of the time-dependent Maxwell's equations are then calculated at each of these distinct cells in a 'leapfrog' manner. i.e., the electric field components in a certain cell are calculated at the first instant of time and then the magnetic field component is calculated for the same cell at the next instant. This process is iterated until the electromagnetic field inside the computational domain decays below the pre-defined threshold value.

The FDTD simulations presented in this dissertation were carried out by Jesil Jose with the software Lumerical FDTD.

4.1.1. Surface-Enhanced Raman Scattering

SERS enhancement factors are an important tool to estimate the resulting Raman signal intensity of molecules placed inside the cavity of a gold nanoparticle dimer. FDTD simulations were carried out to examine the electric field enhancement around the nanostructures due to the plasmonic coupling. Even though the FDTD cannot model a Raman process, the enhancement in Raman scattering (SERS) of a molecule attached to the nanoparticles can be calculated from the local electric field enhancement around the nanoparticle. The SERS enhancement factor (SERS EF) $[(E_{loc}/E_{inc})^4]$ at a certain wavelength is calculated as the fourth power of the local electric field enhancement (E_{loc}/E_{inc}) at that wavelength. [97]

The computational domain is defined as a $1\ \mu\text{m} \times 1\ \mu\text{m} \times 1\ \mu\text{m}$ cubic region. The refractive index of the domain is set to be 1.33. A perfectly matched layer (PML) boundary condition is applied at the domain boundaries to absorb all the incident electromagnetic fields so that there will not be any back-reflections into the simulation region. A total simulation time of 200 fs is specified, and an early termination is allowed if the amplitude of the total electric field decays to 10^{-5} times of its initial value. The gold nanoparticle dimers were placed at the exact center of the computational domain. The dielectric permittivity of gold is taken from the experimental data by Johnson and Christy. [98] Initially a total-field scattered-field (TFSF) source is used to illuminate the domain to simulate the scattering spectra of the dimer structures. Subsequently 2-D frequency domain field profile monitors were used to compute the local electric field profile inside the gap and around the nanostructures at the resonance wavelength (λ_{max}).

The dimensions of the spherical and cubic gold nanoparticles used in this dissertation are limited by design constraints of the used DNA origami. The overall length of the scaffold is an upper limit with respect to the available size of the material. Also the bilayer design of the DNA origami box, the space between the gold nanoparticles and the box itself together with the persistence length of hybridized DNA must be considered. Thus, different dimensions (18 nm and 10 nm) and shapes (cube and sphere) with different gap distances (15 nm and 2 nm) of dimers were simulated. **Figure 21** shows the false color image of the SERS enhancement factor ($|E^4|$) distribution of two gold nano-cubes with 18 nm edge length and 2 nm edge curvature, separated by a gap distance of 15 nm (A) and 2 nm (B) apart. Shown are the XY-plane (A left, B left) as well as the YZ-plane (A right, B right).

Gap distances used for the simulations are derived from the designed DNA origami platform Zelos with respect to the endpoints of the dynamic system as shown in **Figure 17**. Simulations revealed that the highest SERS enhancement factors for AuNC dimer with a gap distance of 2 nm are located at the edges due to the increased coupling of the individual cube plasmons at sub-five-nanometer gap. This state is referred as the 'ON'-state. The Raman signal enhancement of a reporter molecule inside the gap can be estimated to be 1.35×10^6 at the corners and roughly 4.5×10^5 at the edges. Even over the lateral facet of the gold nanoparticle dimer, the enhancement factor is around 10^5 , creating a hot-spot with a large volume. Increasing the gap distance to 15 nm reduces the $|E^4|$ value by half at the edges of the single cubes and by five orders of magnitude at the lateral facets inside the gap. Due to this significant reduction in SERS enhancement factor, this state with 15 nm gap distance is referred as the 'OFF'-state.

In the same way, as the size of the AuNC is decreased (10 nm edge length), the SERS EF values are reduced (**Figure S 3**). Highest values are around 3.2×10^4 at the corners of dimerized AuNC with a gap distance of 2 nm.

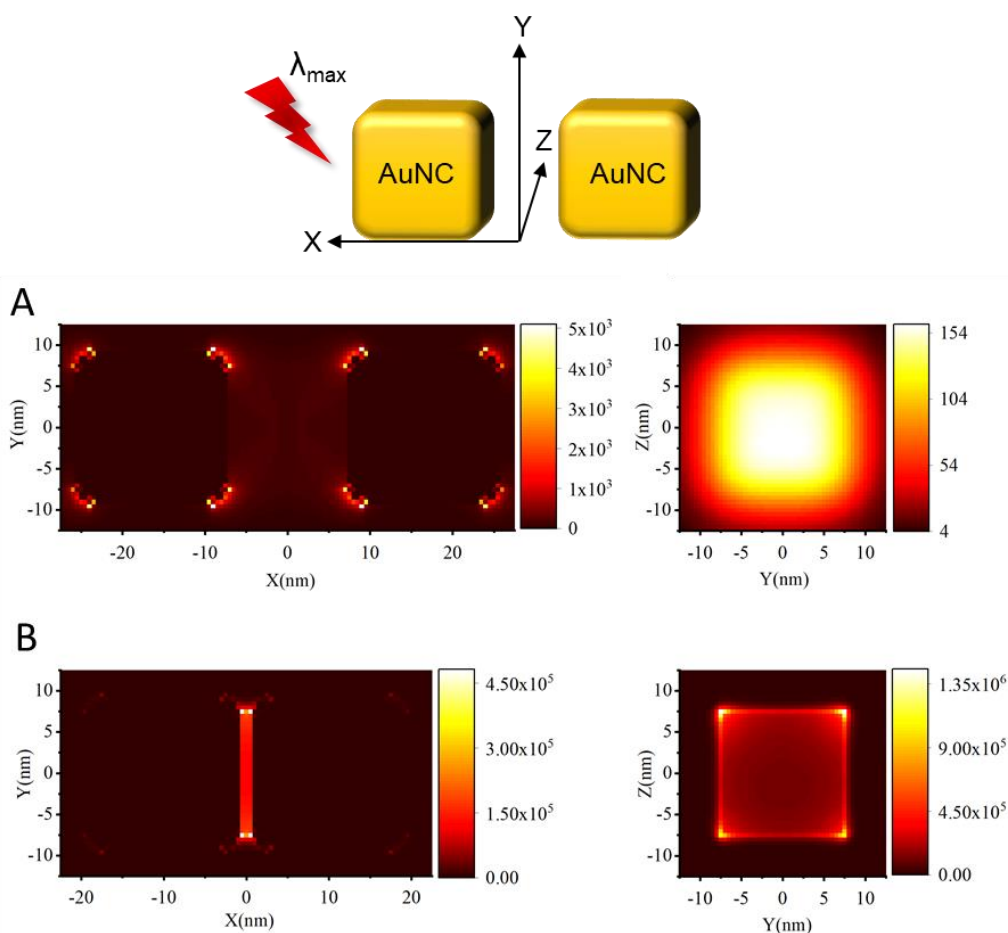


Figure 21: FDTD simulations of SERS enhancement factors $|E_{loc}^4|$ of 18 nm AuNC dimers with 2 nm curve-edge radius at (A) 15 nm and (B) 2 nm gap distance. The different perspectives in the XY-plane (left) and YZ-plane (right) are shown. FDTD simulations were performed with a TFSF (Total field scattered field) white light source and the data represents the SERS EF values at λ_{max} of the coupled longitudinal dipolar plasmon (LBDP) mode of the sphere dimer.

Using gold nanoparticles with different shapes and sizes requires a careful evaluation of their plasmonic properties with respect to the resultant electric field distribution. This distribution can strongly vary upon small changes in shape or size of the gold nanoparticles. Especially, upon dimerization of particles, there is a drastic increase in local electric field intensity in the gap due to plasmon coupling. **Figure 22** shows FDTD simulations of SERS enhancement factor ($|E^4|$) values of two spherical gold nanoparticles with a 15 nm gap distance (A) and a 2 nm gap distance (B). Highest $|E^4|$ enhancement factors in dimers with 2 nm gap distances are about 7.50×10^6 and this enhancement is strongly localized in the gap region. As the interparticle distance increases to 15 nm, there is a drastic reduction in the SERS enhancement factor in the gap region due to the reduction in plasmon coupling. The highest value of SERS EF in this case (5×10^3) is directly related to the individual sphere plasmon

mode rather than the coupled plasmon mode. This is clearly understood from the localization of high SERS EF values close to the edges of the spheres rather than in the gap (**Figure 22**, A, left).

The potential signal enhancement of gold nanoparticle dimers in the 'OFF'-state (15 nm interparticle distance) are comparable irrespective of their shapes. Gold nanocubes as well as gold nanospheres have similar $|E^4|$ values. However, the plasmon coupling differs drastically at lower gap distances as a direct result of their distinct geometries. Dimers of AuNPs reveal between five- and tenfold higher $|E^4|$ values compared to AuNC dimers. Conversely, the reached hotspot volume is around tenfold higher using AuNC dimers which can be favorable for sterically demanding molecules or binding events. Like the case in AuNC, as the size of the AuNP is decreased (10 nm diameter) the overall reached SERS enhancement factors are smaller (**Figure S 4**). Highest values are around 1×10^5 inside the hot spot of dimerized AuNP with a gap distance of 2 nm. However, even those enhancement factors can lead to a detectable SERS signal if small Raman reporters with an intrinsic high scattering cross-section are used.

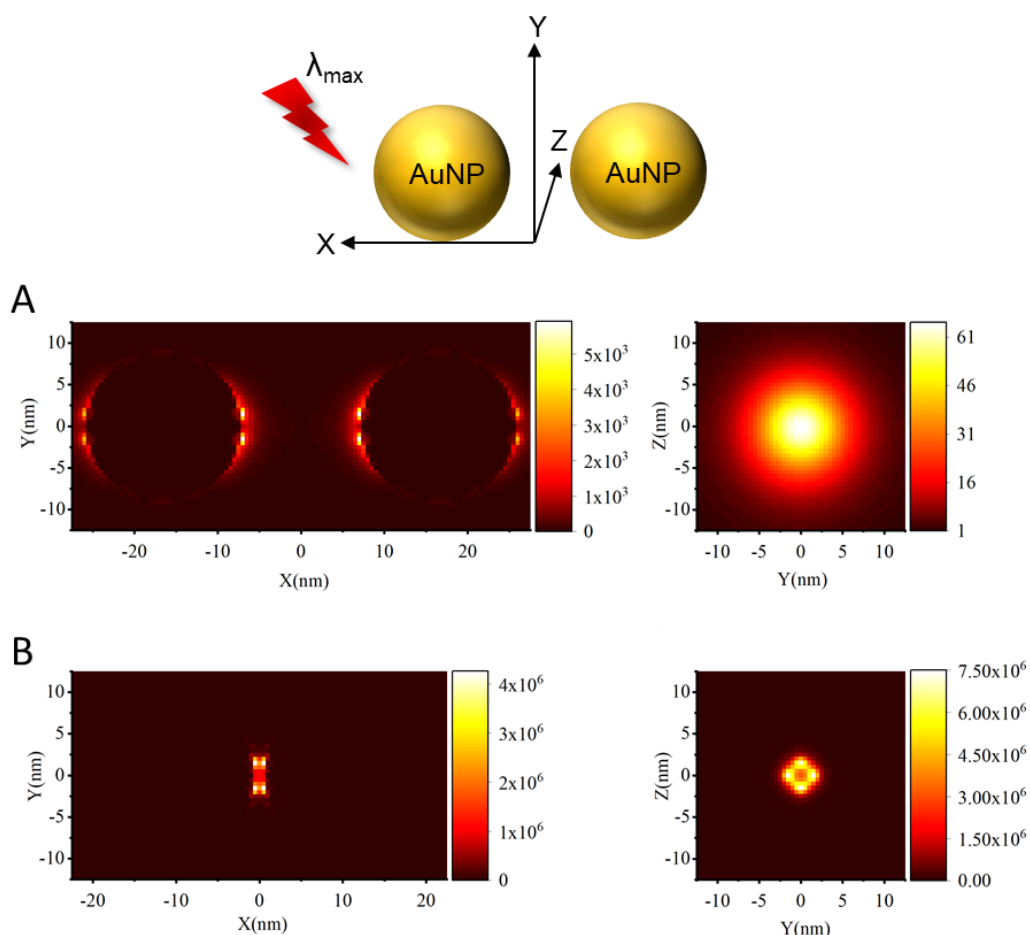


Figure 22: FDTD simulations with resulting SERS enhancement factors $|E_{loc}^4|$ of 18 nm AuNP dimers are shown. Scheme of the planes as well as 15 nm (A) and 2 nm (B) gap distances in the XY-plane (left) and YZ-plane (right) are shown. FDTD simulations were performed with a TFSF (Total field scattered field) white light source and the data represents the SERS EF values at λ_{max} of the coupled longitudinal dipolar plasmon (LBDP) mode of the sphere dimer.

More importantly, this increased hotspot volume reached for AuNC dimers enables receptor-ligand binding studies with high dissociation constants. Effective binding with vibrational spectroscopic detection of the binding event makes high concentrations of the ligands necessary like in the case of supramolecular ligands. [99-101] Local ligand concentrations within the gap can reach low molar regimes following experimental quantification of the thiol coverage efficiency on {100} and {111} gold facets. By assuming a thiol moiety footprint of 1 nm^2 and a gap 18 nm in length and width as well as 2 nm in space, a local gap concentration of 0.83 M can be calculated. Considering the published thiol footprints in literature, the size of the ligand itself is of greater importance. For example, for benzenethiol a value of 4.3 molecules per nm^2 on planar Au {111} facets were published by Wan *et al.* in 2000. [102] For 1-dodecanethiol a value of 2.2-3.1 nm for spherical citrate-stabilized AuNP with a size of 35-40 nm were published by Park and Shumaker-Parry in 2015 [103] which result in a mean footprint of 0.23-0.46 thiols/ nm^2 . However, the ligand exchange of Tween20 present on the Au {100} facets of AuNC or AuNP inside the DNA origami boxes by thiolated ligands like the molecular tweezer CLR01 [104] has to be analytically investigated for quantitative ligand-receptor binding studies. If the number of ligands as well as the number of receptors inside the gap is known, association constants can be derived using the changed Raman signals upon binding. While the quantification of ligands inside the gap is of great interest for the binding to the receptor itself, it is also necessary for the comparison of the Raman signal strength generated by a single AuNC-dimer-Origami device with respect to the simulated SERS EF values.

4.2. Synthesis and Characterization of AuNP/AuNC with Different Size, Shape and Surface Functionalization

Synthesis of gold nanoparticles with different size and geometry has been described and carried out in literature since decades. However, specialized applications like SERS spectroscopy need gold nanoparticles with a great control over size and shape with respect to their standard deviation of their mean size and their faceting. This is conditioned by strong variations of the electrical field of an excited oscillating localized surface plasmon by even slight changes in the shape or size of a gold nanoparticle, especially in anisotropic nanoparticles. Also, the crystal structure of a single gold nanoparticle is of great importance, since lattice defects disturb the oscillation of electrons by damping processes, too. Consequently, single crystalline gold nanoparticles with a high monodispersity and a high shape yield are preferred for spectroscopic applications since they enable control over the physical parameter of the electrical field formation and thus control over the hotspot.

The following sections describe the synthesis of monodisperse spherical gold nanoparticles (4.2.1) and gold nanocubes (3.2.2) with sizes ranging from 8 nm to 26 nm as well as their functionalization and characterization (4.2.3) for further conjugation to DNA origami.

4.2.1. Spherical Gold Nanoparticles

Spherical gold nanoparticles are possibly the oldest and most widespread type of particle synthesized. The synthesis itself can vary depending on their application, the need for specific surface functionalization or the avoidance of toxic or disturbing molecules like specific surfactants while further use. The AuNP used in this thesis were synthesized using a seeded and surfactant-based synthesis since the formation of monodisperse cluster in the size regime of 1-1.5 nm ensure a uniform growth during the first growth step. [81, 105] A high monodispersity is conventionally characterized by a standard deviation $\leq 10\%$ the AuNP size. [106]

Indeed, the fast and reproducible synthesis as well as the easy upscaling to liter scale makes the surfactant-based synthesis of AuNP favorable for the application in this thesis although it makes a ligand exchange necessary. Shown in **Figure 23**, AuNP with 14.5 nm (A), 11.5 nm (B) and 7.6 nm (C) were synthesized. Statistical analysis of TEM images reveals a standard deviation 0.7 nm and 0.6 nm with $n \geq 100$, respectively. Plasmonic properties of gold nanoparticles with respect to their size, shape, concentration as well as stability can be derived by using UV-Vis extinction spectroscopy as shown in **Figure 23** (D). [80, 107-109] Each normalized AuNP extinction spectrum reveals a single narrow plasmon band with a plasmon peak at 516 nm (7.6 nm AuNP), 518 nm (11.5 nm AuNP) and 521 nm (14.5 nm). This validates the colloidal monodispersity derived by TEM images on the scale of several

hundred AuNP. Plasmon modes visible in UV-Vis extinction spectra are caused by the surface plasmon excitation. The small but clearly measurable redshift of the plasmon mode is caused by the increasing particle size which is in good agreement with the underlying Coulomb law mechanism of decreasing restoring force with simultaneously increasing particle diameter. Thus, the resonance frequency is smaller and thereby the plasmon peak occurs at higher wavelengths.

As mentioned before, the synthesis of single-crystalline gold nanoparticles is, with respect to their plasmonic properties like hotspot formation, of great interest. Thus, much effort has been devoted to optimizing the synthesis and understanding the synthesis mechanism by many groups during the last decade. [105, 106, 110, 111] A key player of surfactant-based nanoparticle growth is the soft template of the surfactant micelle. This micelle is generated if the individual critical micelle concentration of a surfactant is reached (e.g., CTAB \sim 1 mM) [112] and has a size (depending on the temperature) of \sim 4-5 nm. [113] Inside these micelles, nanocluster formation takes place, while reduction of Au(III) with the strong reducing agent NaBH₄. Later, these gold clusters with a size of 1-1.5 nm grow in an isotropic manner by using CTAC since Cl⁻ ions does not preferentially bind to a distinct facet of the gold nanoparticles in contrast to other halide ions. [114] For this reason, low-index facets, namely {100} and {111}, are distributed equally over the AuNP surface, leading to quasi-spherical AuNP. Of course, also super-spherical AuNP can be synthesized with different sizes as reported in literature by using stepwise oxidation and edging of the exposed edges of the gold lattice. [32, 115]

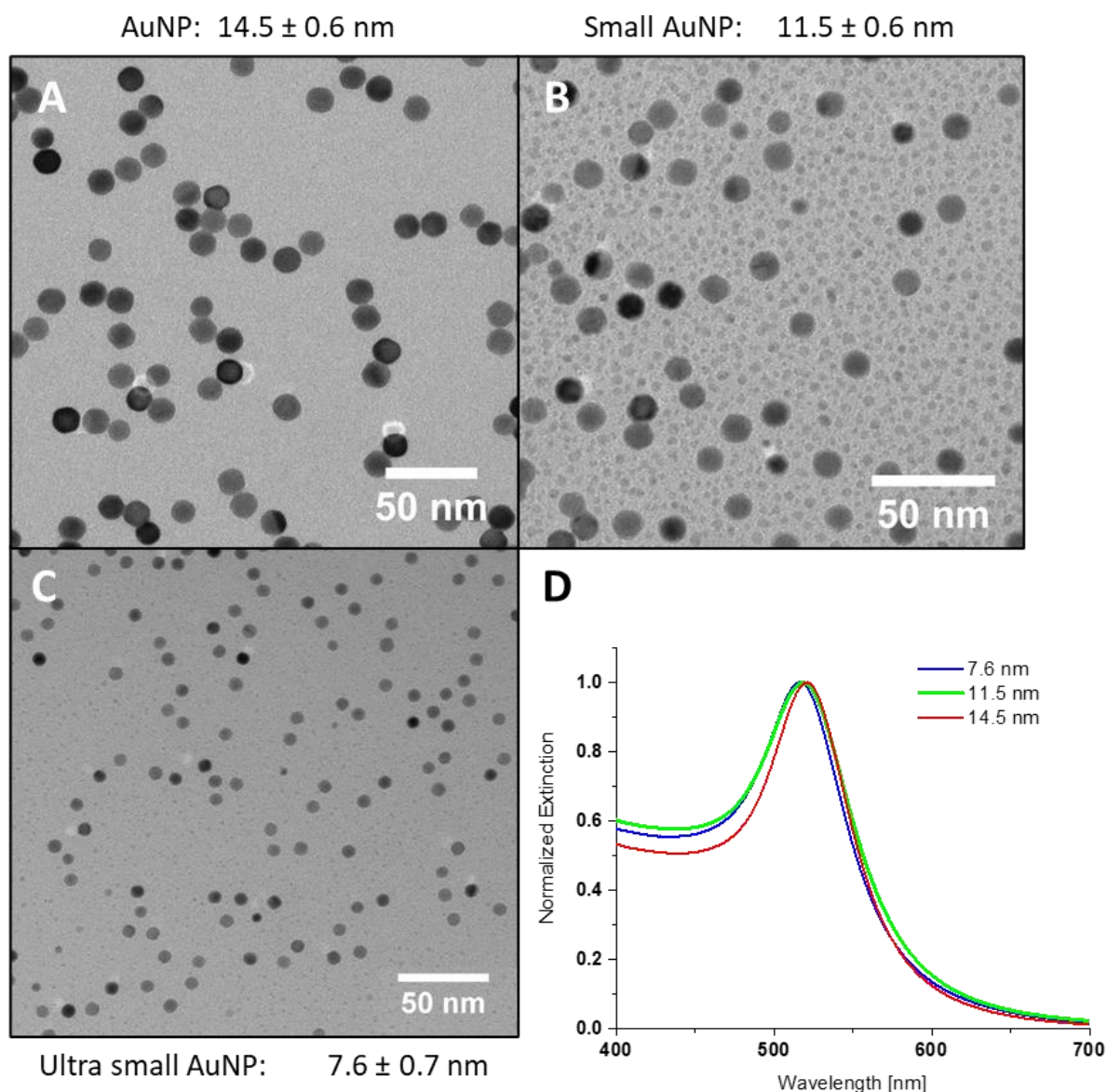


Figure 23: Representative TEM images of AuNP with different sizes (A, B, C) synthesized according to a modified synthesis of Park et al.. [81] Normalized UV-Vis extinction spectra of AuNP with different sizes (D). A red-shift of the plasmon mode from 516 nm to 521 nm due to the increasing AuNP size is visible. For statistical analysis $n > 100$ particles were measured.

4.2.2. Gold Nanocubes

The creation of new anisotropic plasmonic nanostructures has been heavily studied in the past years for the reason of their special plasmonic properties and multiple potential applications (e.g., gold nanorods, gold nanocubes, gold nanostars). As described and simulated before (**Figure 21**), anisotropic gold nanoparticles like AuNC reveal a specially enhanced electric field distribution resulting in hotspot formation at the corners and edges of the AuNC. This enables highly sensitive detection of molecules using SERS. Overall, the flat facets of AuNC makes them interesting as a building block for higher

hierarchical structures. [116, 117] The highly reproducible large scale synthesis of gold nanocubes with a high shape yield is of great importance and was extensively studied in literature. [81] To understand the mechanism of particle formation, the microscopic origin of the anisotropic growth of AuNC formation must be elucidated which is based on the gold crystal lattice. The face-centered cubic crystal lattice of gold can be described with the Miller indices which denote distinct planes. All surface facets of a perfect AuNC can easily described with the Miller indices {100}, {010} and {001}. The overgrowth of other facets present on gold clusters (e.g., {111} and {110}) or gold seeds by addition of halide ions is a widely used procedure for AuNC formation with sizes ranging from 16 nm to larger than hundred nanometers. [81, 118-120] It is well known that the surface energy (γ) differs between different facets of gold crystals ($\gamma_{\{111\}} < \gamma_{\{100\}} < \gamma_{\{110\}}$) which leads to the formation of low-energy equilibrium conditions. [121] Consequently, small gold nanoparticles reveal a regular and truncated decahedral (consisting of {111} planes) or cuboctahedral (consisting of {111} and {100}) shape. By carefully minimizing the local Au(III) reduction on the {100} facet upon addition of surfactants or Br⁻ ions, the growth rate is decreased, resulting in the overgrowth of the {111} facet which finally vanishes. [81, 105, 114, 120, 121] Currently, size limitations regarding the smallest achievable edge length make the development of a seedless synthesis for ≤ 15 nm AuNC necessary, as described before (23).

Figure 24 (A-D) shows TEM images of AuNC with different edge lengths synthesized for this thesis. Edge lengths of the cube can be varied from 6.9 nm to 25.9 nm with a size distribution between 0.8 nm and 1.1 nm. Overall, the shape yield of the synthesized AuNC with different techniques is around 78 % after centrifugation and around 80 % for ultra-small AuNC. Owing to the fact, that in literature only AuNC with an edge length of ≥ 17 nm are described, the shape yield of AuNC synthesized for this thesis is sufficient. Other species present in the AuNC samples are gold nanorods and gold nanotriangles, whereby the appearance of rods is limited to AuNC samples ≥ 20 nm. It has to be mentioned here that the reproducibility decreases with decreasing size and thus has to be further optimized to avoid batch-to-batch differences and get more control over the reaction conditions and mechanisms. However, the exhibited plasmon peaks of the differently sized AuNC shown in **Figure 24** (D) can be well compared because of similar shape yields and standard deviations of the edge length. Like the AuNP described before, the AuNC reveal a single but broadened plasmon peaks at 526 nm (9.6 nm AuNC), 535 nm (18.1 nm) and 541 nm. As published in literature before, the shape of gold nanoparticles strongly influences their optical properties. [122, 123] Thus, a small redshift upon formation of edges and vertices is visible in UV-Vis absorption spectra. Extinction at wavelengths above 575 nm are assignable to impurities by triangular- and rod-shaped gold nanoparticle; especially the gold nanorods exhibit a strong longitudinal plasmon peak. [124, 125]

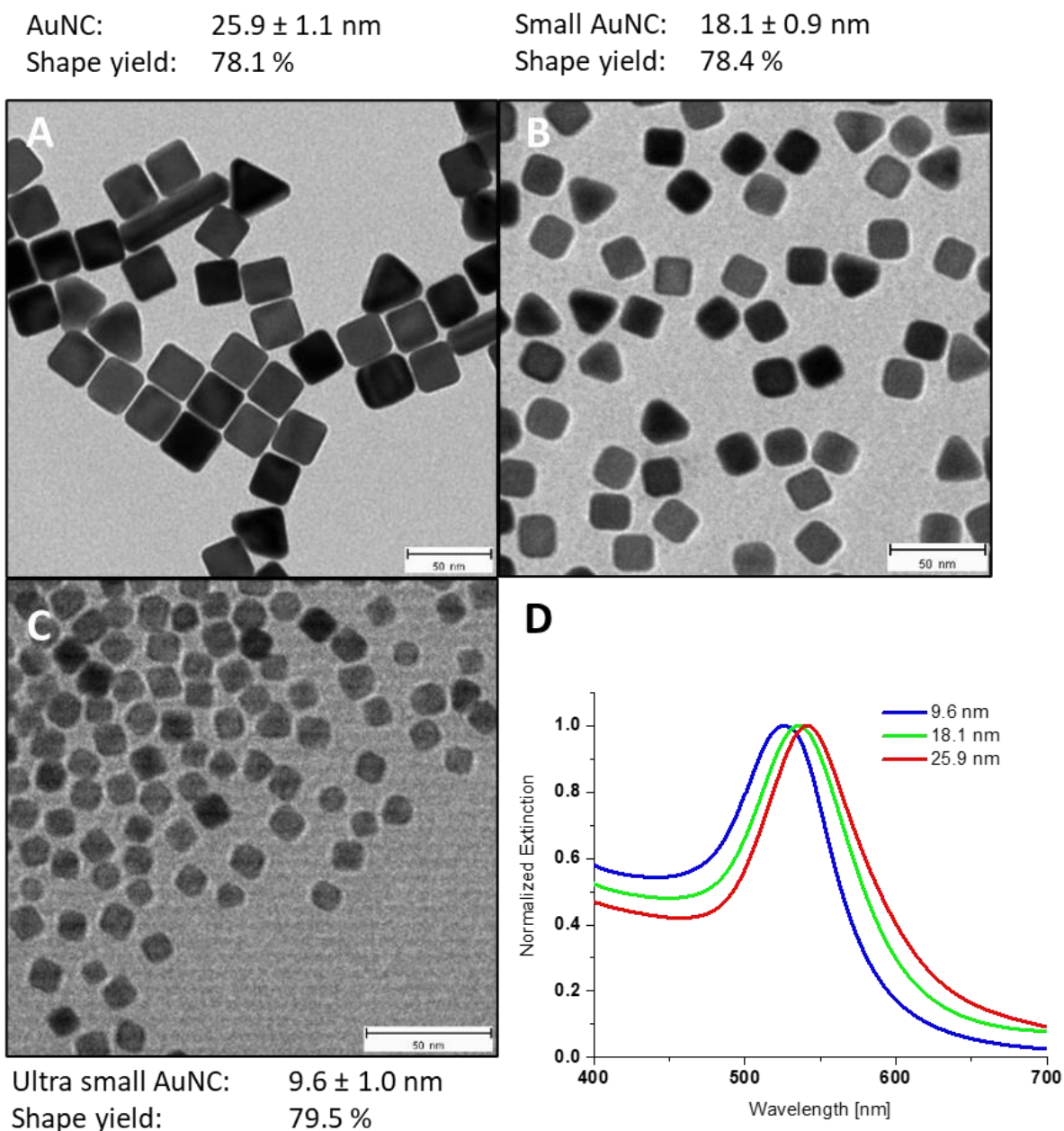


Figure 24: Representative TEM images of AuNC with different sizes (A, B) synthesized according to a modified synthesis of Park et al.[81] Representative TEM image of ultra-small AuNC (C) synthesized with a seedless CTAC-based synthesis is shown (scale bars = 50 nm). Normalized UV-Vis extinction spectra of AuNC with different sizes but comparable shape yield. A red-shift of the plasmon peak from 526 nm to 541 nm due to the increasing AuNC size is visible. For statistical analysis $n > 200$ AuNC were measured.

4.2.3. Functionalization and Characterization

Base hybridization is a widely used technique for the combination of gold nanoparticles and DNA origami to achieve a precise and programmed placement of gold nanoparticles with various shapes and sizes onto or into DNA origami nanostructures. However, this technique presupposes that the gold nanoparticles are covalently functionalized and covered with thiolated oligonucleotides that are complementary to the target sequence either of the scaffold or a protruding staple. Only few publications address the challenge of clearing a hotspot for binding of sterically demanding molecules like proteins or the avoidance of vibrational spectroscopic background signals from the DNA. [41, 91, 95, 126] Thus, it is highly desired to implement another conjugation mechanism for stable conjugation of DNA origami with large gold nanoparticles as first described by Endo *et al.* in 2011. [127] In their work, they used bis-thiolated oligonucleotides placed on a 2D DNA origami slit for the patterning of the origami with 5 nm large and electrostatically coated AuNP. Using bigger AuNP is still challenging because of the reduced stability of large AuNP at high ionic strength.

To compare the internalization yield of Tween20-stabilized gold nanoparticles with various shapes and sizes into Pandora's box via thiol-chemistry, AuNP functionalized with ssDNA were synthesized and characterized via TEM, UV-Vis absorption spectroscopy and DLS as shown in **Figure 25**. The previously synthesized spherical AuNP (4.2.1) with a diameter of ~ 10 nm were functionalized with thiolated oligonucleotides whose sequence is complementary to the protruding staples sequence inside Pandora's box as described in section 3.3.2. By using uranyl formate as contrast agent in transmission electron microscopy (TEM), structures with a low atomic number (Z) can be either positively or negatively contrasted and thus visualized in TEM. Staining mechanisms can be based on intercalation or electrostatic interaction of heavy metal atoms (e.g., uranyl, molybdenum, or tungsten) with biomolecules or the interaction with the glow-charged carbon layer onto the TEM grid. However, staining depends strongly on the target biomolecule, the pH, and the concentration of the staining solution. [128, 129] Gold with a relatively high Z number does not require staining for visualization in contrast to soft matter like surfactants (e.g., CTAC, Tween20) or DNA origami. **Figure 25** (A) reveals the different coatings of AuNP used in this dissertation, namely CTAC, Tween20 and ssDNA. CTAC shows no interaction with the cationic uranyl molecules of the staining solution (A, left). Thus, the CTAC micelle around the AuNP stabilized with CTAC cannot be visualized in TEM. In contrast, the non-ionic and sterically demanding Tween20 surfactant molecules located on the gold nanoparticle are visible as a bright corona with 5.5 ± 1.2 nm thickness around the AuNP in stained TEM samples (A, middle). The compactness of the Tween20 layer prevents the penetration by uranyl molecules. By way of contrast, the cationic uranyl molecules strongly interact electrostatically with the ssDNA located on the AuNP surface of ssDNA-functionalized AuNP and enlarge the electron scattering properties of the

ssDNA layer visible as a 2.8 ± 0.45 nm broad dark corona (A, right). The successful ligand exchange can also be detected by dynamic light scattering (DLS) which reveals an increased hydrodynamic mean radius (HDR) ranging from 11.96 nm (CTAC) over 11.88 nm (Tween20) to 14.21 nm (ssDNA). Beside the direct visualization with TEM and the detection of the increased HDR upon functionalization at the ensemble level, also UV-Vis extinction spectroscopy can be used to control the stability as well as successful functionalization. Aggregation of AuNP while functionalization is observable as a spectral shift of the plasmon peak to longer wavelengths due to plasmon coupling. Ligand exchange of AuNP and covering of the AuNP surface also result in a change of the local refractive index (LRI) near the AuNP and a changed local dielectric environment. [130-133] An increased refractive index leads to a red-shift and *vice versa*. The correlation between the adsorption of molecules on a AuNP and the LRI can be described by the following equation for an exponentially decaying electrical field [132]

$$\Delta\lambda_{max} = \eta B (RI_{molecule} - RI_{medium}) \times \left(1 - e^{-\frac{2d}{L}}\right) \quad (6) \text{ Local refractive index description}$$

where $\Delta\lambda_{max}$ is the spectral shift and ηB is the overall bulk LRI sensitivity of the AuNP, d is the thickness of the layer of adsorbed molecules and L is the electrical field decay length. This equation shows that the spectral shift upon functionalization of AuNP with molecules strongly depends on the surface density of adsorbed molecules as well as the thickness of the layer on the surface. It is known that CTA⁺-based surfactants form a dense bilayer on the AuNP surface, its removal by oxygen plasma treatment reveals a strong blue-shift of λ_{max} . [132] Thus, exchanging the CTAC layer by an assumable less dense layer of the branched Tween20 polymer exhibited a blue-shift of 6 nm visible in UV-Vis extinction spectra as shown in **Figure 25** (B). After functionalization with a dense layer of ssDNA by using a salt-aging method to enlarge the ssDNA loading on the surface, the UV-Vis extinction spectrum displays a red-shift of 3 nm. As previously stated, the quantification of the spectral shift after functionalization requires detailed information about the loading density of the molecules on the surface and cannot be explained exclusively by using published RI values of adsorbed molecules (RI, CTAC = 1.44, Tween20 = 1.50, ssDNA = 1.46). [130, 132] With respect to the RI values of the different molecules present on the AuNP surface, a red-shift after functionalization with Tween20 is expected. The experimentally determined blue-shift of 6 nm underlines the different loading densities on the AuNP surface of the different ligands. However, the successful functionalization can be demonstrated by using different methods as shown before.

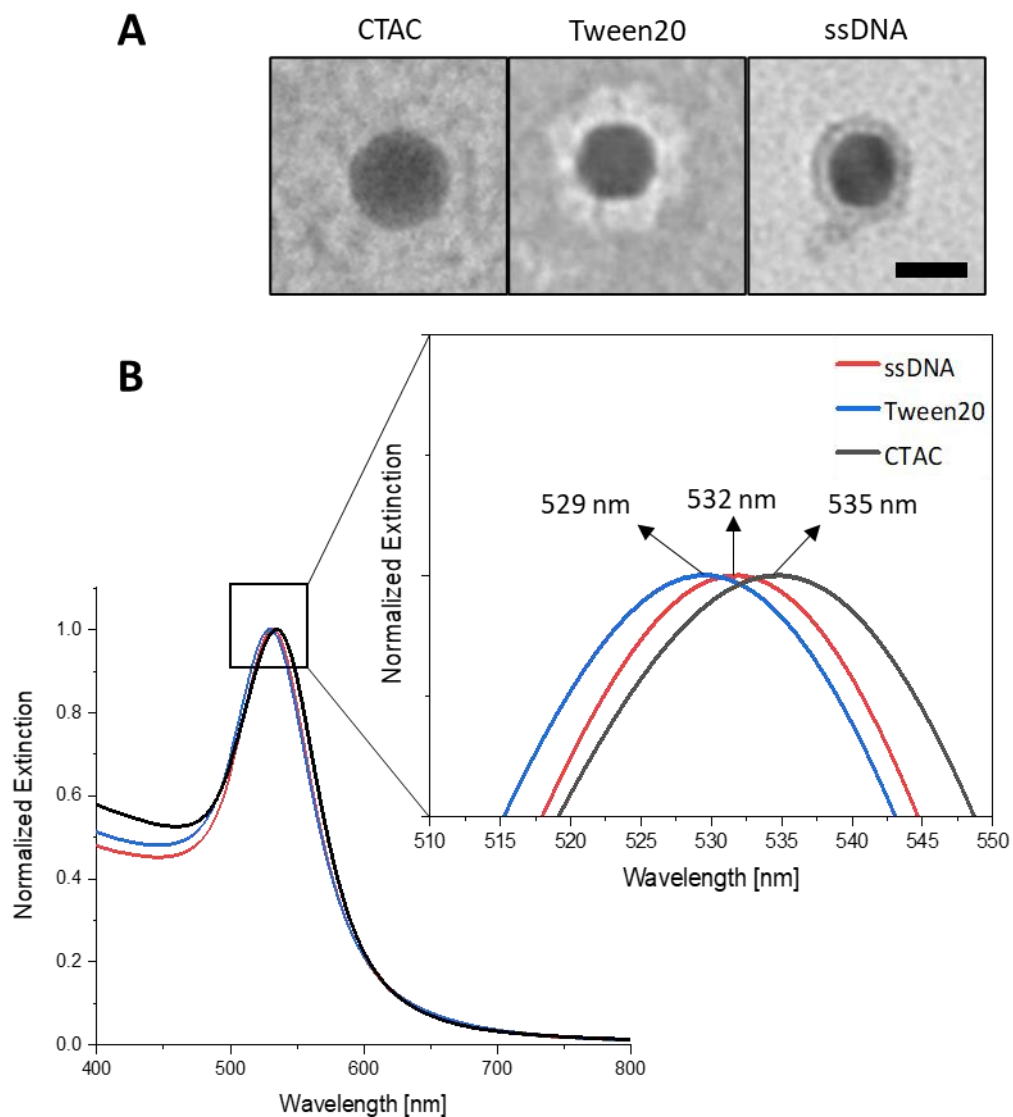


Figure 25: TEM images of 10 nm AuNP with different surface modifications (CTAC left, Tween middle, ssDNA right), stained with uranyl formate for visualization (A, scale bar = 10 nm). UV-Vis extinction spectra of AuNP with different surface modifications (CTAC, Tween20, ssDNA) (B). Normalized spectra show a red-shifted plasmon peak from 529 nm (Tween-functionalized AuNP) to 532 nm (ssDNA-functionalized) caused by the changed dielectric environment of the AuNP.

4.3. Colloidal Stability of Gold Nanoparticles in Origami Buffer Systems with High Ionic Strength and Its Enhancement by Surface-Active Molecules

The combination of gold nanoparticles with DNA origami requires sufficient stabilization of gold nanoparticles against aggregation induced by high ionic strength of the buffer which itself is necessary to ensure structural integrity of DNA origami. The stabilization of gold nanoparticles via functionalization of gold nanoparticles with thiolated oligonucleotides is widely used; this also enables the targeting of specific locations inside the DNA origami. Small gold nanoparticles can be stabilized under high ionic strength in origami buffer containing NaCl instead of MgCl_2 by using electrostatic interactions with small molecules like BSPP. [127, 134, 135] In contrast, if Mg^{2+} ions are present in the origami buffer system as recommended for complex 3D origami designed as square lattice, the AuNP quickly aggregate; this is recognized by the appearance of plasmon coupling peaks in the UV-Vis extinction spectrum. Beside this, the general unspecific interaction of bare gold nanoparticles with DNA origami while conjugation must be prevented to avoid aggregation of AuNP and disintegration of DNA origami. Furthermore, many cationic surfactants like CTAB used to stabilize or synthesize gold nanoparticles are present in the colloid and strongly interact with the negatively charged phosphate backbone of DNA and lead to compaction followed by disintegration. [136]

In this section systematic studies about the colloidal stability of AuNP with 18 nm edge length were carried out and the results are shown in **Figure 26** (A-E). Five different molecules were tested as stabilizing agent to achieve colloidal stability under high ionic strength in buffers containing different concentrations of MgCl_2 . The Mg^{2+} concentrations were varied between 0 mM and 100 mM in 1x TE buffer. UV-Vis extinction spectroscopic analysis was carried out after 24 h of incubation after setting the buffer concentrations to the described values. Shown are the normalized extinction spectra.

Figure 26 (A) shows the results of the aggregation assay using CTAB stabilized AuNC. The AuNC are stored in 5 mM CTAB after synthesis and exhibit a single plasmon peak at 528 nm; this colloid is referred to as stable. However, upon addition of 1x TE buffer (pH 7.4) as well as 1x TE buffer containing 4 – 100 mM, the colloidal stability is negatively influenced and the AuNC aggregate nearly immediately as indicated by a strongly decreasing plasmon peak at 528 nm. Depending on the aggregation state, a broadening and shifting of the plasmon peak is visible in the red and NIR region. The other tested surface-active molecules like SDS (0.5 wt. %), citrate (5 mM) and BSPP (10 mM) reveal distinct capabilities of providing colloidal stability. For instance, SDS with 0.5 wt. % stabilizes the colloid up to 6 mM of Mg^{2+} ions before aggregation occurs visible through a clear plasmon peak at ~740 nm (B). In contrast, citrate-based stabilization, e.g. achieved in AuNP synthesized by the commonly used Turkevich synthesis [137, 138], are only stabilized until 2 mM of Mg^{2+} ions (C). Similarly, 2 mM of Mg^{2+}

ions destabilize BSPP-stabilized colloidal suspension of AuNC (D). Finally, Tween20 as shown in **Figure 26** (E) ensure colloidal stability independently of the Mg^{2+} concentration which makes it the most suitable candidate for conjugation of gold nanoparticles and DNA origami.

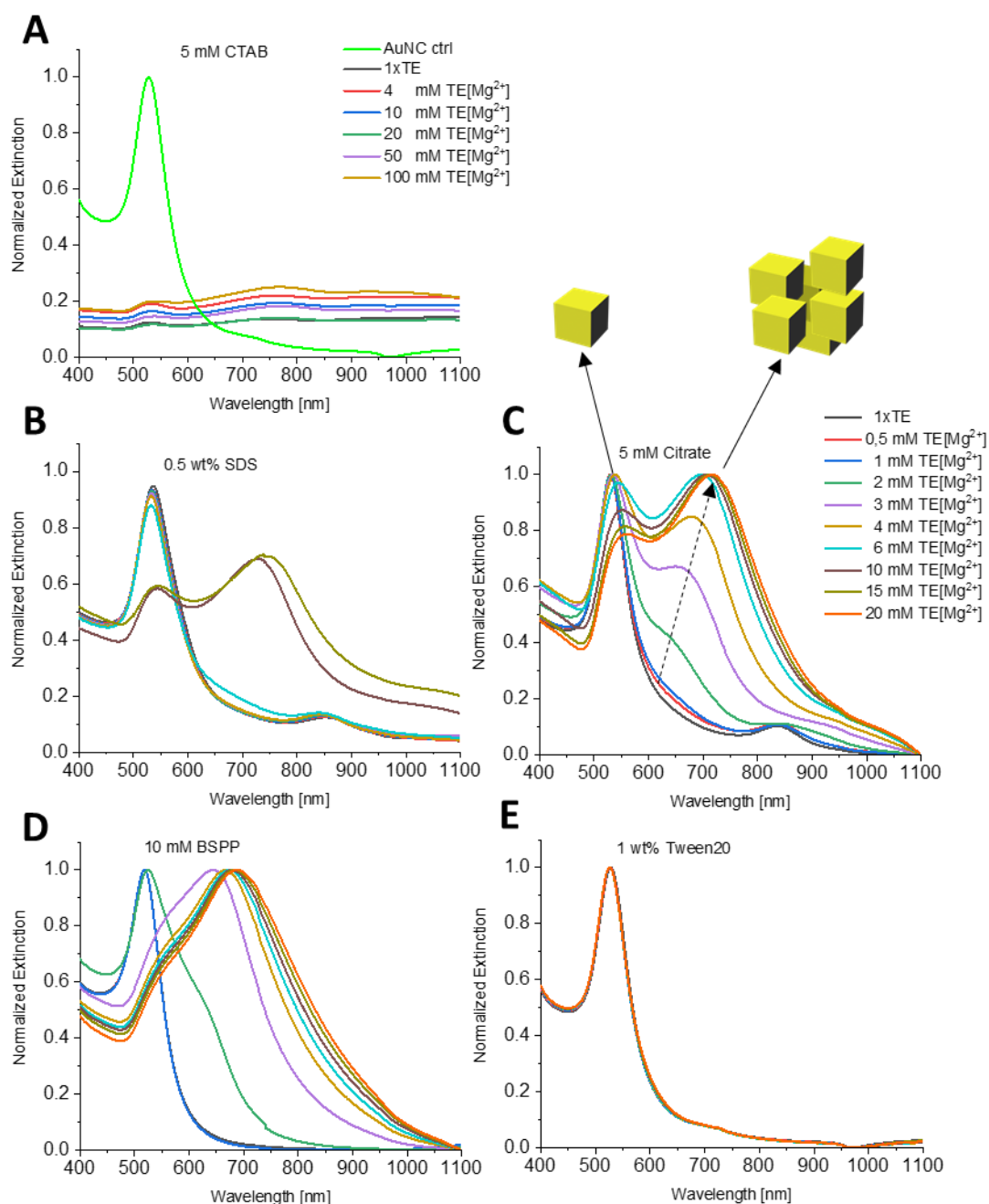


Figure 26: UV-Vis extinction spectroscopic for probing colloidal stability. The stability of differently stabilized AuNC (5 mM CTAB (A), 0.5 wt% SDS (B), 5 mM citrate (C), 10 mM BSPP (D), 1 wt% Tween20 (E)) in DNA origami buffer system with varying molarities of $MgCl_2$ were determined. A red-shift of the plasmon mode indicates the aggregation of the AuNC. The used maximum concentrations of the surface-active molecules are either derived by published ligand-exchange protocols or experimentally by the interaction of the surface-active molecules with the DNA origami followed by disintegration. [82, 83] The origami buffer system consists of 20 mM Tris, 2 mM EDTA, 0-100 mM $MgCl_2$, pH 7.6. The UV-Vis extinction spectra were recorded after one day of incubation.

The experimentally determined different ability of stabilizing AuNC at high ionic strength can be explained by applying the Derjaguin-Landau-Verwey-Overbeek theory (DLVO) on the present colloidal system as well as the special properties of AuNC. The DLVO theory was independently elaborated by E. Verwey and T. Overbeek in 1948 [139] based on fundamental work of P. Debye and E. Hückel (1923) [140] as well as B. V. Derjaguin and L. Landau (1941) [141]. Until today, the DLVO theory is the fundamental theory for explanation and prediction of colloidal stability for colloids that are not sterically stabilized; the theory is built on two components: First, the Van der Waals force as weak distance-depending attractive force V_A , or more specifically the London dispersion force for intermolecular dipole-induced attractive forces, and secondly, the stabilization by electrostatic repulsion V_R of two equally charged particles. The total interaction force V of two equally sized spherically particles can be described with the DLVO theory as follows:

$$V = V_A + V_R = -\frac{A \times R_{sphere}}{12D} + 2\pi\epsilon R_{sphere}\xi^2 \times e^{-x_{DL}D} \quad (7) \text{ Derjaguin-Landau-Verwey-Overbeek theory for two equally sized spherical particles}$$

where the term $(-\frac{A \times R_{sphere}}{12D})$ is from the Hamaker theory with the Hamaker constant A , the radius of the two spheres R_{sphere} and the distance between the particles D . The second part of the DLVO theory $(2\pi\epsilon R_{sphere}\xi^2 \times e^{-x_{DL}D})$ includes the dielectric constant of the medium ϵ , the Zeta potential ξ and the Debye-Hückel parameter x_{DL} , which describes the ionic composition of the overall solution. By using the DLVO theory, some assumptions for enhanced colloidal stability can be made: First, the higher the concentration of particle-charge-enhancing ions, the more stable a colloid is. Second, ion solutions below the critical coagulation concentration enhance the colloidal stability by not destabilizing the boundary layer of ions which are responsible for the electrostatic repulsion (*Stern layer*). Third, the weaker the ions are charged ($\text{Na}^+ < \text{Mg}^{2+}$), the less they are destabilizing the *Stern layer*. As mentioned before colloidal solutions can be protected from aggregation by using polymeric molecules like Tween20 for steric stabilization. This stabilization effect is based on adsorption of the polymer on the surface of the AuNP by chemical or physical adsorption, building a *brush-like*, *mushroom-like*, or *pancake-like* structure depending on the grafting density of the polymer. [142] Responsible for the continuous separation of approximating sterically stabilized particles are two main effects: First, the increased osmotic pressure inside the interparticle gap of the two colliding particles by displaced solvent molecules. And second, the reduced conformational entropy of the polymer. Both

effects hinder the particles from reaching the distance at which the attractive force V_A leads to aggregation.

Obviously, the destabilizing effect upon Mg^{2+} addition is visible in **Figure 26** and the addition of ions with higher charge led to aggregation. In this experiment differently charged molecules were used for stabilization as well as the uncharged Tween20 as shown in **Figure 27**. The weakest stabilizing effect is visible with the CTAB (5 mM) stabilized particles, which even aggregate in 1x TE buffer without Mg^{2+} ions, whereas colloids stabilized by citrate (5 mM) and BSPP (10 mM), i.e., with 3 and 2 negative charges, respectively, resist up to 1 mM Mg^{2+} ions. Induced by the 1x TE buffer system set to pH 7.4 SDS, BSPP and citrate can be regarded as fully deprotonated. The stabilizing effect of SDS with only 1 negative charge per molecule can be attributed to the comparable high concentration (0.5 wt. % = ~ 17.3 mM). However, higher SDS concentrations cannot be used due to the disintegration of DNA origami above 1 wt. % of SDS. Following the DVLO theory it can be assumed that the twofold charged Mg^{2+} destabilize the surfactant layer and *Stern layer* on the AuNC surface. This countering of stabilizing charges together with upper limits for the surfactant concentrations makes them not suitable for conjugation experiments. In contrast, stabilized AuNC with the uncharged Tween20 (1 wt. %) resist at high ionic strength due to the stabilization mechanism based on the physisorption of uncharged polymers on the AuNC surface as described before.

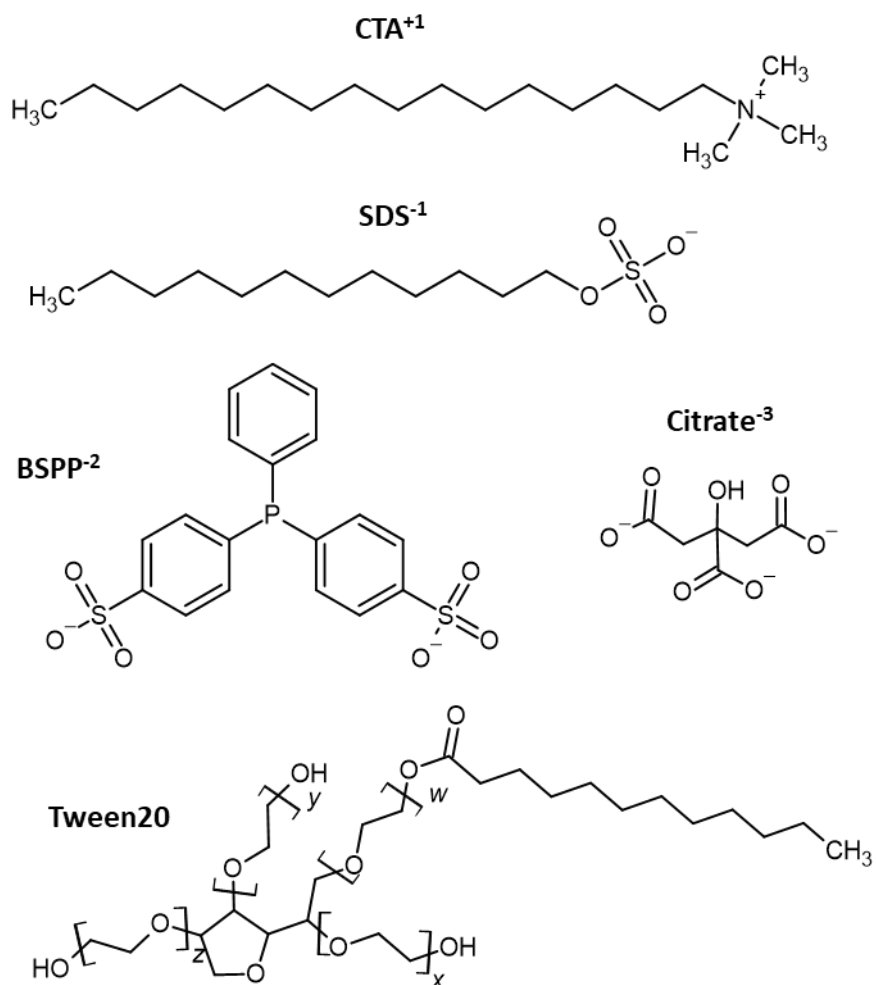


Figure 27: Molecular structure and charges of surfactants (CTAB, SDS, Tween20) and surface-active molecules (BSPP, citrate) used in the aggregation assay for studying their role in stabilization of AuNC.

4.4. Assembly of Pandora's Box

DNA origami structures are subject to a complex folding process, which requires a suitable assembly protocol. The assembly protocol consists of different parameters like the Mg^{2+} ion concentration, the speed of temperature decrease, the staple strand-to-scaffold ratio as well as the overall scaffold concentration. [17, 65, 143] The more complex an origami structure is, the more attention must be paid regarding the parameters used while the assembly. For instance, the thermal annealing ramp starts with the melting of all secondary structures, followed by carefully decreasing the temperature over a sufficiently long timespan to ensure correct folding. Especially between 50-60 °C, where most of the used staple strands are unfolded, the temperature decrease should be slowed down. Agarose gel electrophoresis (AGE), as described in chapter 3.7.3., is widely used for ensemble analysis of DNA origami and nanostructures in general. The analysis by AGE gives information about the structure as well as modification of origami structures by internalization of gold nanoparticles and their co-localization within the gel. Other techniques for direct analysis bear the potential risk of altering the overall properties of DNA origami regarding size or shape due to interaction with the surface (e.g., TEM grids) or the visualization in different phases (e.g., dried state).

Folding of compact and 3D DNA origami requires sufficient amounts of Mg^{2+} ions (> 12.5 mM) as stated in literature [144, 145], which is higher compared to the concentrations typically used for planar structures [17]. For the folding of the 3D DNA lidless origami box, in this thesis called Pandora's box, different Mg^{2+} concentrations were used ranging from 4 mM to 22 mM as shown in **Figure 28** (A). The EtBr-stained gel reveals a decreased electrophoretic mobility of the scaffold after addition of staple strands and at least 4 mM Mg^{2+} . Upon excision, TEM analysis of the four bands visible in the lane with the sample using 22 mM Mg^{2+} revealed that – in order of decreasing electrophoretic mobility – the bands correspond to mono-, di-, tri- and tetrameric forms of the desired box. It is noteworthy that the formation of correctly folded boxes starts at 10 mM Mg^{2+} and that these structures are correctly folded between 16-20 mM Mg^{2+} (B, right). Analysis and comparison of the EtBr fluorescence between the monomer and dimer intensity reveals an increased assembly yield with a maximum of 53 % correctly folded boxes at 20 mM Mg^{2+} and 10-fold staple excess. Dimerization of the boxes due to DNA helical stacking or unspecific scaffold overhang interactions is seen for all magnesium concentrations and can only be partially prevented by using thymine overhang staple strands at the edges of the box. In contrast, higher magnesium concentrations lead to ion-induced aggregation by screening of the negatively charged DNA phosphate backbone. However, the overall assembly yield of the desired structure is quite low compared to the material needed for the conjugation experiment and needs to be enhanced.

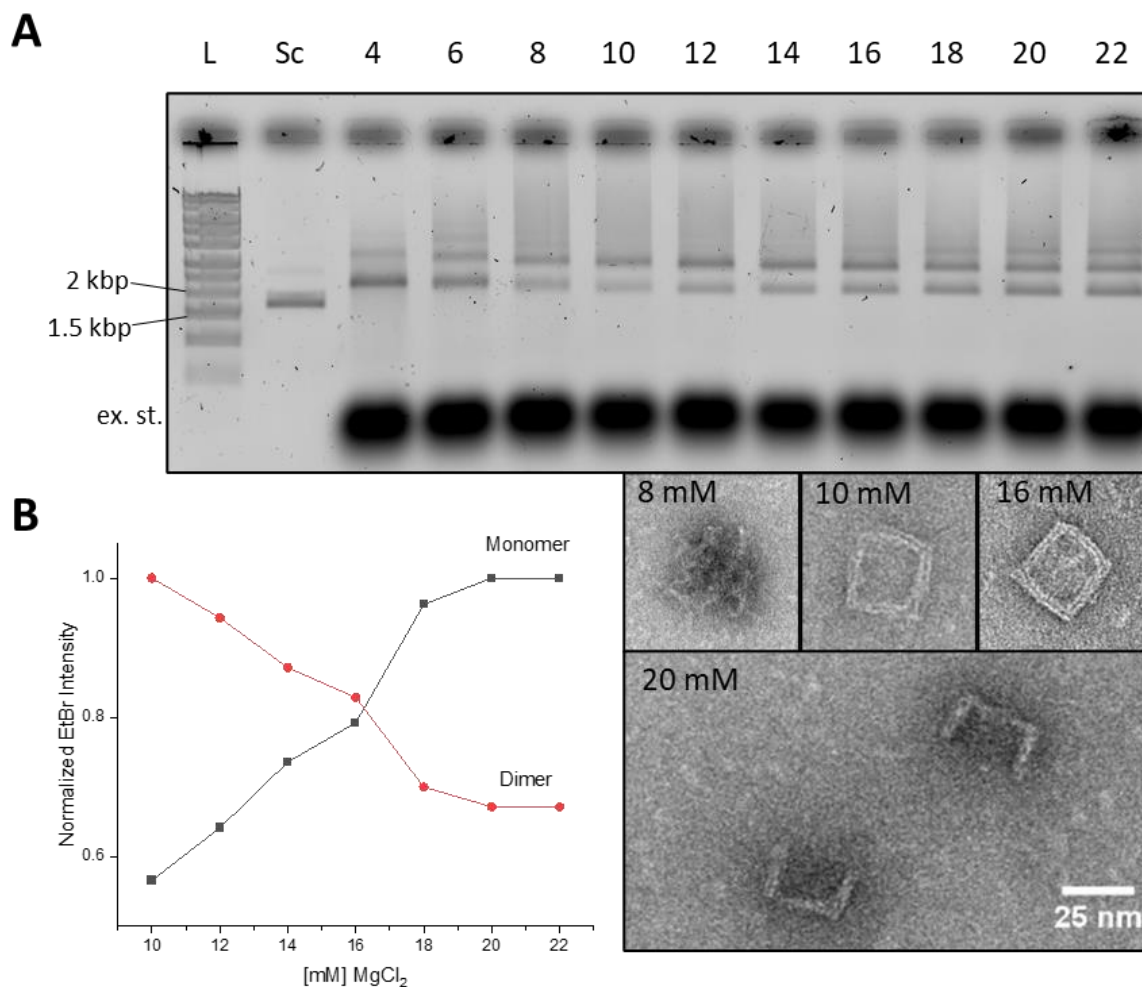


Figure 28: Magnesium-screening of Pandora’s box assembly. (A) L denotes 1 kbp ladder, Sc denotes the phage genome scaffold, 4-22 denotes the MgCl₂ concentration in mM used during assembly. The location of excess staple strands in the gel is indicated by ex. st.. TEM images display the assembly result with different MgCl₂ concentrations. (B) Normalized EtBr fluorescence intensity of the monomer and dimer bands reflecting the assembly yield.

It is well known that the excess of staple strands has a big impact on the assembly yield of the DNA origami, too, and has to be carefully evaluated beside the Mg²⁺ concentration. [143] Cooperative hybridization of several hundred staple strands and staple-scaffold inter-base-stacking are the driving force of origami folding. In addition, kinetic traps in the energy landscape of DNA origami folding can decrease the assembly yield and should be considered when designing a DNA origami. [65, 146] Applying published assembly conditions and empirical design rules it is possible to enhance the assembly yield. [62] Negative stain TEM imaging of the assembled boxes allowed to determine the dimensions of Pandora’s box, which has an inner width of 25.4 ± 1.8 nm, a height of 26.1 ± 2.5 nm and a core diameter of 34.5 ± 2.9 nm, as indicated in **Figure 29**. These values are in good agreement with the calculated dimensions based on the base length and the helical diameter which are 21.3 nm for

the inner width, 25.4 nm for the height and 31.7 nm for the core diameter. Of course, TEM prevents the visualization of the original in suspension state and only reveals the size of objects in the dry state after interaction with the grid surface as well as the interaction with heavy metal ions. Thus, dimensions can vary compared with the calculated values and for a more accurate determination of the native state, cryo-TEM or liquid AFM analysis should be performed. The dimensions of the box pose an upper limit to the size of the gold nanoparticle which can be incorporated. Their size should not exceed 20 nm with respect to the protruding staples located inside the box.

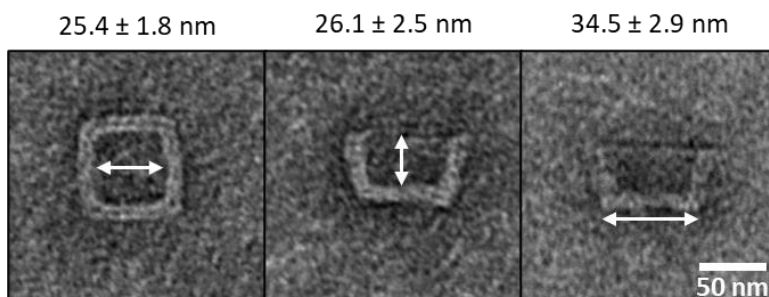


Figure 29: TEM images of negatively stained Pandora's boxes for determination of the inner diameter (left), height (middle) and bottom plate (right). For statistical analysis, $n=40$ boxes were measured.

The assembly yield of Pandora's box was increased to 53 % by adjusting the cation concentration to 20 mM as shown before. **Figure 30** (A) shows the AGE analysis of staple screening in which the excess of staples in relation to the scaffold was varied from 2.5x to 25x keeping the scaffold concentration at 5 nM using 20 mM Mg^{2+} ions concentration. The EtBr-stained gel image reveals an unchanged electrophoretic mobility of the dimer and monomer band as expected, with both bands showing a lower migration rate when compared to the scaffold itself. Enlarging the staple excess to 25x leads to smear above the dimer band as well as aggregates inside the gel pocket, indicating a partial aggregation of the boxes. Analyzing the EtBr fluorescence intensity (B), an increased assembly yield of the monomeric form from 38 % to 88 % while reducing the staple excess from 25x to 2.5x is visible. Conversely, increasing the staple excess from 2.5x to 25x leads to increased yield of the dimeric form from 12 % to 62 %. This correlation of assembly yield and staple-to-scaffold ratio and the underlying thermodynamic mechanism was described recently in the literature. [143] Briefly, this effect can be explained considering that two identical staples bind separately to the two corresponding binding domains of the scaffold, whereby neither of them is removed by staple displacement. This leads to a sort of "blocked state" that is favored if high staple concentrations are used, resulting in a supersaturated hybridization state. However, by reducing the staple excess to 2.5x and setting the Mg^{2+} concentration to 20 mM, the assembly yield can be enlarged to 88 % for the monomeric correctly folded form of Pandora's box. This is sufficient for further preparative purification by AGE and

incorporation of gold nanoparticles. It has to be mentioned here that the overall molar yield of boxes after AGE purification and isolation from the gel by spin-column extraction is ~10 % and should be enhanced in the future. A method of choice could be the asymmetric-flow field-flow fractionation (A4F), whose mechanism of separation is based on the diffusion of the analyte inside a laminar flow with a parabolic flow profile above a membrane. [147-150] The use of an orthogonal crossflow enables the separation of macromolecules, nanoparticles, and polymers from single to several hundred nanometers in size. While separation, the analytes are in stable colloidal suspension and do not interact with the membrane, which ensures their structural integrity. Additionally, online analysis with DLS and UV-Vis extinction spectroscopy as well as controlled elution of the desired particle fraction makes A4F a powerful tool for gold nanoparticle as well as DNA origami purification and can dramatically enhance the yield of purified DNA origami if preparative scales are necessary. First proof-of-principle A4F-based separation experiments with origami filaments were performed in cooperation with Lena Stenke and should be continued in future work.

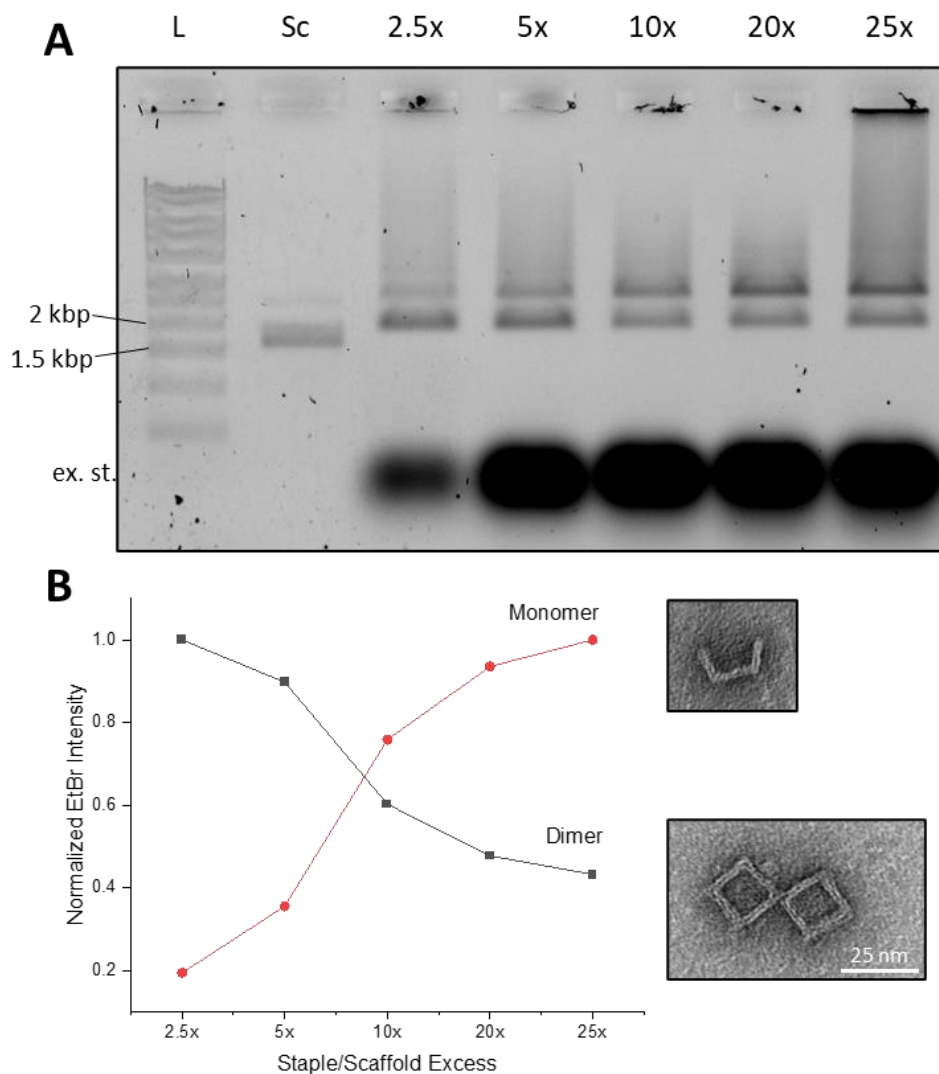


Figure 30: Staple-screening of Pandora's box assembly. (A) AGE analysis of assembly with 5 nM scaffold, 20 mM MgCl₂ and varied staple/scaffold excess. L denotes 1 kbp ladder, Sc denotes the phage genome scaffold, 2.5x – 25x denotes the staple excess used during assembly compared to the scaffold amount. The location of excess staple strands in the gel is indicated by ex. st.. (B) Normalized EtBr fluorescence intensity of the monomer and dimer bands representing the assembly yield with representative TEM image of Pandora monomer and dimer.

4.5. Incorporation of Gold Nanoparticles and Gold Nanocubes with Different Sizes in Pandora's Box

In literature, the widely used base hybridization approach is mostly utilized to combine oligonucleotide-functionalized gold nanoparticles with various shapes and sizes with DNA origami as described in section 2.3. Plasmonic hybrid structures assembled this way are designed for different applications, ranging from plasmon sensing to cancer therapy. [151-153] While this approach may be sufficient for many applications, it bears some drawbacks: the hot spot is filled with DNA and the gold surface is not accessible for further ligands or molecules for catalytic reactions. To overcome this problem, the thiols can be placed directly onto the DNA origami surface by using protruding staples and thiolated anti-handles. [87, 127] The following chapter presents first the incorporation of gold nanoparticles into Pandora's box by the base hybridization approach using ssDNA-functionalized gold nanoparticles and complementary protruding staples inside Pandora's box. The second part describes the new developed incorporation approach using surfactant-stabilized gold nanoparticles and thiols presented inside the box. Afterwards, the incorporation yield of both methods with respect to the gold nanoparticle size and geometry is discussed.

4.5.1. Incorporation via Hybridization

To compare the incorporation yield of the hybridization method with the thiol-based method, 10 nm AuNP were functionalized with thiolated handles complementary to anti-handles located as *protruding arms* inside Pandora's box (**Figure 31**, A). To evaluate the binding efficiency and identify unspecific binding, the number of protruding staples was varied between 0 and 28, as indicated in bold numbers (**Figure 31**, B). Statistical analysis of TEM images reveals only a small percentage (1 %) of unspecifically incorporated ssDNA-functionalized AuNP due to their electrostatic repulsion from the origami. The yield can be gradually increased to 62 % by introducing protruding staples inside the box; the strongest increase of binding efficiency is achieved with 28 protrusions. Of course, besides the number of protrusions, their localization inside the box is tremendously important. For instance, the box with 16 protruding staples exhibits no protrusions on the core plate compared to the structure with 28 protrusions. This underlines the importance of protruding staples located on the core plate, pointing towards the open side of the box. Steric hindrance is probably responsible for the less effective hybridization with protrusions located on the inner site walls. However, beside the overall and presumably electrostatically limited incorporation yield, size limitations must be considered, too. For example, it was not possible to incorporate gold nanoparticles with a diameter ≥ 13 nm. Thus, a size of 13 nm can be considered as an upper limit for incorporation by hybridization (**Figure S 5**). [87] Hybridized protruding staples located on the inner walls with 16 bp have a length of ~ 5.4 nm on each

side which minimizes the size of an incorporable gold nanoparticle to ~11 nm. With respect to the origami design, the persistence length of dsDNA which describes the mechanical stiffness as well as the base length of dsDNA, it is obvious that a calculated inner box diameter of ~22 nm is too small. On the other hand, DNA origami structures bear, in spite of the dsDNA persistence length, a certain degree of flexibility which should enable the incorporation of bigger particles as reported for instance by Zhao *et al.* in 2011 [154] and Luo *et al.* in 2018 [155]. In their work, particles larger than the cavity of the DNA origami cage were incorporated by hybridization reaction by either bending the origami apart or not full incorporation of the particles. For instance, the size of the inner cavity used by Luo *et al.* was designed to be 10 nm x 10 x nm x 21 nm. Incorporation yields between ~36 % and ~99 % were achieved with respect to the gold nanoparticle size between 5 nm and 15 nm and the number of catching strands (1-3) inside the DNA origami cage. Taking this into account, even higher incorporation yields should be achievable in our hybridization experiments. The stability of the ssDNA-functionalized AuNP used in our experiments is comparable to values published in literature [156, 157], which suggests similar ssDNA loading. Interference of Tween20 to base hybridization reactions was not found to play a role until the highest tested concentration of 1 wt. % (**Figure S 6**). However, it is possible that Tween20 molecules, which are still present on the AuNC surface, sterically hinder the incorporation by base hybridization.

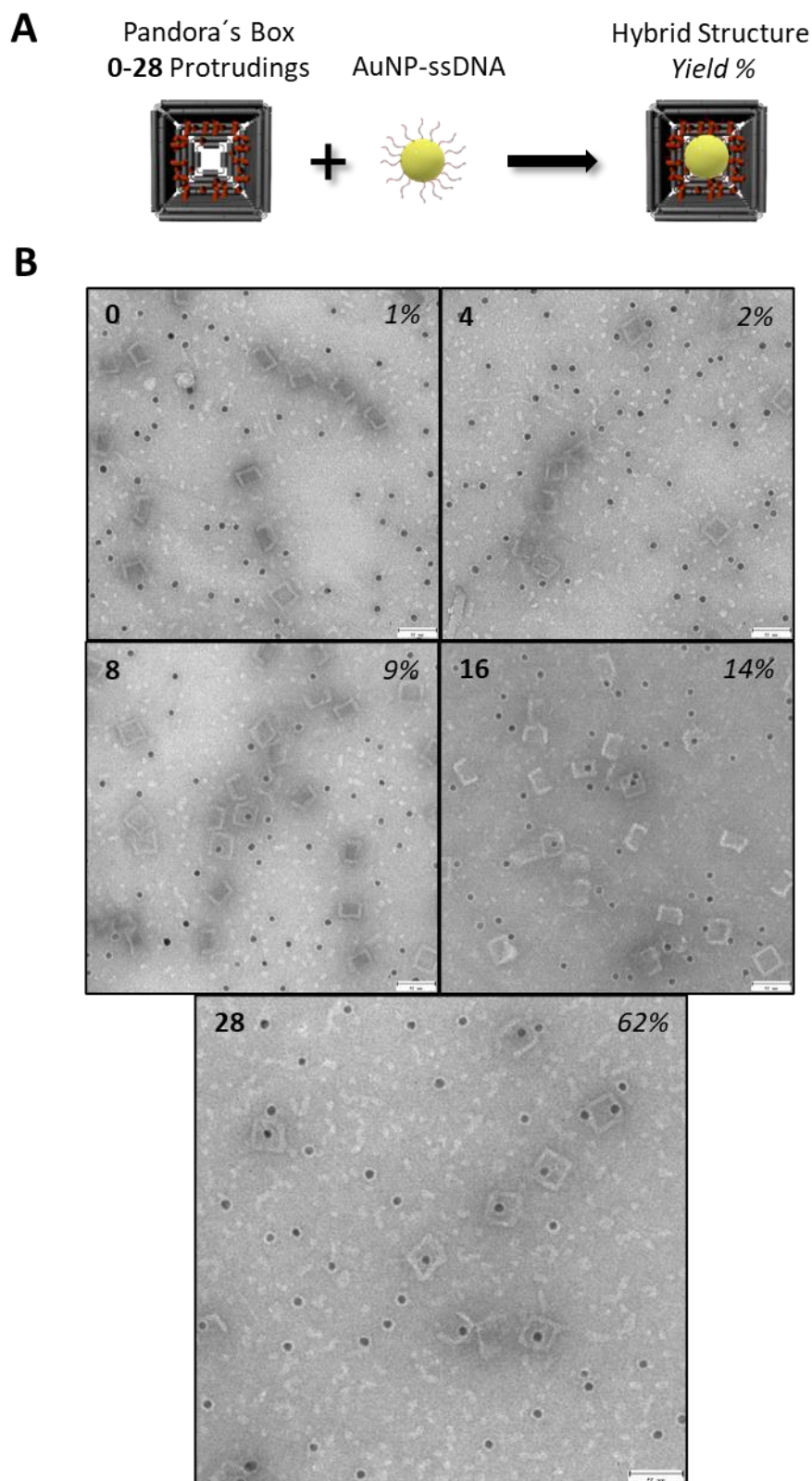


Figure 31: Incorporation of 10 nm AuNP into Pandora's box by base hybridization. (A) Prior to the incorporation, the AuNP were functionalized with thiolated oligonucleotides complementary to protrudings inside the box. (B) Representative TEM images of unpurified samples after hybridization at 2.5x molar excess of AuNP with Pandora's box for 24 h at 30 °C. Bold numbers indicate the number of protrudings and italic numbers indicate the resulting incorporation yield. For statistical analysis at least $n = 129$ boxes were counted. Scale bars = 50 nm.

4.5.2. Incorporation via Thiol Chemistry

After successful incorporation of ssDNA-functionalized AuNP inside Pandora's box, incorporation of differently shaped and sized gold nanoparticles via thiols was performed. The corresponding results are shown in **Figure 32** and the incorporation yields are listed in Table 3. The concept of incorporation is based on the decoration of the inner walls and the inner core with thiolated anti-handles (blue) which are complementary in sequence to the staples (red) protruding out of the origami surface, as schematically shown in **Figure 32** (A). Consequently, different numbers of thiols can be placed inside the cavity. The maximum number of 28 thiols placeable inside the cavity was used as well as a reduced number (16 and 0 thiols) to show the correlation between the binding yield and the number of thiols. AuNP with 8, 10 or 15 nm, respectively, and AuNC with an edge length of 16 nm or 18 nm, respectively, were used for conjugation as shown in **Figure 32** (B). An origami without thiols served as a negative control for determination of unspecific binding which was not visible at all (**Figure S 7**). As expected, the incorporation yields gradually decreases with increasing AuNP and AuNC size and increases with higher number of thiols inside (**Figure S 7**). The highest incorporation yield was achieved with 28 thiols and 8 nm AuNP with 77 % of boxes containing at least one single AuNP. Compared with 16 thiols, the yield is decreased to 68 %. The lowest incorporation yield is obtained with 18 nm AuNC with 16 % (28 thiols) and 3 % (16 thiols), respectively.

However, compared to the incorporation yield of AuNP by using base hybridization (4.5.1), the thiol-based approach led to higher incorporation yields. For instance, ssDNA-covered 10 nm AuNP were internalized with a 62 % yield inside boxes presenting 28 protruding arms, whereas 69 % bare AuNP were internalized using 28 thiols presented inside the box. With respect to the stability of ssDNA-functionalized gold nanoparticles, the incorporation yield may be enhanced by increasing the AuNP concentration and thus the stoichiometry while the coupling reaction. However, this is not recommended for this thiol-based incorporation which is based on the metastable state of the Tween20-stabilized gold nanoparticles. For AuNP concentrations higher than ~ 125 nM in $0.5\times$ TE[Mg²⁺] [6.25 mM], the AuNP aggregate during the conjugation reaction, leading to a dramatically decreased yield. On the other hand, when taking the size and electrostatic limitations into account which hinder the incorporation of AuNP and AuNC with a size $>\sim 12$ nm, the thiol-based approach enables the incorporation of AuNP/AuNC up to 18 nm. This size is sufficiently large for plasmonic applications and enables further experiments.

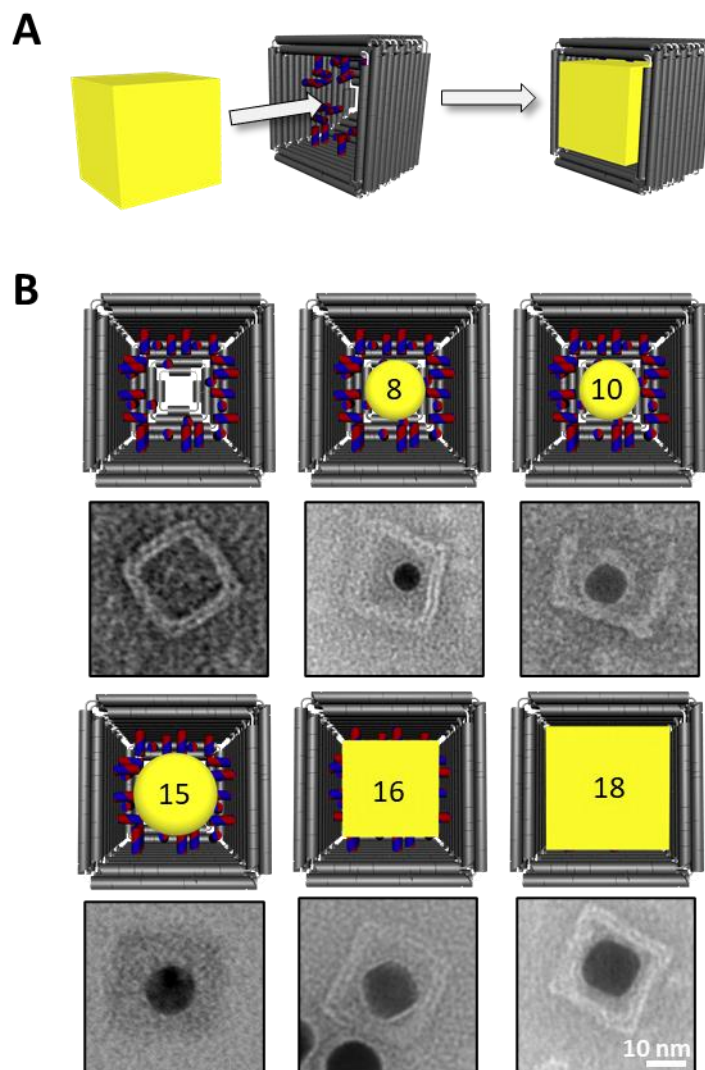


Figure 32: Internalization of gold nanoparticles with different sizes and shapes into Pandora's box. (A) Scheme for incorporating 18 nm AuNC into Pandora's box bearing thiols inside the cavity. (B) TEM images of Pandora's boxes containing differently sized and shaped gold nanoparticles ranging from 8 nm AuNP to 18 nm AuNC.

Table 3: Incorporation yields of differently sized and shaped gold nanoparticles into Pandora's box via thiol chemistry. Different numbers of thiolated oligonucleotides present inside the box were used. For stabilization of <15 nm gold nanoparticles 0.15% Tween20 and for >15 nm gold nanoparticles 0.2% Tween20 was used while incorporation. For statistical analysis at least $n = 130$ origami boxes were counted.

No. thiols	AuNP			AuNC	
	8 nm	10 nm	15 nm	16 nm	18 nm
0	0%	0%	0%	0%	0%
16	68%	59%	12%	13%	3%
28	77%	69%	50%	28%	16%

4.6. Purification of Gold Nanoparticle-Origami Conjugates

High incorporation yields of gold nanoparticles inside DNA origami require a high molar excess of gold nanoparticles which must be removed prior to spectroscopic applications since unbound NP may lead to unspecific signal or interaction with the analytes. Several mechanisms for purification of DNA origami have been reported: they range from the PEG-induced precipitation that relies on the crowding effect [158], to ultra- or gel-filtration, AGE separation followed by gel extraction, magnetic bead-based separation or FPLC. [159, 160] As mentioned before, alternative techniques like A4F can be also used for purification of origami structures. Here, the gold nanoparticle-origami conjugates were purified using the AGE method for both analytical as well as preparative purposes. The purification of DNA origami structures on a preparative scale and likewise the purification of gold nanoparticle-origami conjugates requires high sample concentrations obtained by enrichment. Typically, cut-off filtration devices are employed for this purpose: the filter membranes are permeable to water and small molecules whereas they retain larger molecules above the cut-off limit. **Figure 33** shows a Pandora's box sample (left) after conjugation to gold nanoparticles (13x molar excess) with an incorporation yield of 53%. After sample concentration (10x-fold) using cut-off filtration devices, the stability of the origami is still maintained and the sample can be mixed with loading dye and purified by AGE. Notably, the incorporation yield is similar after centrifugation.

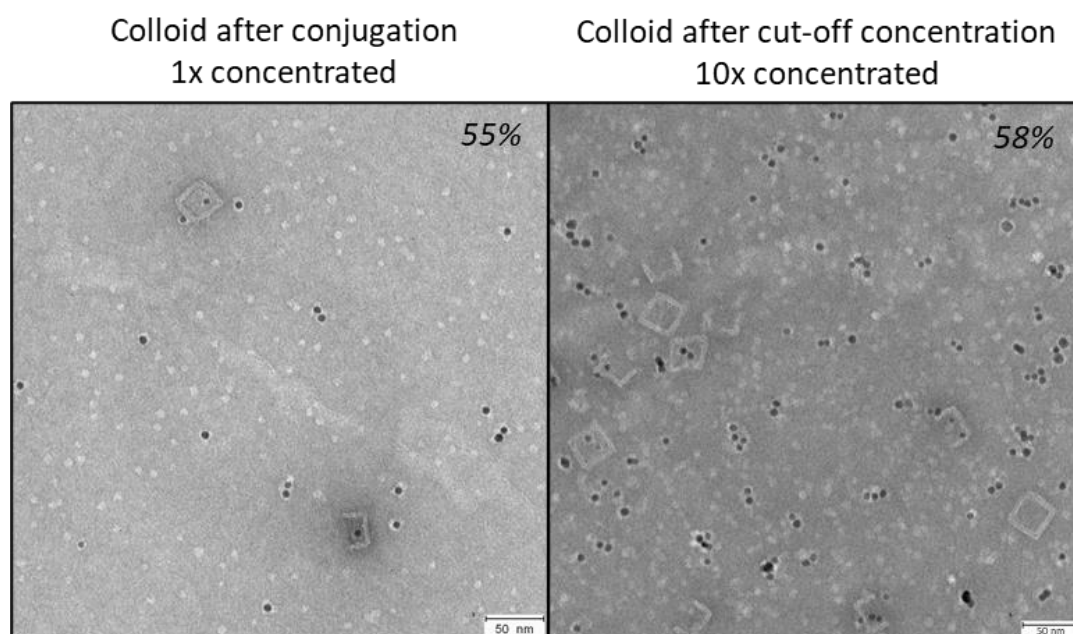


Figure 33: TEM images of unpurified colloids after conjugation containing Pandora's boxes as well as AuNP (left). Same colloid after cut-off concentration (right, 100 kDa filter, 7 min, 2.000 rcf). Italic numbers indicate the resulting AuNP incorporation yield. For statistical analysis at least $n = 157$ boxes were counted. Scale bars = 50 nm.

Figure 34 (left) shows a typical EtBr-based AGE analysis for preparative purposes: the 10x-lane is used for excision of the desired product band followed by spin column extraction and TEM imaging. The gel is loaded with empty boxes and AuNP, both as negative controls, as well as the 1-fold concentrated colloid after AuNP-origami conjugation and the 10-fold concentrated sample. The gel shows that AuNP as well as the origami boxes are stable in our conditions as no aggregates are visible inside the pockets. The control sample of Pandora's box shows a monomer and a dimer band; the latter is likely due to undesired stacking of the origami structures at the high concentrations used for sample preparation. It has to be noted here that a dimerization band is visible upon storage of the concentrated Pandora samples for several weeks at room temperature. The AuNP stabilized with Tween20 show a higher electrophoretic mobility visible as a whitish band inside the bromophenol blue band. The whitish color of the AuNP band upon EtBr-staining is originated by the fact that plasmon peaks at ~520 nm lead to an absorption and thus to a white appearance in fluorescence images of EtBr-stained gels. Despite the stabilization of AuNP by addition of Tween20 inside the gel and running buffer, a whitish smear can be seen above the AuNP band. This indicates a metastable state of AuNP inside the suspension which is also critical in the mixture after conjugation. Nevertheless, the electrophoretic mobility of Pandora's box does not change after AuNP incorporation as demonstrated from TEM imaging of the excised monomer band (**Figure 34**, right). In fact, 61 % (n = 149) of the monomers contain a single AuNP after purification which is slightly higher than (**Figure 33**, 58 %). More importantly, only 12 % of unbound AuNP (n = 20) are visible in TEM images with respect to the total number of counted AuNP (n = 169). This rate of removal from initially 13-fold molar AuNP excess prior to conjugation to only 12 % of unbound AuNP after purification is equivalent to the removal of 99 % of unbound AuNP.

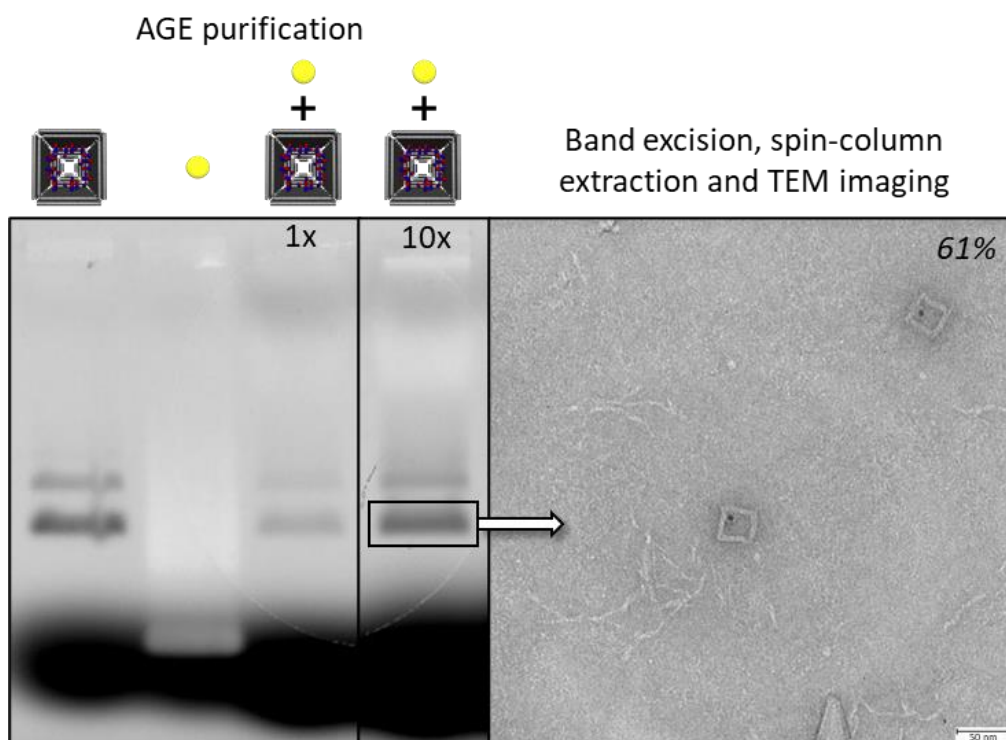


Figure 34: AGE purification and TEM imaging of nanoparticle-origami conjugates. (left) AGE purification of a mixture containing AuNP and DNA origami boxes for isolation of box-AuNP conjugates. Isolation of conjugates from gel by spin-column extraction (7 min, 250 rcf) followed by TEM imaging. (right) TEM images of isolated box-AuNP conjugates. Italic numbers indicate the resulting incorporation yield. For statistical analysis at least $n = 244$ boxes were counted. Scale bars = 50 nm.

4.7. Zelos Assembly and Characterization

Dimerization of gold nanoparticles incorporated into Pandora's box requires the design, assembly and characterization of a DNA origami platform with intrinsic dynamic properties. As describes in section 3.4.2, the platform, called Zelos in this thesis, consists of a bilayer of two origami rectangles connected by four duplexes on each side of the gap. The bundles can be used for controlling the distance between the two rectangles by using toehold-mediated single-strand displacement reactions. This leads to formation of scaffold loops while pulling the platform halves together. Assembly of the newly designed Zelos origami was done using the same thermal annealing protocol used for the assembly of the Pandora box and the effect of different Mg^{2+} concentrations was evaluated using AGE and TEM as shown in **Figure 35**. The results show that different bands appear depending on the cation concentration. Using 4 mM and 8 mM Mg^{2+} leads to the formation of more compact structures with decreased electrophoretic mobility compared to the scaffold control (A). Additionally, mono-, di- and trimers of Zelos are formed; they exhibit a decreasing electrophoretic mobility with increasing the size. TEM analysis of these structures reveals the incomplete formation of the two rectangular bilayers of Zelos. First assembly of Zelos was observed at 8 mM Mg^{2+} and the highest assembly yield was achieved using 16 mM Mg^{2+} . At higher Mg^{2+} concentrations the appearance of additional bands in the gel suggests that unspecific interactions of origami take place and that multimers may form. The scaffold can be considered as flexible polymeric molecule which can be described by the worm-like chain model. Thus, a long flexible chain can be assumed as a random coil structure with partially stacked domains. [161] Incorrectly folded Zelos (**Figure 35, B, left**) exhibits a more compact scaffold-like structure than correctly folded Zelos which would result in a higher electrophoretic mobility. Band mobility reveals instead an opposite trend. The correctly folded Zelos monomers show an electrophoretic mobility similar to that of the scaffold whereas low concentrations of Mg^{2+} (6 – 10 mM) enlarge the compactness. It has to be mentioned here, that the structure of Zelos visible in TEM (**Figure 35, B, right**) at 16 mM Mg^{2+} shows a potential weakness at the eight helices responsible for the separation of the two rectangular halves. After optimization of Mg^{2+} concentration and staple screening it was found that 16 mM Mg^{2+} and 10-fold staple-to-scaffold excess are ideal assembly conditions. Assembly yields calculated by the intensity of the gel bands indicate that monomers form with a 64 % efficiency.

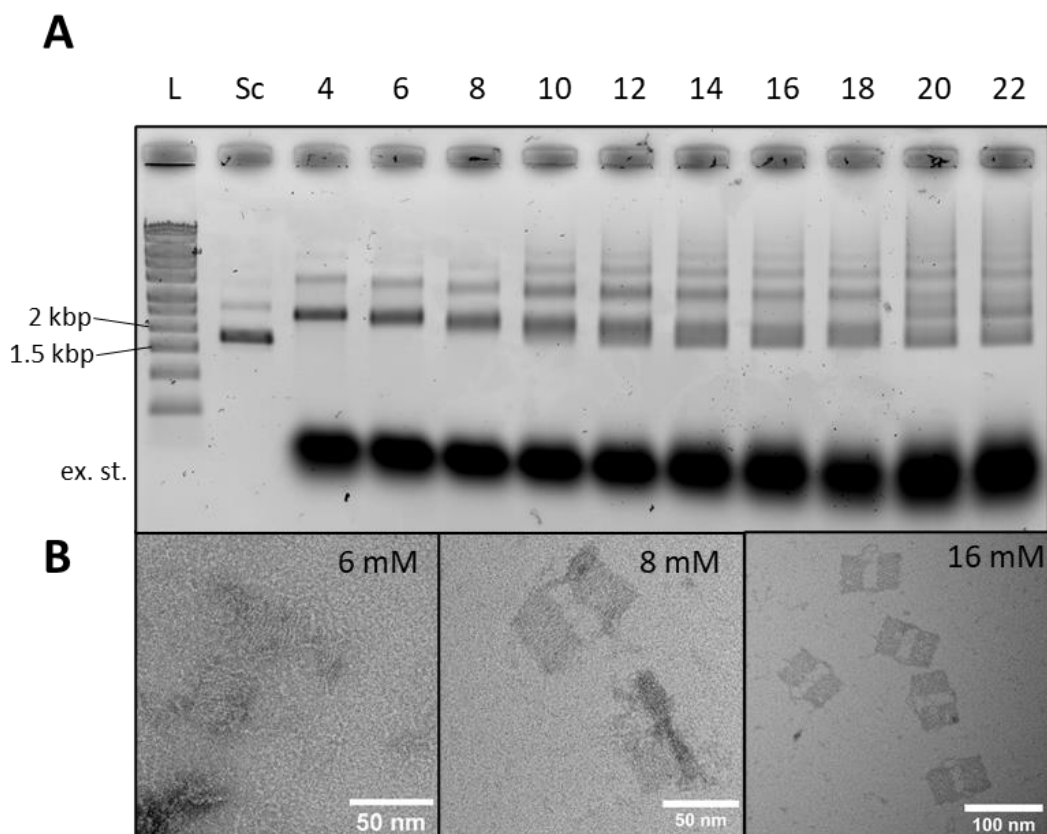


Figure 35: Magnesium screening of Zelos assembly with 43 bp gap distance. L denotes 1 kbp ladder, Sc denotes the phage genome scaffold, 4-22 denotes the MgCl_2 concentration used during assembly in mM. The location of excess staple strands in the gel is indicated by ex. st.. (B) TEM images show the assembly result obtained with different MgCl_2 concentrations.

Imaging via TEM was used to estimate the overall size of Zelos after successful assembly of Zelos. Zelos with 0 bp distance (right) has a mean length of 60.7 ± 3.5 nm and a width of 45.9 ± 5.7 nm as shown in **Figure 36**. In contrast, Zelos with 43 bp distance has a length of 74.8 ± 3.4 nm and a width of 50.4 ± 2.0 nm (left). The calculated length of the 0 bp state is 58.1 nm while the calculated length of the 43 bp state is 72.8 nm; both match well with the experimentally measured values. On the contrary, the measured widths of the 0 bp and 43 bp state deviate from the calculated values. This difference can be explained as the result of intrinsic tension and deformation of the structures in the conditions used for TEM imaging. It has to be considered that the overhang staples inside the gap, while preventing stacking effects, can also induce a bending effect in the 0 bp state as exemplary shown in **Figure 36** (right). However, the overall structural integrity is still ensured.

Length:	74.8 ± 3.4 nm	60.7 ± 3.5 nm
Diameter:	50.4 ± 2.0 nm	45.9 ± 5.7 nm

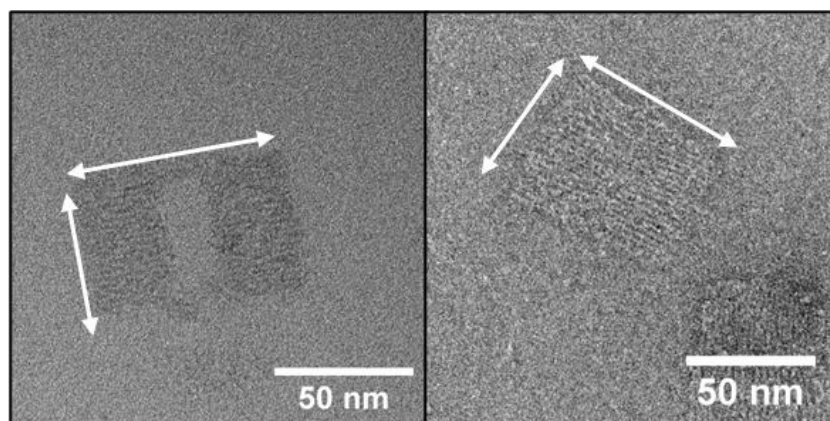


Figure 36: Characterization of Zelos dimensions (43 bp and 0 bp distance). Representative TEM images of AGE-purified Zelos platform with 43 bp (left) as well 0 bp gap distance (right). For statistical analysis $n = 68$ boxes were measured.

4.7.1. Characterization of the Dynamics

Zelos was designed to achieve base pair-wise stepping of the gap size by using oligonucleotides of different lengths. In this thesis, five different lengths were used, resulting into duplexes which are 0, 6, 12, 24 or 43 bp long. A first evaluation of the device performance was carried out by adding a defined set of gap-staples in the assembly mixture. The resulting Zelos origami were analyzed quantitatively at the ensemble level via fluorescence in AGE (A) and qualitatively at the single-Zelos level via TEM imaging (B) (**Figure 37**). AGE analysis shows a slight increase in the electrophoretic mobility of Zelos with increasing gap distance. Overall, the mobility of Zelos within the gel is lower when compared to the scaffold. Interestingly, by increasing the gap distance, the monomer bands become broader. Bending of the connecting helices might be responsible for this behavior and make predictions on its electrophoretic mobility difficult. The statistical analysis of Zelos in TEM nicely reveals that the measured distance is close to the calculated value. In detail, using the 0 bp fuel strands during the assembly process leads to Zelos structures with no visible gap in between the two halves. In contrast, using the 6 bp fuel strands results in the formation of a 2.8 ± 1 nm gap. The expected gap distance for this set of fuels is 2.04 nm. The small difference from the measured value can be caused by the limited number ($n = 21$) of measured structures and the difficulty in resolving the fine structure of planar origami by TEM. Altogether, a larger gap led to better staining results and a higher number of measured structures. Using 12 bp oligos results in a 4.2 ± 0.9 nm gap distance which is in good agreement to the calculated distance of 4.08 nm. Using 24 bp and 43 bp oligonucleotides led to 8.1 ± 1.3 nm and 14.5 ± 1.3 nm gap distances, which also nicely match with the calculated values of 8.16 nm and 14.62 nm,

respectively. Even though the mean values of the measured distances are close to the calculated, the standard deviation is constant by ~ 1 nm. A possible reason for that can be the grain sized of the used uranyl formate which is around 0.4 – 0.5 nm [162] and the dried state of the structures during TEM imaging. Moreover, the single unpaired scaffold base at the end of each duplex of the gap also introduces a flexibility of around ~ 0.56 nm, which can contribute to the observed standard deviation. It should be noted here that the persistence length of dsDNA and ssDNA is different with ~ 50 nm for the former and $\sim 1.98 - 2.2$ nm for the latter [163, 164]; however, the published values of ssDNA persistence length are still under debate. In addition, the orientation of the gap staples is such that the unpaired scaffold base is placed alternatively on the left and right half of the platform. In this way, no clear “break point” is generated and the stability along the whole origami is optimized as shown in **Figure 17**.

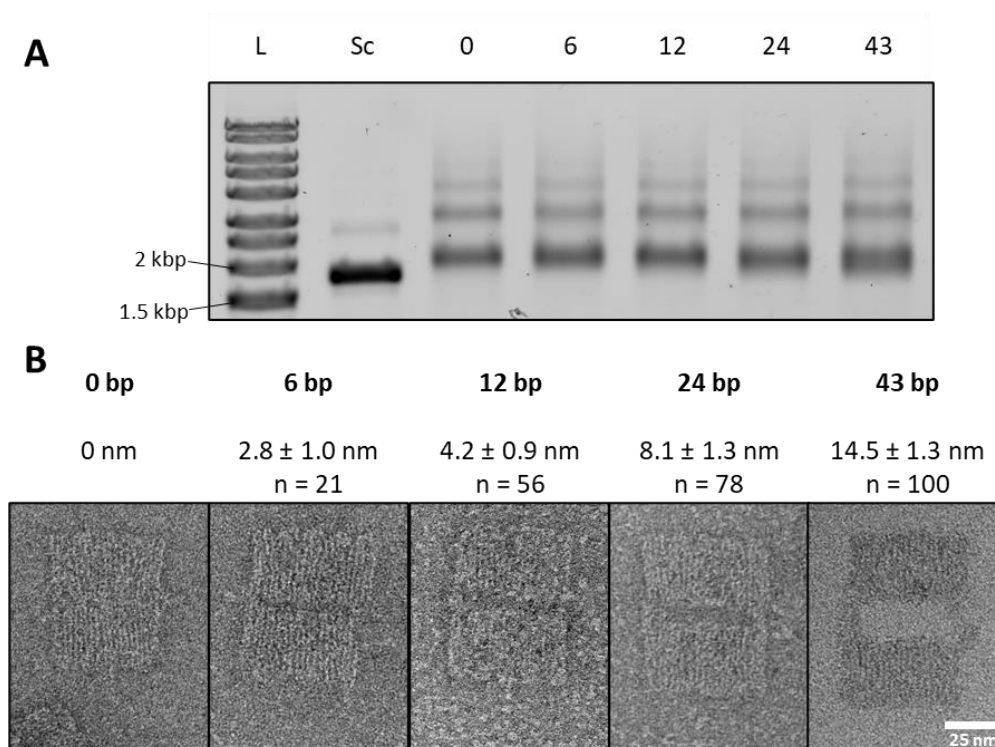


Figure 37: Characterization of Zelos’ dynamic properties. (A) AGE of Zelos with different gap distances ranging from 0 bp to 43 bp. L denotes 1 kbp ladder, Sc denotes the phage genome scaffold, 0-43 denotes the duplex length of Zelos’ loop-region. (B) TEM images of Zelos assembled with different gap distances. For determination of the gap distances and statistical analysis between $n = 21$ and $n = 100$ structures were measured as indicated.

The efficient actuation of the device from one state to the next was evaluated using single-particle TEM studies and statistical analysis in the dried state. Of course, more insights in the dynamic behavior of the device in aqueous solution can be acquired at the ensemble level by optical spectroscopic methods such as FRET. For this purpose, fluorescent labelling of the inner edges of Zelos with FAM and

TAMRA was carried out to enable the indirect read-out of the distance between these two fluorophores using AGE and *in situ* analysis of the fluorescence FAM signal. The exact position of the FRET pair as well as the changed length of the edge staples, omitting the polyT sequence to avoid steric hindrance of the fluorophores, around the FRET pair is shown in **Figure S 10**. **Figure 38** (A) shows the AGE analysis of Zelos assembled with different gap distances and a scaffold control. The gel was imaged using the FAM and TAMRA channels. If FAM is excited, it can transfer the energy to the TAMRA fluorophore through non-radiative dipole-dipole coupling, which is typically accompanied by a slight enhancement of the TAMRA signal. In **Figure 38** (A) both channels were separately imaged, thus, revealing a quenched donor (FAM) signal at smaller distances. Gel analysis reveals a gradually decreasing FAM signal upon approaching of the two inner edges of Zelos while the TAMRA signal intensity remains practically unchanged. The lowest FAM intensity is visible at 0 bp and shows the successful implementation of the fluorophores as well as the successful approaching of the two halves of the device. *In situ* FRET analysis (**Figure 38**, B) validates the AGE results. The relative FAM intensity is decreased if the distance between the two labelled inner Zelos edges is decreased. Noteworthy is the slightly increasing FAM signal at 0 bp distance. As mentioned before, the 0 bp state of Zelos shows the strongest size deviation in statistical analysis of TEM images, supporting the hypothesis of mechanical tension caused by the sterically demanding overhang staples at the inner edges. Accordingly, the increased FAM signal at 0 bp can be owed to the bending of the inner edges, including the FRET pair, away from the horizontal plane of Zelos either up or down. Finally, this would result in larger distances between the FRET pair and higher FAM intensities. However, the overhang staples at the inner edges cannot be completely omitted due to helical stacking effects as experimentally shown in **Figure S 9**. With respect to the length of the overhang staples (5 thymine) and their unpaired state which induces flexibility, the possible bending effects should be negligible with respect to the structural integrity of Zelos. However, the FRET intensity depending on the distance between the FRET pair is sensitive to even small changes. Thus, TEM analysis gives more reliable information about the geometry of Zelos at < 1 nm distances. FRET is an important technique for the live readout of the dynamic gap distance change whereas TEM is used for the endpoint analysis of the changed gap distance.

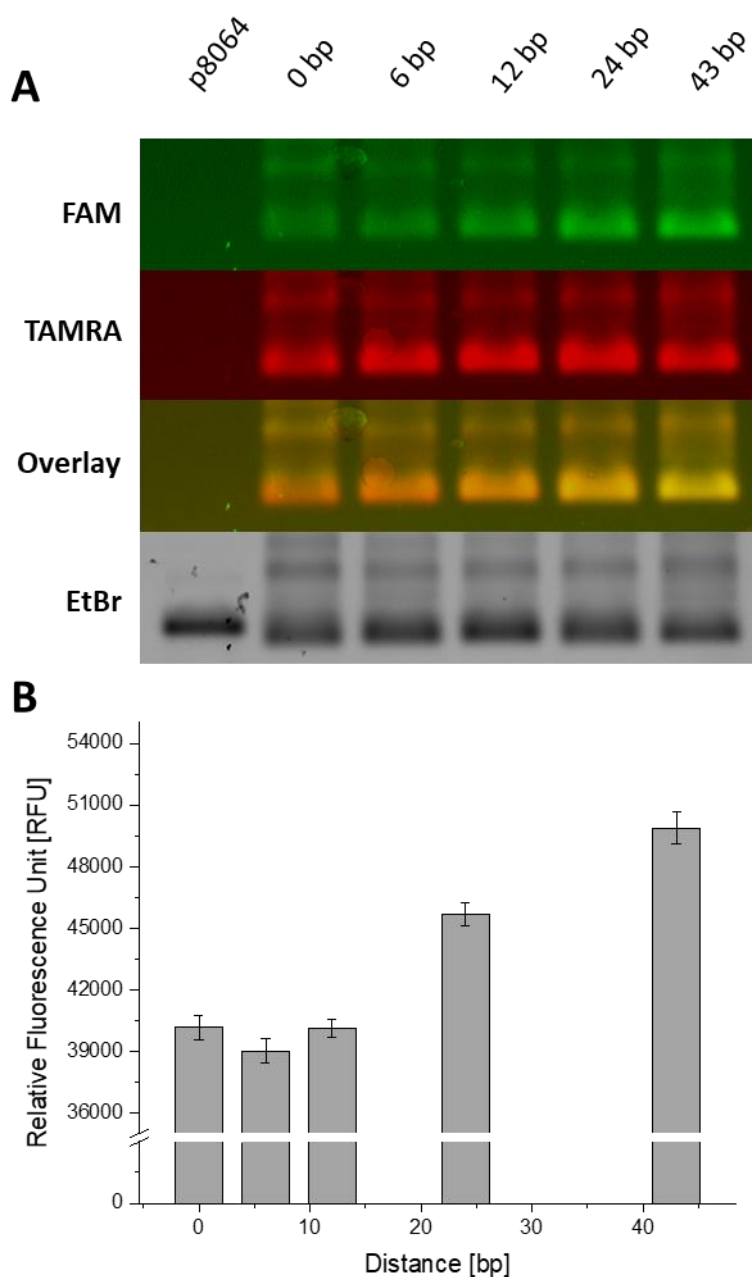


Figure 38: FRET-based determination of the variation in Zelos' gap size. (A) AGE analysis of Zelos labelled with FAM and TAMRA on each side, respectively. Lower gap distances lead to increased FRET extinction of the FAM fluorescence. Fluorophore channels were imaged separately followed by EtBr staining and imaging. 5 μ L Zelos with 20 nM without purification after assembly were loaded as well as 100 ng scaffold. (B) Graph of relative FAM fluorescence intensity with different gap distances of Zelos.

4.8. Assembly of the Origami Superstructure and the Nanophotonic Platform

First, the assembly of the three origami (Zelos and two Pandora boxes) was performed in absence of gold nanoparticles to later evaluate the influence of incorporated nanoparticles on the assembly and to optimize the hybridization conditions. To overcome the electrostatic repulsion between the Zelos platform and Pandora's box due to the negatively charged phosphate backbones, a Mg^{2+} screening was performed (**Figure S 8**). On the one hand, the hybridization yield is increased by higher Mg^{2+} concentrations (≥ 20 mM), on the other hand AGE analysis after one day of Zelos-Pandora hybridization revealed a tendency for aggregation visible as a smear in EtBr-stained gel and a strong fluorescence signal in the gel pockets. Using lower Mg^{2+} concentration (11 mM) slows down the hybridization rate (~ 7 days) but reduces the formation of aggregates. Thus, long-term incubation was performed before AGE and TEM analysis and this condition was applied both in absence and presence of gold nanoparticles. **Figure 39** (A) shows the AGE analysis of a fourfold molar excess of Pandora hybridized onto Zelos after seven days, compared to scaffold, Zelos and Pandora alone as negative control. The hybridization process led to the appearance of two new bands (1+2) with a lower electrophoretic mobility compared to the monomer (4) and dimer band (3) of Pandora. It is noteworthy that though the monomer bands of Pandora and Zelos partially overlap, the Zelos monomer band is not visible in the product lane. Thus, most of Zelos is hybridized to at least one Pandora structure. However, partial aggregation, visible as a smear in the product bands, decreases the overall hybridization efficiency. Band excision followed by spin-column extraction and TEM imaging (B) enables the identification of the structures associated to the single bands (1-4). As expected, band 4 and 3 refer to the monomeric and unspecifically dimerized form of Pandora whereas band 2 contains Zelos hybridized to one box and band 1 corresponds to Zelos hybridized to two boxes. Quantification of the band intensities reveals a yield of 16 % for the desired product (band 1), i.e., Zelos with two boxes. The intermediate product (2) is present at 18 %, whereas the Pandora's dimerized form is 13 % and the monomeric form is 53 % of the mixture. Considering the stoichiometry of the full hierarchical structure and assuming that Pandora and Zelos give equal EtBr signals, one can estimate the hybridization efficiency based on the EtBr signal which is around 21%. Nevertheless, the yield should be enhanced by higher excess of Pandora and a longer hybridization time; nevertheless, it is sufficiently high for a first assembly of the nanophotonic platform with respect to the planned single-particle application.

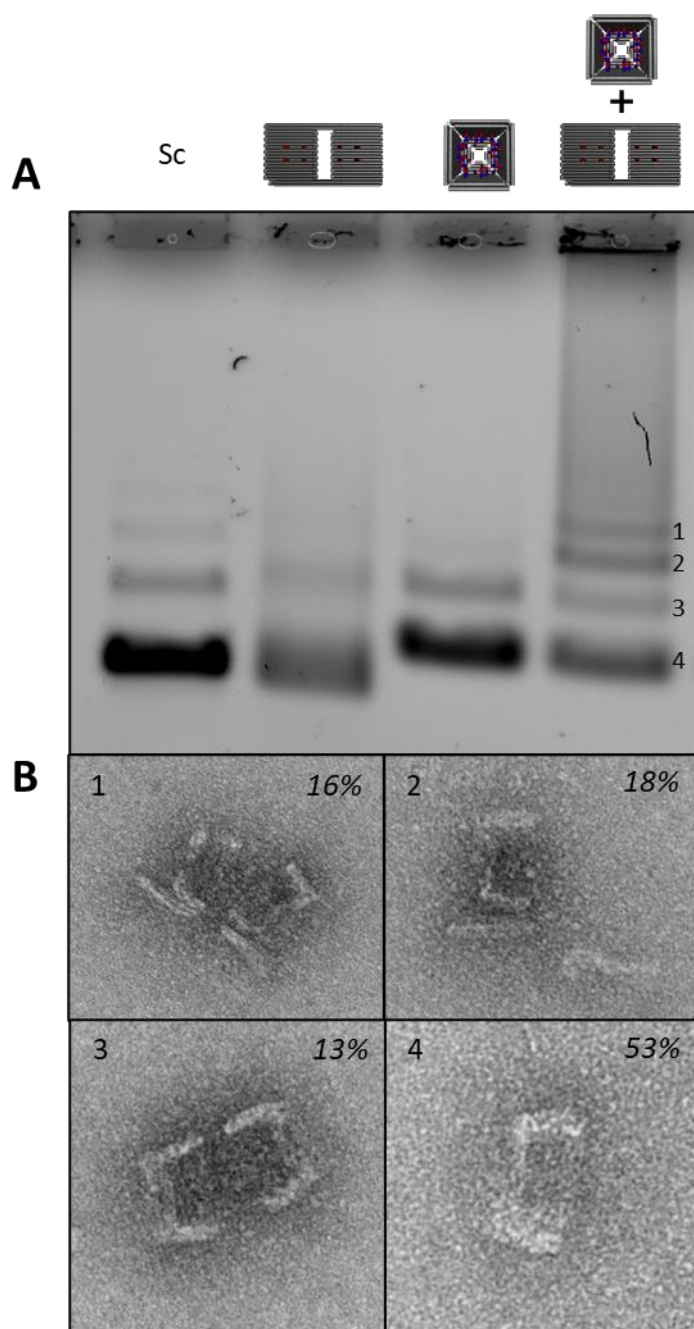


Figure 39: Hybridization of Pandora's Box onto Zelos. (A) AGE of Zelos, Pandora's box and a mixture of both incubated for 7 days (stoichiometry Pandora:Zelos = 3:1, 30 °C, 11 mM MgCl₂. Sc denotes the phage genome scaffold and numbers 1-4 denote excised bands (B) TEM images of the isolated origami structures from the excised bands. Italic numbers denote the resulting yield derived from the summed-up EtBr intensity of the AGE product lane.

4.8.1. AuNP Dimerization with Pandora hybridized onto Zelos

After purification of Pandora-AuNP conjugates with AGE, comparatively low concentrations are obtained because of the low recovery yield by the spin-column extraction method. Sub-nanomolar concentrations of Pandora and Zelos used for the hybridization limits the quantification of the product yield to TEM as the method of choice. However, TEM analysis of long-term incubation solutions containing Pandora's boxes/10 nm AuNP complexes hybridized to Zelos revealed only partially successful formation of the target species as shown in **Figure 39**. Due to the low concentration of Zelos (0.15 nM), TEM images rarely show more than two to three origami, although higher Mg^{2+} concentrations can be used. The resulting TEM images reveal the formation of various intermediate species as those characterized by AGE (**Figure 39**). Single Pandora's boxes with incorporated AuNP as well as Zelos hybridized with one or two boxes are visible. The nanoparticle is mostly found on top or within the core plate, which can be explained by the deformation of the structure in the dry state conditions used during TEM imaging or by the presence of a small design-related "hole" in the core plate where helices cannot be densely packed. The orientation of the boxes onto the platform can be in principle optimized, as boxes would be able to slightly move if they are not hybridized with all four protruding staples located on each side of Zelos. This hypothesis will be addressed in future design-related changes which will involve optimization of the length, position, and sequence of the protruding staples. Introducing additional catching staples at the outer end of Zelos or changing the binding mechanism from hybridization into the wall of Pandora to a zipper-like motive, as reported elsewhere, did not lead to higher hybridization yields but unfortunately caused aggregation. [41]

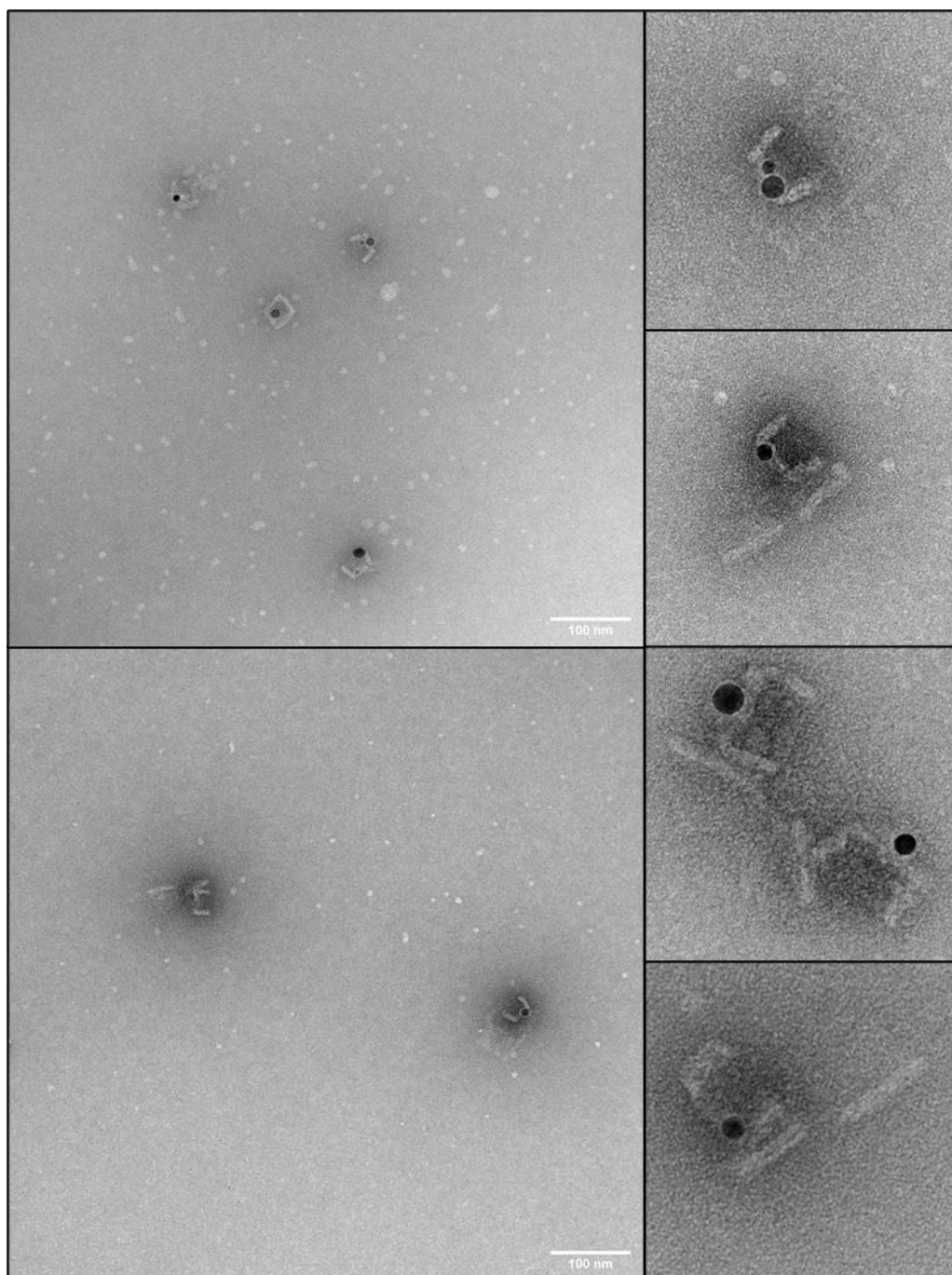


Figure 40: Representative TEM images of AGE-purified Pandora's box-AuNP (10 nm) conjugates (0.6 nM) incubated with Zelos (0.15 nM) for 7 days (30 °C, 1x TE[MgCl₂] [25 mM]).

Statistical analysis of the different species visible in TEM images was used to characterize the overall binding yield of the desired structure. For this aim, Zelos platforms ($n = 98$) were counted and the relative appearance of single Zelos, Zelos hybridized with one Pandora and two Pandoras, respectively, were calculated. 45 % of all Zelos platforms show no hybridization with Pandora's box whereas 51 % are hybridized to one Pandora's box. 4 % of the counted platforms are the desired origami superstructure consisting of one Zelos platform, two Pandora's boxes, each with one gold nanoparticle

incorporated. These results should be understood as a proof-of-principle and in future bigger nanoparticles with different shapes can be incorporated. Also, the distance-dependent plasmonic dimerization will be addressed in future experiments and can be spectroscopically determined at the ensemble level or even at the single-particle level.

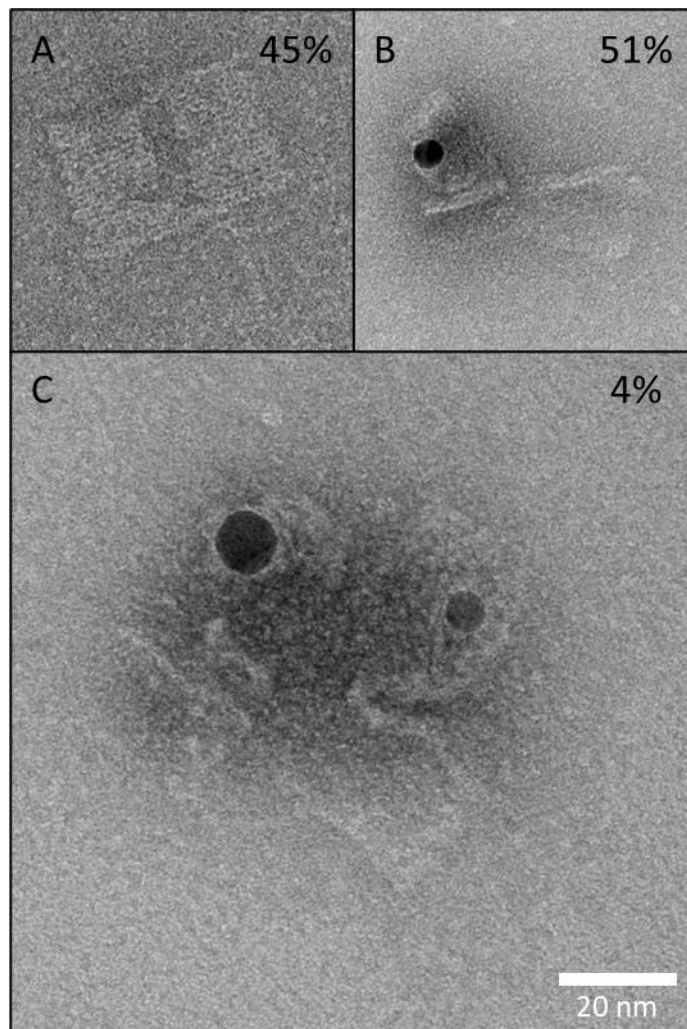


Figure 41: TEM images of the three different species appearing during hybridization of Pandora's box-AuNP conjugates onto Zelos. (A) Unbound Zelos, (B) Zelos with one Pandora's box hybridized and (C) two Pandora's boxes hybridized onto Zelos forming a AuNP dimer. Italic numbers give the yield of the respective species relative to the total number of Zelos. For statistical analysis $n = 98$ Zelos origami were counted.

5. Conclusion and Outlook

The interdisciplinary transfer of knowledge is nowadays a key factor to overcome scientific and technical limitations and gain deeper insights in basic research that can be exploited to develop new applications. Nanotechnology is a perfect example of this interdisciplinary interplay. In this thesis, the programmability of complex 3D DNA structures at the nanoscale and the design of nanoscale devices with modular functions is coupled with the unique plasmonic properties of noble metal nanoparticles. Plasmonic nanoparticles and in particular gold nanoparticles are used since decades as catalysts, diagnostic and therapeutic tools as well as sensors for ultra-sensitive vibrational spectroscopy, namely SERS. In the past few years, the combination of these two fields, DNA nanotechnology and SERS, led to the development of nanomaterials with novel properties and promises to be a powerful tool for the advancement of material science and nanophotonics in the next decades.

The purpose of this thesis was the realization of a complex hybrid platform for nanophotonic applications consisting of three megadalton DNA origami and two gold nanoparticles. The straightforward design and assembly of the hybrid platform for nanophotonics was based on finite difference time-domain (FDTD) simulations of spherical and cubic gold nanoparticles in the size range 8 nm to 18 nm. Through the modification of current synthesis protocols, ~10 nm cubic gold nanoparticles were synthesized, which are smaller in size than the currently published lower limit (~17 nm). The hybrid origami device is designed to enable a site-specific functionalization of gold nanoparticles with sizes up to 18 nm incorporated in a lidless 3D DNA origami box using a new incorporation approach. This new approach, using thiols present on the inner surface of the origami box and surfactant stabilized gold nanoparticles, enables the incorporation of bare nanoparticles with a larger size than what has been shown so far. Furthermore, the colloidal stability of non-covalently stabilized gold nanoparticles with surfaces accessible for linker molecules like thiols was achieved by testing multiple surfactants with Tween20 as molecule of choice. I showed that the incorporation of gold nanoparticles via thiol-chemistry in DNA origami can be the method of choice if spatial limitations are given, which do not allow the use of the widely-used approach based on ssDNA-coated gold nanoparticles. Thiol-based incorporation yields were comparable or even higher than the standard hybridization method, depending on the used gold nanoparticle size and shape.

Finally, two of the origami box-nanoparticle hybrid structures were placed on top of a DNA origami platform, designed to implement the programmable switch of the box-to-box distance. Specifically, the distance between the gold nanoparticles inside the origami boxes can be controlled by varying the length of the bridge spanning the two halves of the platform. The dynamic mechanism is based on the toehold-mediated single-strand displacement and formation of a scaffold loop at the dynamic region

of the platform. In future, this should result in a reversible pulling of the two parts of the platform towards each other, with sub-nanometer precision of the dynamic stepping.

At a certain gap distance (< 5 nm), the two gold nanoparticles located on the two halves of the platform would dimerize, leading to the plasmonic coupling and formation of a hot spot. This hot spot formation can be used in future experiments for ultra-sensitive SERS detection of the interaction between supramolecular ligands and target molecules. In particular, the system can be used upon functionalization of the gold nanoparticles with Raman reporters for single-molecule SERS experiments and spectroscopic evaluation of the simulated SERS enhancement factors presented in this work. Beside this, the design of the DNA origami box as well as the platform should be made more rigid to allow spectroscopic experiments at the ensemble level. In general, optimization of the experimental procedure will be necessary to enlarge the yield of the finally obtained hybrid platform especially if nanoparticles with the maximum size of 18 nm are used.

6. References

1. Erkelenz, M and Schlücker, S (2022) Fundamentals of Nanobiophotonics for Diagnostics and Therapy. In: Schlücker S (ed) Plasmonic Nanoparticles in Diagnostics and Therapy, World Scientific Publishing Company, Singapore
2. Feynman, R (1960), There's a Plenty of Room at the Bottom. *Engineering and Science*, **23**:22-36.
3. Taniguchi, N (1974), On the basic concept of nanotechnology. Proc. Intl. Conf. Prod. Eng., Tokyo pp. 18-23
4. Drexler, E (1986) Engines of creation. *Anchor Books*.
5. Abadeer, NS and Murphy, CJ (2016), Recent Progress in Cancer Thermal Therapy Using Gold Nanoparticles. *J. Phys. Chem. C*, **120**:4691-4716.
6. An, L, Wang, Y, Tian, Q and Yang, S (2017), Small Gold Nanorods: Recent Advances in Synthesis, Biological Imaging, and Cancer Therapy. *Materials*, **10**:1372-1393.
7. Sotiriou, GA (2013), Biomedical applications of multifunctional plasmonic nanoparticles. *WIREs Nanomed. Nanobiotechnol.*, **5**:19-30.
8. Yi, DK, Kaushal, S, Nanda, SS, Samal, S and Yi, DK (2019), Strategies for Development of Metallic Nanoparticle-Based Label-Free Biosensors and Their Biomedical Applications. *ChemBioChem*, **20**:1-26.
9. Kim, T-S, Cha, J-R and Gong, M-S (2017), Investigation of the antimicrobial and wound healing properties of silver nanoparticle-loaded cotton prepared using silver carbamate. *Text. Res. J.*, **88**:766-776.
10. Tran, V, Walkenfort, B, König, M, Salehi, M and Schlücker, S (2019), Rapid, Quantitative, and Ultrasensitive Point-of-Care Testing: A Portable SERS Reader for Lateral Flow Assays in Clinical Chemistry. *Angew. Chem. Int. Ed. Engl.*, **58**:442-446.
11. Burda, C, Chen, X, Narayanan, R and El-Sayed, MA (2005), Chemistry and Properties of Nanocrystals of Different Shapes. *Chem. Rev.*, **105**:1025-1102.
12. Bayford, R, Rademacher, T, Roitt, I and Wang, SX (2017), Emerging applications of nanotechnology for diagnosis and therapy of disease: a review. *Physiol. Meas.*, **38**:R183-R203.
13. Ru, ECL, Blackie, E, Meyer, M and Etchegoin, PG (2007), Surface Enhanced Raman Scattering Enhancement Factors: A Comprehensive Study. *J. Phys. Chem. C*, **111**:13794-13803.

14. Custance, O, Perez, R and Morita, S (2009), Atomic force microscopy as a tool for atom manipulation. *Nat. Nanotechnol.*, **4**:803-10.
15. Seeman, NC (2010), Nanomaterials based on DNA. *Annu. Rev. Biochem.*, **79**:65-87.
16. Watson, JD and Crick, FH (1953), Molecular structure of nucleic acids; a structure for deoxyribose nucleic acid. *Nature*, **171**:737-738.
17. Rothmund, PW (2006), Folding DNA to create nanoscale shapes and patterns. *Nature*, **440**:297-302.
18. Freestone, I, Meeks, N, Sax, M and Higgitt, C (2007), The Lycurgus Cup - A Roman nanotechnology. *Gold Bulletin*, **40**:270-277.
19. Faraday, M (1857), X. The Bakerian Lecture. Experimental relations of gold (and other metals) to light. *Phil. Trans.*, **147**:145-181.
20. Mie, G (1908), Beiträge zur Optik trüber Medien, speziell kolloidaler Metallösungen. *Ann. Phys.*, **4**:377-445.
21. Schlücker, S (2014), Surface-enhanced Raman spectroscopy: concepts and chemical applications. *Angew. Chem. Int. Ed. Engl.*, **53**:4756-4795.
22. Drude, P (1900), Zur Elektronentheorie der Metalle. *Ann. Phys.*, **306**.
23. Maxwell, JC (1873) A Treatise on Electricity and Magnetism. *Dover Publications*, New York.
24. Maxwell, JC (1865), A Dynamical Theory of the Electromagnetic Field. *Phil. Trans. R. Soc. Lond.*, **155**:459-512.
25. (2015) Optical Coherence Tomography: Technology and Applications. *Springer*.
26. Bateman, G (1972), Damping of Electron-Plasma Oscillations in a Uniform Electric-Field. *Phys. Fluids*, **15**:2295-2298.
27. Jaque, D, Martinez Maestro, L, del Rosal, B, Haro-Gonzalez, P, Benayas, A, Plaza, JL, Martin Rodriguez, E and Garcia Sole, J (2014), Nanoparticles for photothermal therapies. *Nanoscale*, **6**:9494-530.
28. Amendola, V, Pilot, R, Frasconi, M, Marago, OM and Iati, MA (2017), Surface plasmon resonance in gold nanoparticles: a review. *J. Phys. Condens. Matter.*, **29**:203002.

29. Link, S and El-Sayed, MA (1999), Size and temperature dependence of the plasmon absorption of colloidal gold nanoparticles. *J. Phys. Chem. B*, **103**:4212-4217.
30. Ringe, E, Langille, MR, Sohn, K, Zhang, J, Huang, J, Mirkin, CA, Van Duyne, RP and Marks, LD (2012), Plasmon Length: A Universal Parameter to Describe Size Effects in Gold Nanoparticles. *J. Phys. Chem. Lett.*, **3**:1479-83.
31. Ghosh, SK, Nath, S, Kundu, S, Esumi, K and Pal, T (2004), Solvent and ligand effects on the localized surface plasmon resonance (LSPR) of gold colloids. *J. Phys. Chem. B*, **108**:13963-13971.
32. Yoon, JH, Selbach, F, Langolf, L and Schlücker, S (2018), Ideal Dimers of Gold Nanospheres for Precision Plasmonics: Synthesis and Characterization at the Single-Particle Level for Identification of Higher Order Modes. *Small*, **14**:1702754.
33. Wang, XP, Walkenfort, B, König, M, König, L, Kasimir-Bauer, S and Schlücker, S (2017), Fast and reproducible iSERS microscopy of single HER2-positive breast cancer cells using gold nanostars as SERS nanotags. *Faraday Discuss.*, **205**:377-386.
34. Wang, XP, Zhang, Y, König, M, Papadopoulou, E, Walkenfort, B, Kasimir-Bauer, S, Bankfalvi, A and Schlücker, S (2016), iSERS microscopy guided by wide field immunofluorescence: analysis of HER2 expression on normal and breast cancer FFPE tissue sections. *Analyst*, **141**:5113-9.
35. Fleischmann, M, Hendra, PJ and Mcquillan, AJ (1974), Raman-Spectra of Pyridine Adsorbed at a Silver Electrode. *Chem. Phys. Lett.*, **26**:163-166.
36. Tanwar, S, Kaur, V, Kaur, G and Sen, T (2021), Broadband SERS Enhancement by DNA Origami Assembled Bimetallic Nanoantennas with Label-Free Single Protein Sensing. *J. Phys. Chem. Lett.*, **12**:8141-8150.
37. Matteini, P, Cottat, M, Tavanti, F, Panfilova, E, Scuderi, M, Nicotra, G, Menziani, MC, Khlebtsov, N, de Angelis, M and Pini, R (2017), Site-Selective Surface-Enhanced Raman Detection of Proteins. *ACS Nano*, **11**:918-926.
38. Kwizera, EA, O'Connor, R, Vinduska, V, Williams, M, Butch, ER, Snyder, SE, Chen, X and Huang, X (2018), Molecular Detection and Analysis of Exosomes Using Surface-Enhanced Raman Scattering Gold Nanorods and a Miniaturized Device. *Theranostics*, **8**:2722-2738.
39. Stepula, E, König, M, Wang, XP, Levermann, J, Schimming, T, Kasimir-Bauer, S, Schilling, B and Schlücker, S (2020), Localization of PD-L1 on single cancer cells by iSERS microscopy with Au/Au core/satellite nanoparticles. *J. Biophotonics*, **13**:e201960034.
40. Xie, W and Schlücker, S (2013), Medical applications of surface-enhanced Raman scattering. *Phys. Chem. Chem. Phys.*, **15**:5329-44.

41. Tapio, K, Mostafa, A, Kanehira, Y, Suma, A, Dutta, A and Bald, I (2021), A Versatile DNA Origami-Based Plasmonic Nanoantenna for Label-Free Single-Molecule Surface-Enhanced Raman Spectroscopy. *ACS Nano*, **15**:7065-7077.
42. Simoncelli, S, Roller, EM, Urban, P, Schreiber, R, Turberfield, AJ, Liedl, T and Lohmüller, T (2016), Quantitative Single-Molecule Surface-Enhanced Raman Scattering by Optothermal Tuning of DNA Origami-Assembled Plasmonic Nanoantennas. *ACS Nano*, **10**:9809-9815.
43. Prinz, J, Heck, C, Ellerik, L, Merk, V and Bald, I (2016), DNA origami based Au-Ag-core-shell nanoparticle dimers with single-molecule SERS sensitivity. *Nanoscale*, **8**:5612-20.
44. Sheikholeslami, S, Jun, YW, Jain, PK and Alivisatos, AP (2010), Coupling of optical resonances in a compositionally asymmetric plasmonic nanoparticle dimer. *Nano Lett.*, **10**:2655-60.
45. Prodan, E, Radloff, C, Halas, NJ and Nordlander, P (2003), A Hybridization Model for the Plasmon Response of Complex Nanostructures. *Science*, **302**:419-422.
46. Hershey, A and Chase, M (1952), Independent functions of viral protein and nucleic acid in growth of bacteriophage. *J. Gen. Physiol*, **36**:39-56.
47. Avery, O, MacLeod, C and McCarty, M (1944), Studies on the chemical nature of the substance inducing transformation of pneumococcal types. Inductions of transformation by a desoxyribonucleic acid fraction isolated from pneumococcus type III. *J. Exp. Med.*, **79**:137-158.
48. Miescher, JF (1871), Über die chemische Zusammensetzung der Eiterzellen.
49. Kossel, A and Neumann, A (1893), Über das Thymin, ein Spaltungsproduct der Nucleinsäure. *Berichte der Deutschen Chemischen Gesellschaft*, **26**:2753-2756.
50. Kossel, A (1885), Ueber eine neue Base aus dem Thierkörper. *Berichte der Deutschen Chemischen Gesellschaft*, **18**:79-85.
51. Kossel, A and Steudel, H (1903), Weitere Untersuchungen über das Cytosin. *Hoppe-Seyler's Zeitschrift für physiologische Chemie*, **38**:49-60.
52. Watson, JD and Crick, FH (1953), Molecular Structure of Nucleic Acids: A Structure for Deoxyribose Nucleic Acid. *Nature*, **171**:737-738.
53. Hunter, CA (1993), Sequence-dependent DNA Structure: The Role of Base Stacking Interactions. *J. Mol. Biol.*, **230**:1025-1054.
54. Hunter, CA and Sanders, JKM (1990), The Nature of Pi-Pi Interactions. *J. Am. Chem. Soc.*, **112**:5525-5534.

55. Sarai, A, Mazur, J, Nussinov, R and Jernigan, RL (1988), Origin of DNA helical structure and its sequence dependence. *Biochemistry (Mosc.)*, **27**:8498-8502.
56. Seeman, NC (1982), Nucleic Acid Junctions and Lattices. *J. Theor. Biol.*, **99**:237-247.
57. Kallenbach, NR, Ma, R-I and Seeman, NC (1983), An immobile nucleic acid junction constructed from oligonucleotides. *Nature*, **305**:829-831.
58. Holliday, R (1964), The Induction of Mitotic Recombination by Mitomycin C in *Ustilago* and *Saccharomyces*. *Genetics*, **50**:323-335.
59. Castro, CE, Kilchherr, F, Kim, DN, Shiao, EL, Wauer, T, Wortmann, P, Bathe, M and Dietz, H (2011), A primer to scaffolded DNA origami. *Nat. Methods*, **8**:221-9.
60. Froehler, BC, Ng, PG and Matteucci, MD (1986), Synthesis of DNA via deoxynucleoside H-phosphonate Intermediates. *Nucleic Acids Res.*, **14**:5399-5407.
61. Garegg, PJ, Lindh, I, Regberg, T, Stawinski, J, Strömberg, R and Henrichson, C (1986), Nucleoside H-phosphonates. III. Chemical synthesis of oligodeoxyribonucleotides by the hydrogenphosphonate approach. *Tetrahedron Lett.*, **27**:4051-4054.
62. Ke, Y, Bellot, G, Voigt, NV, Fradkov, E and Shih, WM (2012), Two design strategies for enhancement of multilayer-DNA-origami folding: underwinding for specific intercalator rescue and staple-break positioning. *Chem. Sci.*, **3**:2587-2597.
63. Douglas, SM, Dietz, H, Liedl, T, Hogberg, B, Graf, F and Shih, WM (2009), Self-assembly of DNA into nanoscale three-dimensional shapes. *Nature*, **459**:414-8.
64. Wagenbauer, KF, Engelhardt, FAS, Stahl, E, Hechtel, VK, Stommer, P, Seebacher, F, Meregalli, L, Ketterer, P, Gerling, T and Dietz, H (2017), How We Make DNA Origami. *ChemBioChem*, **18**:1873-1885.
65. Martin, TG and Dietz, H (2012), Magnesium-free self-assembly of multi-layer DNA objects. *Nat Commun*, **3**:1103.
66. Glaser, M, Deb, S, Seier, F, Agrawal, A, Liedl, T, Douglas, S, Gupta, MK and Smith, DM (2021), The Art of Designing DNA Nanostructures with CAD Software. *Molecules*, **26**.
67. Birac, JJ, Sherman, WB, Kopatsch, J, Constantinou, PE and Seeman, NC (2006), Architecture with GIDEON, a program for design in structural DNA nanotechnology. *J. Mol. Graph. Model.*, **25**:470-80.

68. Douglas, SM, Marblestone, AH, Teerapittayanon, S, Vazquez, A, Church, GM and Shih, WM (2009), Rapid prototyping of 3D DNA-origami shapes with caDNAno. *Nucleic Acids Res.*, **37**:5001-6.
69. Kim, DN, Kilchherr, F, Dietz, H and Bathe, M (2012), Quantitative prediction of 3D solution shape and flexibility of nucleic acid nanostructures. *Nucleic Acids Res.*, **40**:2862-8.
70. Kuzyk, A, Schreiber, R, Fan, Z, Pardatscher, G, Roller, EM, Hogele, A, Simmel, FC, Govorov, AO and Liedl, T (2012), DNA-based self-assembly of chiral plasmonic nanostructures with tailored optical response. *Nature*, **483**:311-4.
71. Kuhler, P, Roller, EM, Schreiber, R, Liedl, T, Lohmüller, T and Feldmann, J (2014), Plasmonic DNA-origami nanoantennas for surface-enhanced Raman spectroscopy. *Nano Lett.*, **14**:2914-2929.
72. Thacker, VV, Herrmann, LO, Sigle, DO, Zhang, T, Liedl, T, Baumberg, JJ and Keyser, UF (2014), DNA origami based assembly of gold nanoparticle dimers for surface-enhanced Raman scattering. *Nat. Commun.*, **5**:3448-3455.
73. Koenderink, AF (2017), Single-Photon Nanoantennas. *ACS Photonics*, **4**:710-722.
74. Li, JF, Li, CY and Aroca, RF (2017), Plasmon-enhanced fluorescence spectroscopy. *Chem. Soc. Rev.*, **46**:3962-3979.
75. Zhang, T, Gao, N, Li, S, Lang, MJ and Xu, QH (2015), Single-Particle Spectroscopic Study on Fluorescence Enhancement by Plasmon Coupled Gold Nanorod Dimers Assembled on DNA Origami. *J. Phys. Chem. Lett.*, **6**:2043-9.
76. Heck, C, Prinz, J, Dathe, A, Merk, V, Stranik, O, Fritzsche, W, Kneipp, J and Bald, I (2017), Gold Nanolenses Self-Assembled by DNA Origami. *ACS Photonics*, **4**:1123-1130.
77. Funck, T, Nicoli, F, Kuzyk, A and Liedl, T (2018), Sensing Picomolar Concentrations of RNA Using Switchable Plasmonic Chirality. *Angew. Chem. Int. Ed. Engl.*, **57**:13495-13498.
78. Nie, S and Emory, SR (1997), Probing Single Molecules and Single Nanoparticles by Surface-Enhanced Raman Scattering. *Science*, **275**:1102-1106.
79. Kneipp, K, Wang, Y, Kneipp, H, Perelman, LT, Itzkan, I, Dasari, RR and Feld, MS (1997), Single Molecule Detection Using Surface-Enhanced Raman Scattering (SERS). *Phys. Rev. Lett.*, **78**:1667-1671.
80. Hendel, T, Wuithschick, M, Kettemann, F, Birnbaum, A, Rademann, K and Polte, J (2014), In situ determination of colloidal gold concentrations with UV-vis spectroscopy: limitations and perspectives. *Anal. Chem.*, **86**:11115-24.

81. Park, JE, Lee, Y and Nam, JM (2018), Precisely Shaped, Uniformly Formed Gold Nanocubes with Ultrahigh Reproducibility in Single-Particle Scattering and Surface-Enhanced Raman Scattering. *Nano Lett.*, **18**:6475-6482.
82. Mehtala, JG, Zemlyanov, DY, Max, JP, Kadasala, N, Zhao, S and Wei, A (2014), Citrate-stabilized gold nanorods. *Langmuir*, **30**:13727-30.
83. Yao, G, Li, J, Li, Q, Chen, X, Liu, X, Wang, F, Qu, Z, Ge, Z, Narayanan, RP, Williams, D, Pei, H, Zuo, X, Wang, L, Yan, H, Feringa, BL and Fan, C (2020), Programming nanoparticle valence bonds with single-stranded DNA encoders. *Nat. Mater.*, **19**:781-788.
84. O'Brien, MN, Radha, B, Brown, KA, Jones, MR and Mirkin, CA (2014), Langmuir analysis of nanoparticle polyvalency in DNA-mediated adsorption. *Angew. Chem. Int. Ed. Engl.*, **53**:9532-8.
85. P. A. E. Piunnoa, J. Watterson, C. C. Wust and Krull, UJ (1999), Considerations for the quantitative transduction of hybridization of immobilized DNA. *Anal. Chim. Acta*, **400**:73-89.
86. Ke, Y, Douglas, SM, Liu, M, Sharma, J, Cheng, A, Leung, A, Liu, Y, Shih, WM and Yan, H (2009), Multilayer DNA Origami Packed on a Square Lattice. *J. Am. Chem. Soc.*, **131**:15903-15908.
87. Erkelenz, M, Kosinski, R, Sritharan, O, Giesler, H, Saccà, B and Schlücker, S (2021), Site-specific facet protection of gold nanoparticles inside a 3D DNA origami box: a tool for molecular plasmonics. *Chem. Commun. (Camb)*, **57**:3151-3153.
88. Abbe, E (1773), Beiträge zur Theorie des Mikroskops und der mikroskopischen Wahrnehmung. *Arch. Mikrosk. Anat.*, **9**:413-486.
89. De Broglie, L (1929), The wave nature of electrons. *Nobel Lecture*, **12**:244-256.
90. Viovy, JL (2000), Electrophoresis of DNA and other polyelectrolytes: Physical mechanisms. *Rev. Mod. Phys.*, **72**:813-873.
91. Trofymchuk, K, Glembockyte, V, Grabenhorst, L, Steiner, F, Vietz, C, Close, C, Pfeiffer, M, Richter, L, Schütte, ML, Selbach, F, Yaadav, R, Zahringer, J, Wei, Q, Ozcan, A, Lalkens, B, Acuna, GP and Tinnefeld, P (2021), Addressable nanoantennas with cleared hotspots for single-molecule detection on a portable smartphone microscope. *Nat. Commun.*, **12**:950-958.
92. Kaminska, I, Bohlen, J, Mackowski, S, Tinnefeld, P and Acuna, GP (2018), Strong Plasmonic Enhancement of a Single Peridinin-Chlorophyll a-Protein Complex on DNA Origami-Based Optical Antennas. *ACS Nano*, **12**:1650-1655.
93. Badshah, MA, Koh, NY, Zia, AW, Abbas, N, Zahra, Z and Saleem, MW (2020), Recent Developments in Plasmonic Nanostructures for Metal Enhanced Fluorescence-Based Biosensing. *Nanomaterials (Basel)*, **10**:1749-1771.

94. Puchkova, A, Vietz, C, Pibiri, E, Wunsch, B, Sanz Paz, M, Acuna, GP and Tinnefeld, P (2015), DNA Origami Nanoantennas with over 5000-fold Fluorescence Enhancement and Single-Molecule Detection at 25 μ M. *Nano Lett.*, **15**:8354-9.
95. Martens, K, Binkowski, F, Nguyen, L, Hu, L, Govorov, AO, Burger, S and Liedl, T (2021), Long- and short-ranged chiral interactions in DNA-assembled plasmonic chains. *Nat. Commun.*, **12**:2025-2031.
96. Yee, K (1966), Numerical solution of initial boundary value problems involving maxwell's equations in isotropic media. *IEEE Trans. Antennas Propag.*, **14**:302-307.
97. Jeanmaire, DL and Duynes, RPV (1977), Surface raman spectroelectrochemistry: Part I. Heterocyclic, aromatic, and aliphatic amines adsorbed on the anodized silver electrode. *J. Electroanal. Chem. Interf. Electrochem.*, **84**:1-20.
98. Johnson, PB and Christy, RW (1972), Optical Constants of the Noble Metals. *Phys. Rev. B*, **6**:4370-4379.
99. Zakeri, B, Niebling, S, Martinez, AG, Sokkar, P, Sanchez-Garcia, E, Schmuck, C and Schlücker, S (2018), Molecular recognition of carboxylates in the protein leucine zipper by a multivalent supramolecular ligand: residue-specific, sensitive and label-free probing by UV resonance Raman spectroscopy. *Phys. Chem. Chem. Phys.*, **20**:1817-1820.
100. Bayer, P, Matena, A and Beuck, C (2020), NMR Spectroscopy of supramolecular chemistry on protein surfaces. *Beilstein J. Org. Chem.*, **16**:2505-2522.
101. Bier, D, Rose, R, Bravo-Rodriguez, K, Bartel, M, Ramirez-Anguita, JM, Dutt, S, Wilch, C, Klärner, FG, Sanchez-Garcia, E, Schrader, T and Ottmann, C (2013), Molecular tweezers modulate 14-3-3 protein-protein interactions. *Nat. Chem.*, **5**:234-9.
102. Wan, LJ, Terashima, M, Noda, H and Osawa, M (2000), Molecular Orientation and Ordered Structure of Benzenethiol Adsorbed on Gold(111). *J. Phys. Chem. B*, **104**:3563-3569.
103. Park, JW and Shumaker-Parry, JS (2015), Strong Resistance of Citrate Anions on Metal Nanoparticles to Desorption under Thiol Functionalization. *ACS Nano*, **9**:1665-1682.
104. Schrader, T, Bitan, G and Klärner, FG (2016), Molecular tweezers for lysine and arginine - powerful inhibitors of pathologic protein aggregation. *Chem. Commun. (Camb)*, **52**:11318-34.
105. Zheng, Y, Zhong, X, Li, Z and Xia, Y (2014), Successive, Seed-Mediated Growth for the Synthesis of Single-Crystal Gold Nanospheres with Uniform Diameters Controlled in the Range of 5-150 nm. *Part. Part. Syst. Charact.*, **31**:266-273.

106. Jana, NR, Gearheart, L and Murphy, CJ (2001), Seeding Growth for Size Control of 5-40 nm Diameter Gold Nanoparticles. *Langmuir*, **17**:6782-6786.
107. Liu, X, Atwater, M, Wang, J and Huo, Q (2007), Extinction coefficient of gold nanoparticles with different sizes and different capping ligands. *Colloids Surf. B*, **58**:3-7.
108. Amendola, V and Meneghetti, M (2009), Size Evaluation of Gold Nanoparticles by UV-vis Spectroscopy. *J. Phys. Chem. C*, **113**:4277-4285.
109. Tang, J, Gao, K, Ou, Q, Fu, X, Man, SQ, Guo, J and Liu, Y (2018), Calculation extinction cross sections and molar attenuation coefficient of small gold nanoparticles and experimental observation of their UV-vis spectral properties. *Spectrochim. Acta A Mol. Biomol. Spectrosc.*, **191**:513-520.
110. Zheng, Y, Ma, Y, Zeng, J, Zhong, X, Jin, M, Li, ZY and Xia, Y (2013), Seed-mediated synthesis of single-crystal gold nanospheres with controlled diameters in the range 5-30 nm and their self-assembly upon dilution. *Chem. Asian J.*, **8**:792-9.
111. Zhao, P, Li, N and Astruc, D (2013), State of the art in gold nanoparticle synthesis. *Coord. Chem. Rev.*, **257**:638-665.
112. Karimi, MA, Mozaheb, MA, Hatefi-Mehrjardi, A, Tavallali, H, Attaran, AM and Shamsi, R (2015), A new simple method for determining the critical micelle concentration of surfactants using surface plasmon resonance of silver nanoparticles. *Anal. Sci. Technol.*, **6**:35-43.
113. Meena, SK and Sulpizi, M (2016), From Gold Nanoseeds to Nanorods: The Microscopic Origin of the Anisotropic Growth. *Angew. Chem. Int. Ed. Engl.*, **55**:11960-4.
114. Meena, SK, Celiksoy, S, Schäfer, P, Henkel, A, Sönnichsen, C and Sulpizi, M (2016), The role of halide ions in the anisotropic growth of gold nanoparticles: a microscopic, atomistic perspective. *Phys. Chem. Chem. Phys.*, **18**:13246-54.
115. Rodríguez-Fernández, J, Pérez-Juste, J, Mulvaney, P and Liz-Marzán, LM (2005), Spatially-Directed Oxidation of Gold Nanoparticles by Au(III)-CTAB Complexes. *J. Phys. Chem. B*, **109**:14257-14261.
116. O'Brien, MN, Jones, MR, Lee, B and Mirkin, CA (2015), Anisotropic nanoparticle complementarity in DNA-mediated co-crystallization. *Nat. Mater.*, **14**:833-9.
117. Jones, MR, Macfarlane, RJ, Lee, B, Zhang, J, Young, KL, Senesi, AJ and Mirkin, CA (2010), DNA-nanoparticle superlattices formed from anisotropic building blocks. *Nat. Mater.*, **9**:913-7.
118. Grzelczak, M, Perez-Juste, J, Mulvaney, P and Liz-Marzan, LM (2008), Shape control in gold nanoparticle synthesis. *Chem. Soc. Rev.*, **37**:1783-91.

119. Zhang, J, Langille, MR, Personick, ML, Zhang, K, Li, S and Mirkin, CA (2010), Concave Cubic Gold Nanocrystals with High-Index Facets. *J. Am. Chem. Soc.*, **132**:14012–14014.
120. Wu, HL, Kuo, CH and Huang, MH (2010), Seed-mediated synthesis of gold nanocrystals with systematic shape evolution from cubic to trisoctahedral and rhombic dodecahedral structures. *Langmuir*, **26**:12307-13.
121. Dovgolevsky, E and Haick, H (2008), Direct observation of the transition point between quasi-spherical and cubic nanoparticles in a two-step seed-mediated growth method. *Small*, **4**:2059-66.
122. Jeon, HB, Tsalu, PV and Ha, JW (2019), Shape Effect on the Refractive Index Sensitivity at Localized Surface Plasmon Resonance Inflection Points of Single Gold Nanocubes with Vertices. *Sci. Rep.*, **9**:13635-13643.
123. Sosa, IO, Noguez, C and Barrera, RG (2003), Optical Properties of Metal Nanoparticles with Arbitrary Shapes. *J. Phys. Chem. B*, **107**:6269-6275.
124. Mackey, MA, Ali, MR, Austin, LA, Near, RD and El-Sayed, MA (2014), The most effective gold nanorod size for plasmonic photothermal therapy: theory and in vitro experiments. *J. Phys. Chem. B*, **118**:1319-26.
125. Link, S, Mohamed, MB and El-Sayed, MA (1999), Simulation of the Optical Absorption Spectra of Gold Nanorods as a Function of Their Aspect Ratio and the Effect of the Medium Dielectric Constant. *J. Phys. Chem. B*, **103**:3073-3077.
126. Niu, R, Song, C, Gao, F, Fang, W, Jiang, X, Ren, S, Zhu, D, Su, S, Chao, J, Chen, S, Fan, C and Wang, L (2021), DNA origami based nanoprinting for the assembly of plasmonic nanostructures with single-molecule surface enhanced Raman scattering. *Angew. Chem. Int. Ed. Engl.*, **60**:11695-11701.
127. Endo, M, Yang, Y, Emura, T, Hidaka, K and Sugiyama, H (2011), Programmed placement of gold nanoparticles onto a slit-type DNA origami scaffold. *Chem. Commun. (Camb)*, **47**:10743-5.
128. Zobel, CR and Beer, M (1961), Chemical Studies on the Interaction of DNA with Uranyl Salts. *J. Biophys. Biochem. Cytol.*, **10**:335-346.
129. Kabiri, Y, Angelin, A, Ahmed, I, Mutlu, H, Bauer, J, Niemeyer, CM, Zandbergen, H and Dekker, C (2019), Intercalating Electron Dyes for TEM Visualization of DNA at the Single-Molecule Level. *ChemBioChem*, **20**:822-830.
130. Elhadj, S, Singh, G and Saraf, RF (2004), Optical Properties of an Immobilized DNA Monolayer from 255 to 700 nm. *Langmuir*, **20**:5539-5543.

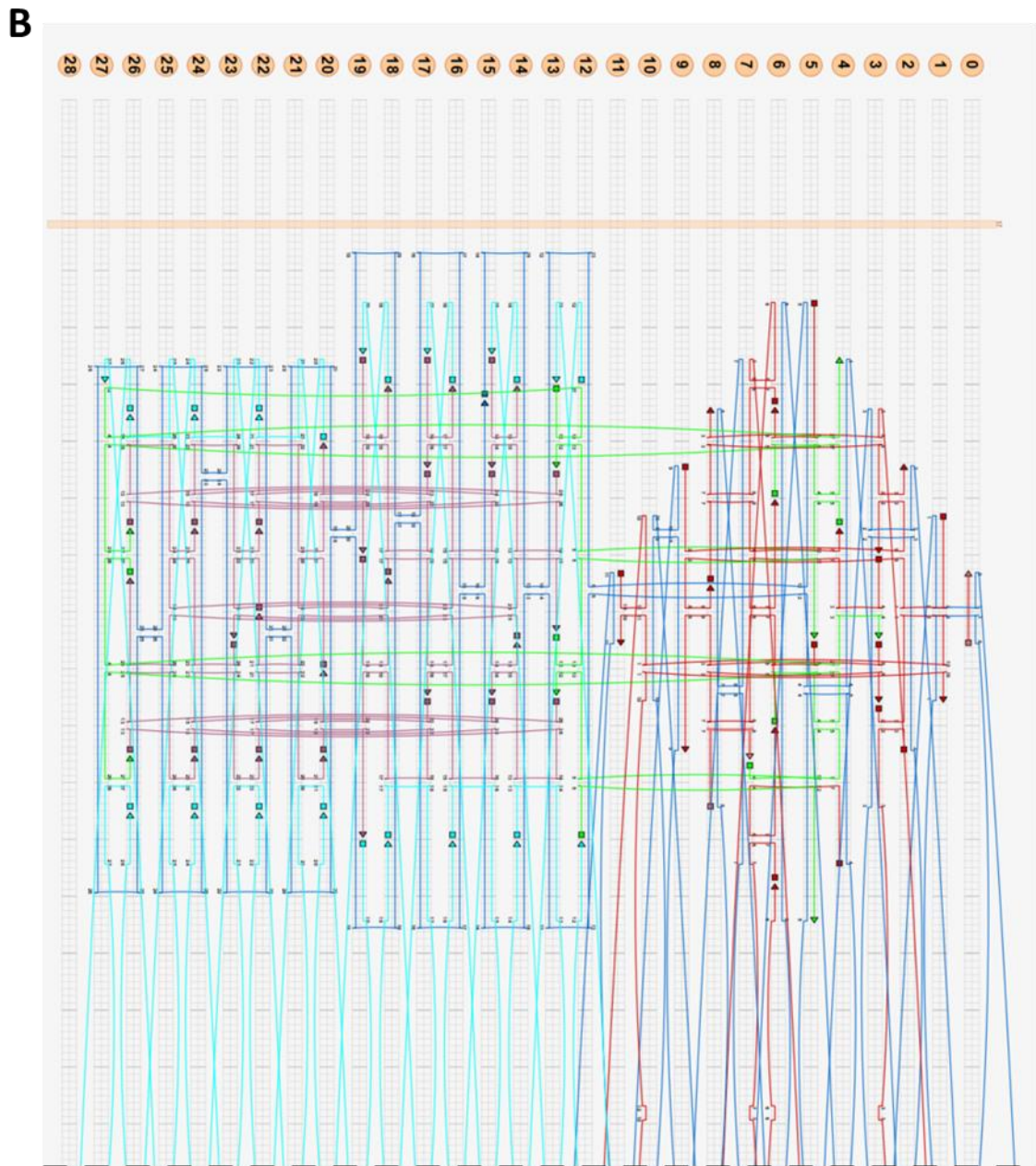
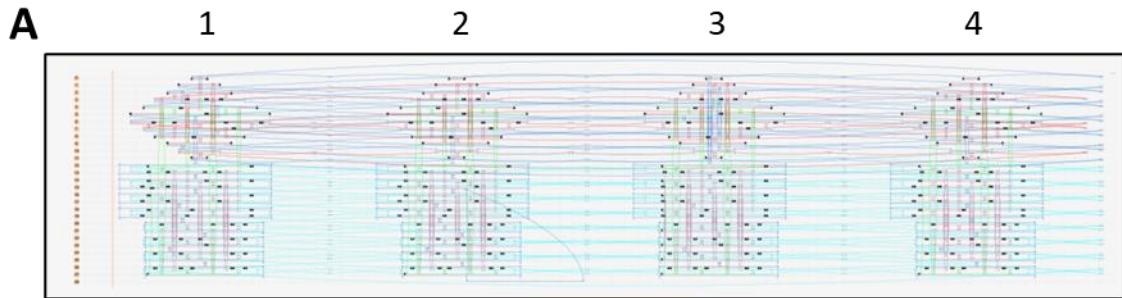
131. Sturtevant, JL, Lee, K, Kunjappu, J, Jockusch, S, Turro, NJ, Widerschpan, T, Zhou, J, Smith, BW, Zimmerman, P and Conley, W (2005), Amplification of the index of refraction of aqueous immersion fluids by ionic surfactants. *Proceedings of SPIE*, **5753**:537-553.
132. Martinsson, E, Shahjamali, MM, Large, N, Zaraee, N, Zhou, Y, Schatz, GC, Mirkin, CA and Aili, D (2016), Influence of Surfactant Bilayers on the Refractive Index Sensitivity and Catalytic Properties of Anisotropic Gold Nanoparticles. *Small*, **12**:330-42.
133. Mock, JJ, Smith, DR and Schultz, S (2003), Local Refractive Index Dependence of Plasmon Resonance Spectra from Individual Nanoparticles. *Nano Lett.*, **3**:485-491.
134. Wu, R, Jiang, LP, Zhu, JJ and Liu, J (2019), Effects of Small Molecules on DNA Adsorption by Gold Nanoparticles and a Case Study of Tris(2-carboxyethyl)phosphine (TCEP). *Langmuir*, **35**:13461-13468.
135. Sharma, J, Chhabra, R, Andersen, CS, Gothelf, KV, Yan, H and Liu, Y (2008), Toward Reliable Gold Nanoparticle Patterning On Self-Assembled DNA Nanoscaffold. *J. Am. Chem. Soc.* , **130**:7820–7821.
136. Grueso, E, Cerrillos, C, Hidalgo, J and Lopez-Cornejo, P (2012), Compaction and decompaction of DNA induced by the cationic surfactant CTAB. *Langmuir*, **28**:10968-79.
137. Turkevich, J, Stevenson, PC and Hillie, J (1951), A Study of the Nucleation and Growth Processes in the Synthesis of Colloidal Gold. *Discuss. Faraday Soc.*, **11**:55-75.
138. Wuithschick, M, Birnbaum, A, Witte, S, Sztucki, M, Vainio, U, Pinna, N, Rademann, K, Emmerling, F, Kraehnert, R and Polte, J (2015), Turkevich in New Robes: Key Questions Answered for the Most Common Gold Nanoparticle Synthesis. *ACS Nano*, **9**:7052-7071.
139. Verwey, EJW and Overbeek, JTG (1948), Theory of the stability of lyophobic colloids. *J. phys.colloid chem.*, **51**:631-636.
140. Debye, P and Hückel, E (1923), The theory of electrolytes. Lowering of freezing point and related phenomena. *Physikalische Zeitschrift*, **24**:185–206.
141. Derjaguin, B and Landau, L (1941), Theory of the stability of strongly charged lyophobic sols and of the adhesion of strongly charged particles in solutions of electrolytes. *Acta Physico Chimica URSS*, **14**:633-663.
142. Vilanova, N and Voets, IK (2016) Introduction to Soft Matter. In: Lang PR and Liu Y (eds) *Soft Matter at Aqueous Interfaces*, Springer, pp. 3-27
143. Majikes, JM, Patrone, PN, Kearsley, AJ, Zwolak, M and Liddle, JA (2021), Failure Mechanisms in DNA Self-Assembly: Barriers to Single-Fold Yield. *ACS Nano*, **15**:3284-3294.

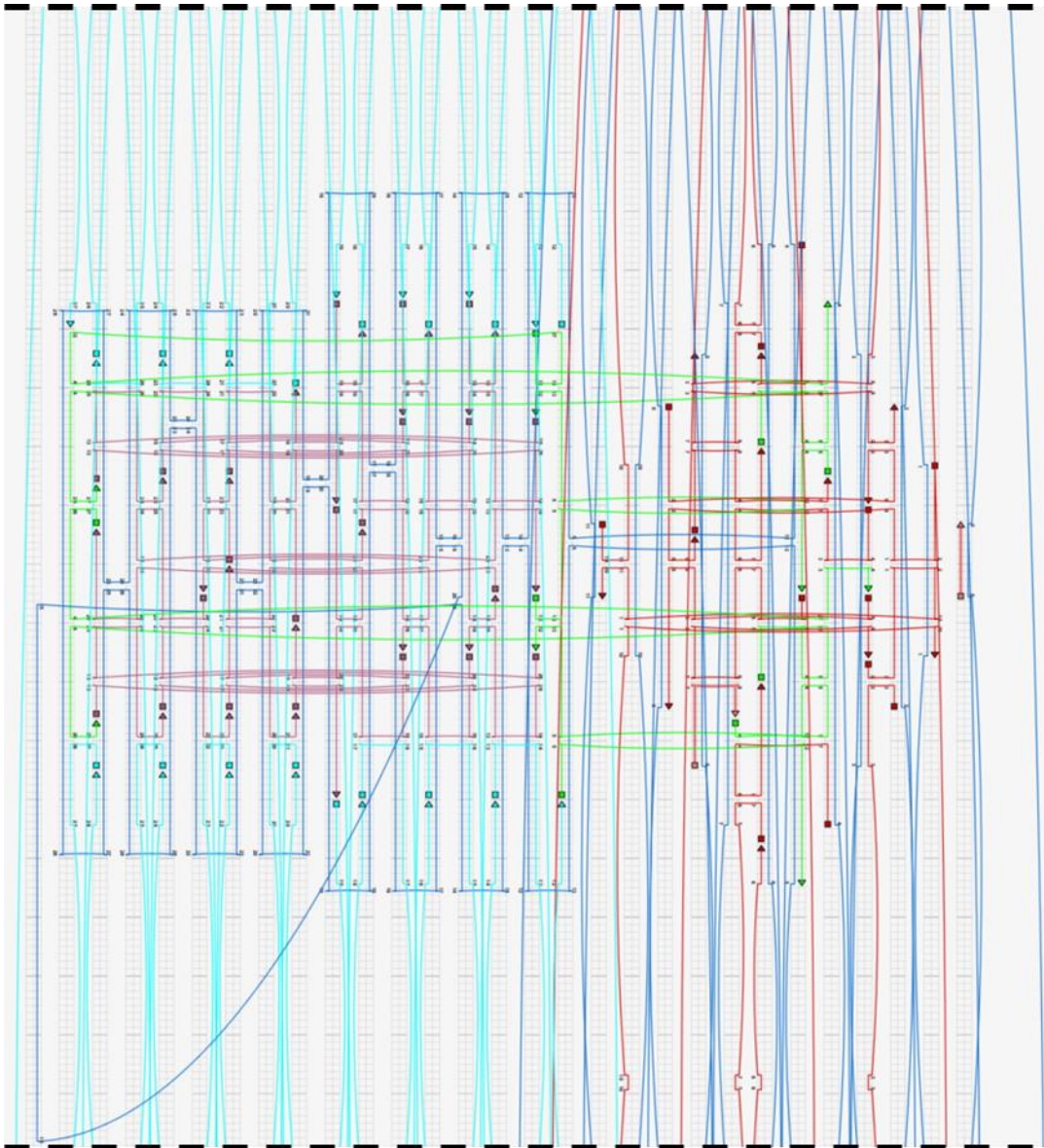
144. Gerling, T, Wagenbauer, KF, Neuner, AM and Dietz, H (2015), Dynamic DNA devices and assemblies formed by shape-complementary, non–base pairing 3D components. *Science*, **347**:1446-1452.
145. Tikhomirov, G, Petersen, P and Qian, L (2017), Fractal assembly of micrometre-scale DNA origami arrays with arbitrary patterns. *Nature*, **552**:67-71.
146. Dunn, KE, Dannenberg, F, Ouldrige, TE, Kwiatkowska, M, Turberfield, AJ and Bath, J (2015), Guiding the folding pathway of DNA origami. *Nature*, **525**:82-6.
147. Podzimek, S (2011) Light scattering, size exclusion chromatography and asymmetric flow field flow fractionation: powerful tools for the characterization of polymers, proteins and nanoparticles. *John Wiley & Sons*.
148. Baalousha, M, Stolpe, B and Lead, JR (2011), Flow field-flow fractionation for the analysis and characterization of natural colloids and manufactured nanoparticles in environmental systems: a critical review. *J. Chromatogr. A*, **1218**:4078-103.
149. Gigault, J, Nguyen, TM, Pettibone, JM and Hackley, VA (2014), Accurate determination of the size distribution for polydisperse, cationic metallic nanomaterials by asymmetric-flow field flow fractionation. *J. Nanopart. Res.*, **16**:2735-2745.
150. Timm, C and Niemeyer, CM (2015), Assembly and purification of enzyme-functionalized DNA origami structures. *Angew. Chem. Int. Ed. Engl.*, **54**:6745-50.
151. Dass, M, Gur, FN, Kolataj, K, Urban, MJ and Liedl, T (2021), DNA Origami-Enabled Plasmonic Sensing. *J. Phys. Chem. C Nanomater. Interfaces*, **125**:5969-5981.
152. Dai, L, Liu, P, Hu, X, Zhao, X, Shao, G and Tian, Y (2021), DNA origami: an outstanding platform for functions in nanophotonics and cancer therapy. *Analyst*, **146**:1807-1819.
153. Kuzyk, A, Jungmann, R, Acuna, GP and Liu, N (2018), DNA Origami Route for Nanophotonics. *ACS Photonics*, **5**:1151-1163.
154. Zhao, Z, Jacovetty, EL, Liu, Y and Yan, H (2011), Encapsulation of gold nanoparticles in a DNA origami cage. *Angew. Chem. Int. Ed. Engl.*, **50**:2041-2044.
155. Luo, X, Chidchob, P, Rahbani, JF and Sleiman, HF (2018), Encapsulation of Gold Nanoparticles into DNA Minimal Cages for 3D-Anisotropic Functionalization and Assembly. *Small*, **14**:1702660.
156. Hurst, SJ, Lytton-Jean, AKR and Mirkin, CA (2006), Maximizing DNA Loading on a Range of Gold Nanoparticle Sizes. *Anal. Chem.*, **78**:8313-8318.

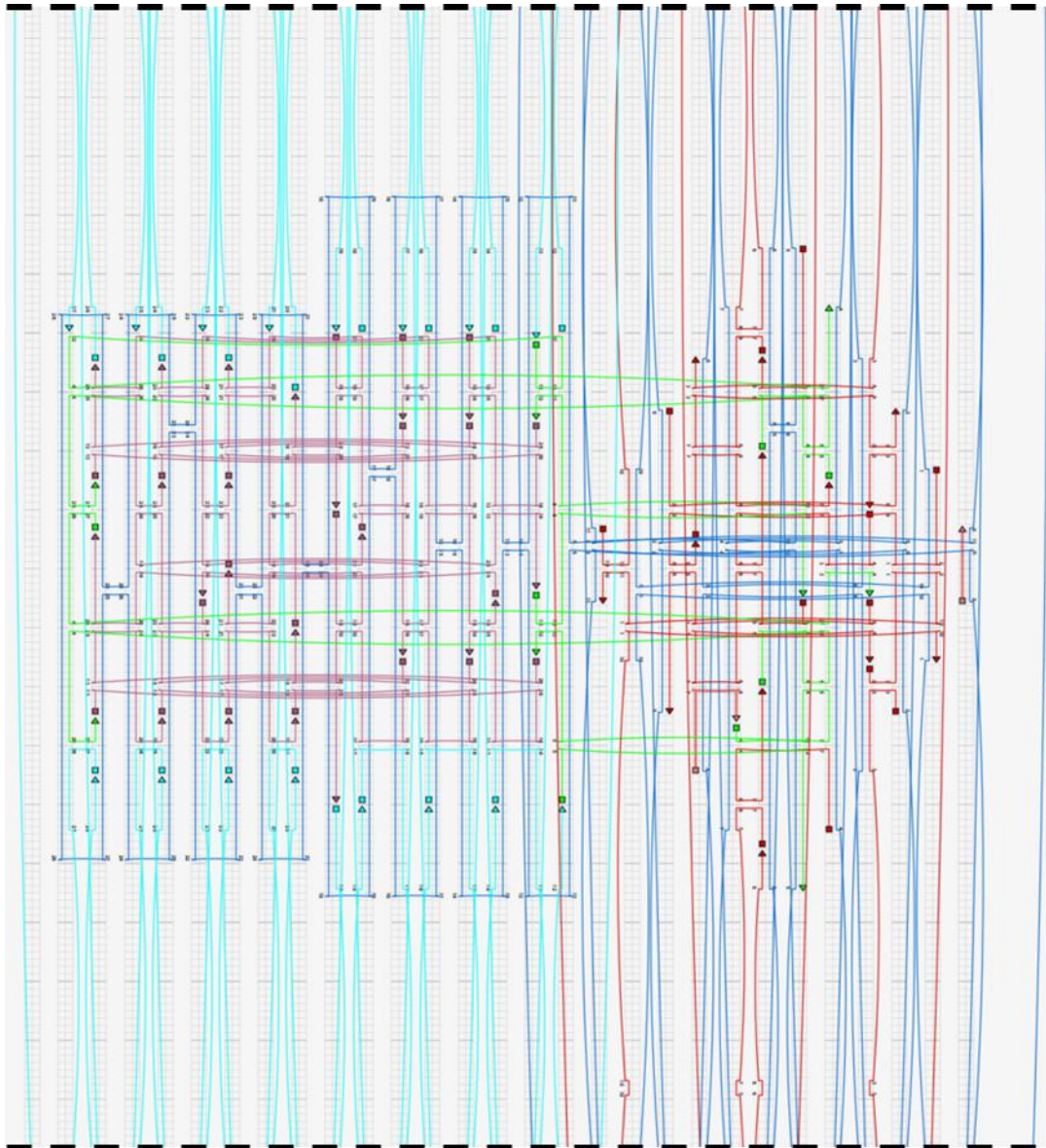
157. Liu, B and Liu, J (2017), Methods for preparing DNA-functionalized gold nanoparticles, a key reagent of bioanalytical chemistry. *Analytical Methods*, **9**:2633-2643.
158. Stahl, E, Martin, TG, Praetorius, F and Dietz, H (2014), Facile and scalable preparation of pure and dense DNA origami solutions. *Angew. Chem. Int. Ed. Engl.*, **53**:12735-40.
159. Shaw, A, Benson, E and Högberg, B (2015), Purification of Functionalized DNA Origami Nanostructures. *ACS Nano*, **5**:4968–4975.
160. Praetorius, F, Kick, B, Behler, KL, Honemann, MN, Weuster-Botz, D and Dietz, H (2017), Biotechnological mass production of DNA origami. *Nature*, **552**:84-87.
161. Zhang, Y, Zhou, H and Ou-Yang, Z-C (2001), Stretching Single-Stranded DNA: Interplay of Electrostatic, Base-Pairing, and Base-Pair Stacking Interactions. *Biophys. J.*, **81**:1133-1143.
162. Haschemeyer, RH and Myers, RJ (1972), Negative staining. *Principles and techniques of electron microscopy*, **2**:101-147.
163. Chi, Q, Wang, G and Jiang, J (2013), The persistence length and length per base of single-stranded DNA obtained from fluorescence correlation spectroscopy measurements using mean field theory. *Phys. A: Stat. Mech. Appl.*, **392**:1072-1079.
164. Roth, E, Glick Azaria, A, Girshevitz, O, Bitler, A and Garini, Y (2018), Measuring the Conformation and Persistence Length of Single-Stranded DNA Using a DNA Origami Structure. *Nano Lett.*, **18**:6703-6709.

A. Appendix

I. Supplementary Information







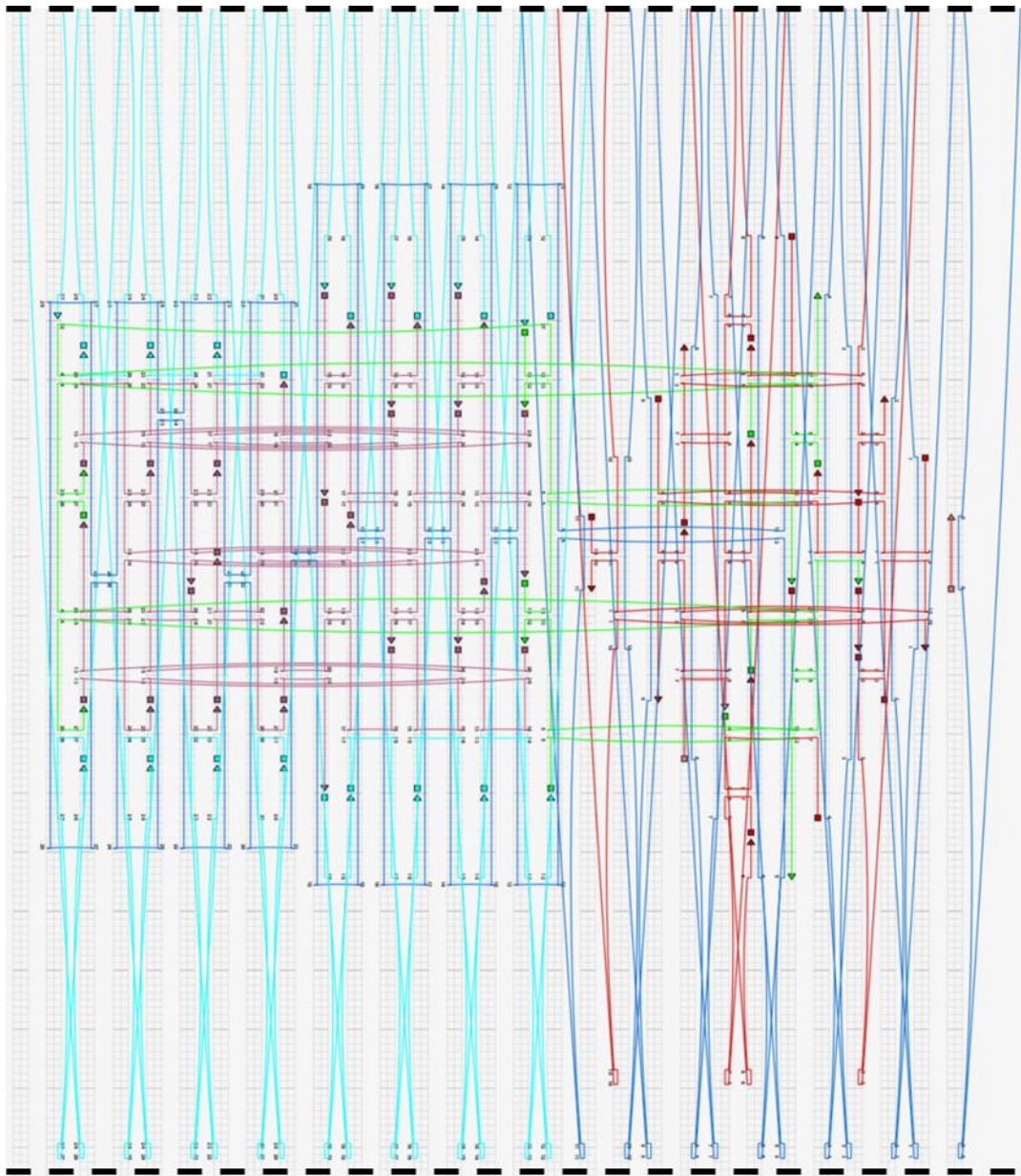


Figure S 1: CaDNAno design of Pandora. (A) Overview of the design. (B) Magnifications of each numbered part. The structure consists of a bottom plate and four walls. Small single-stranded DNA segments are interspersed in between each face to release possible strain. Staples are color-coded (red: bottom plate core staples; green: Staples connecting bottom plate and walls; purple: wall core staples; cyan: Staples connecting walls; magenta: fluorophore-staple; dark blue: edge staples (prevent stacking); orange: protruding staples).

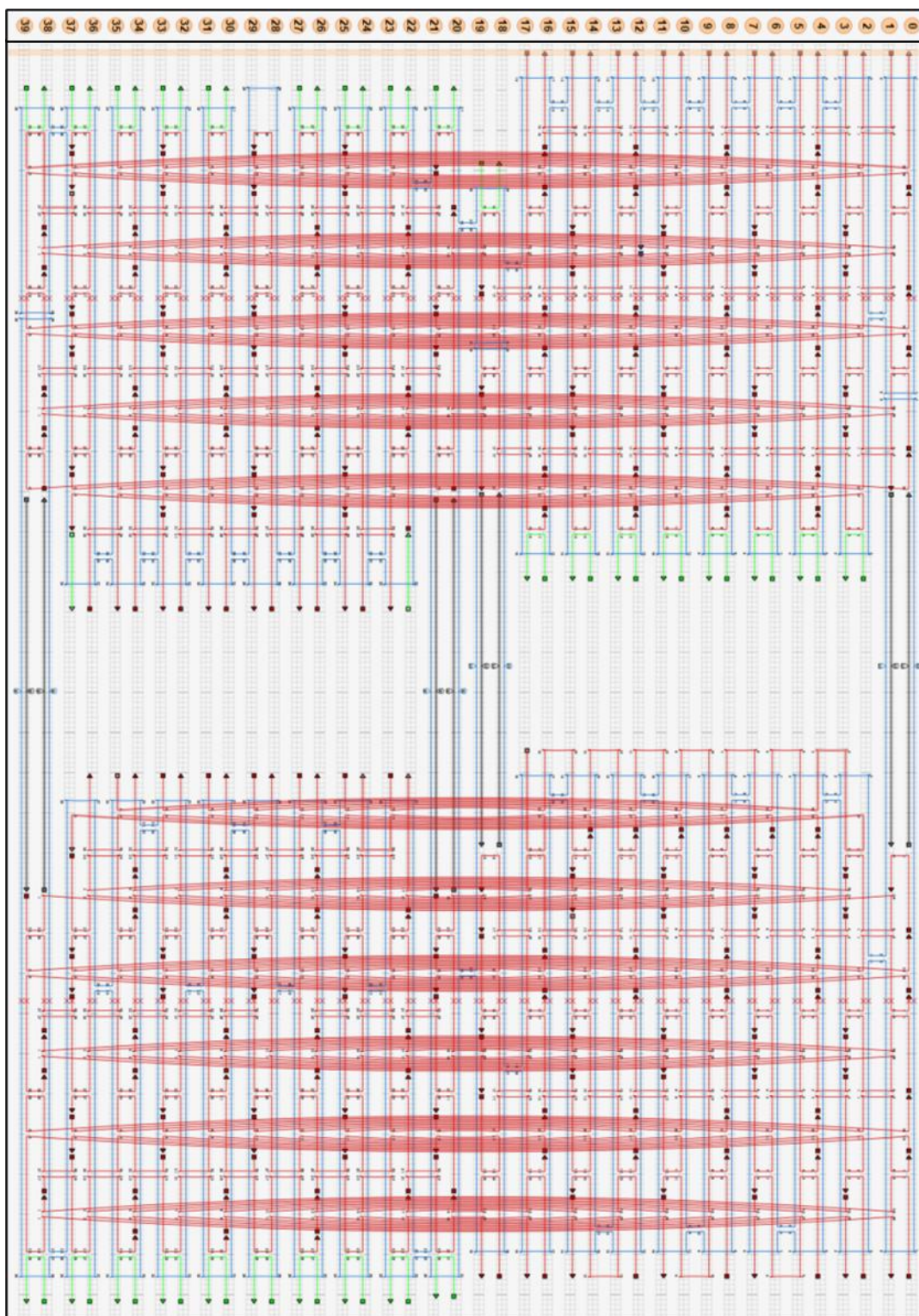


Figure S 2: CaDNAno design of Zelos. The structure consists of two rectangular moieties designed as square-lattice bilayer. Staples are color-coded (red: plate core staples; green: passivating overhang staples; black: fuel staples)

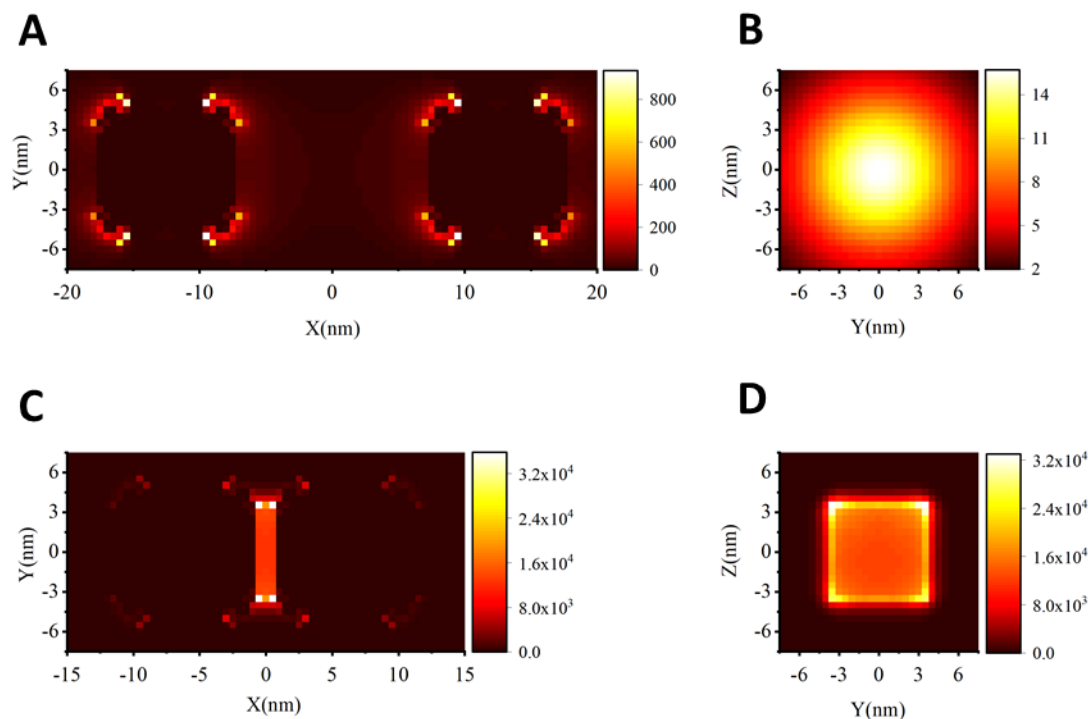


Figure S 3: FDTD simulations with resulting $|E^4|$ SERS enhancement factors of 10 nm AuNC dimers with 2 nm curve-edge radius are shown. Scheme of the planes as well as 15 nm (A, B) and 2 nm (C, D) gap distances in the XY-plane (left) and YZ-plane (right) are shown. FDTD simulations were performed with a TFSF (Total field scattered field) white light source and the data represents the SERS EF values at λ_{max} of the coupled longitudinal dipolar plasmon (LBDP) mode of the sphere dimer.

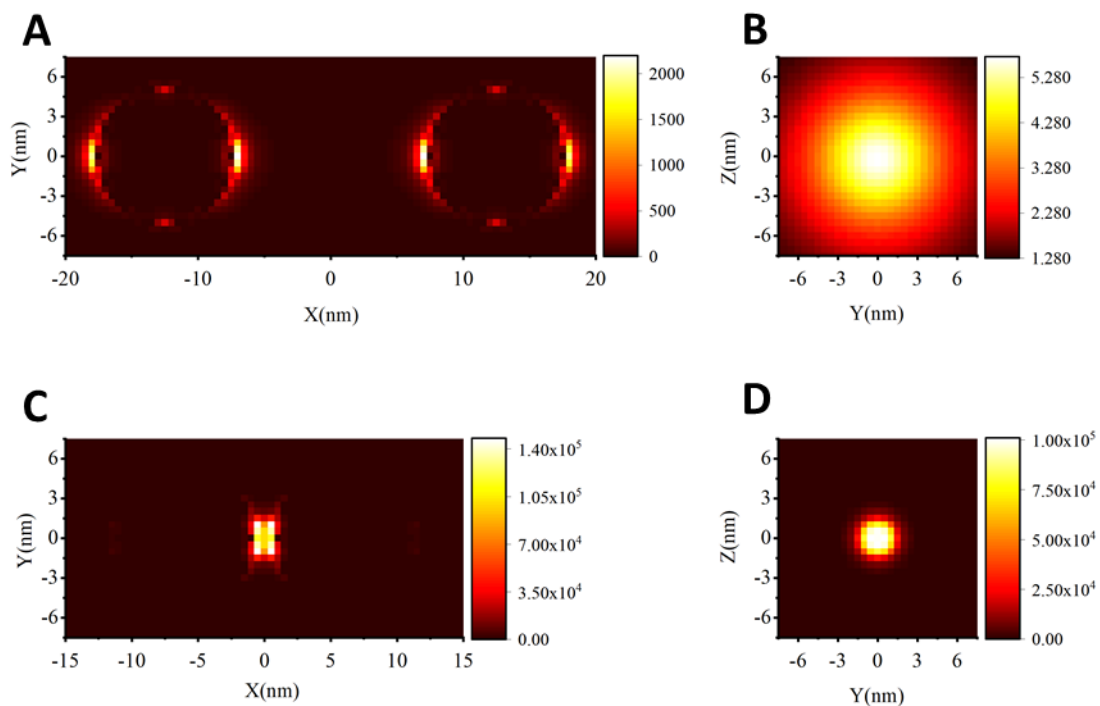


Figure S 4: FDTD simulations with resulting $|E^4|$ SERS enhancement factors of 10 nm AuNP dimers are shown. 15 nm (A, B) and 2 nm (C, D) gap distances in the XY-plane (left) and YZ-plane (right) are shown. FDTD simulations were performed with a TFSF (Total field scattered field) white light source and the data represents the SERS EF values at λ_{max} of the coupled longitudinal dipolar plasmon (LBDP) mode of the sphere dimer.

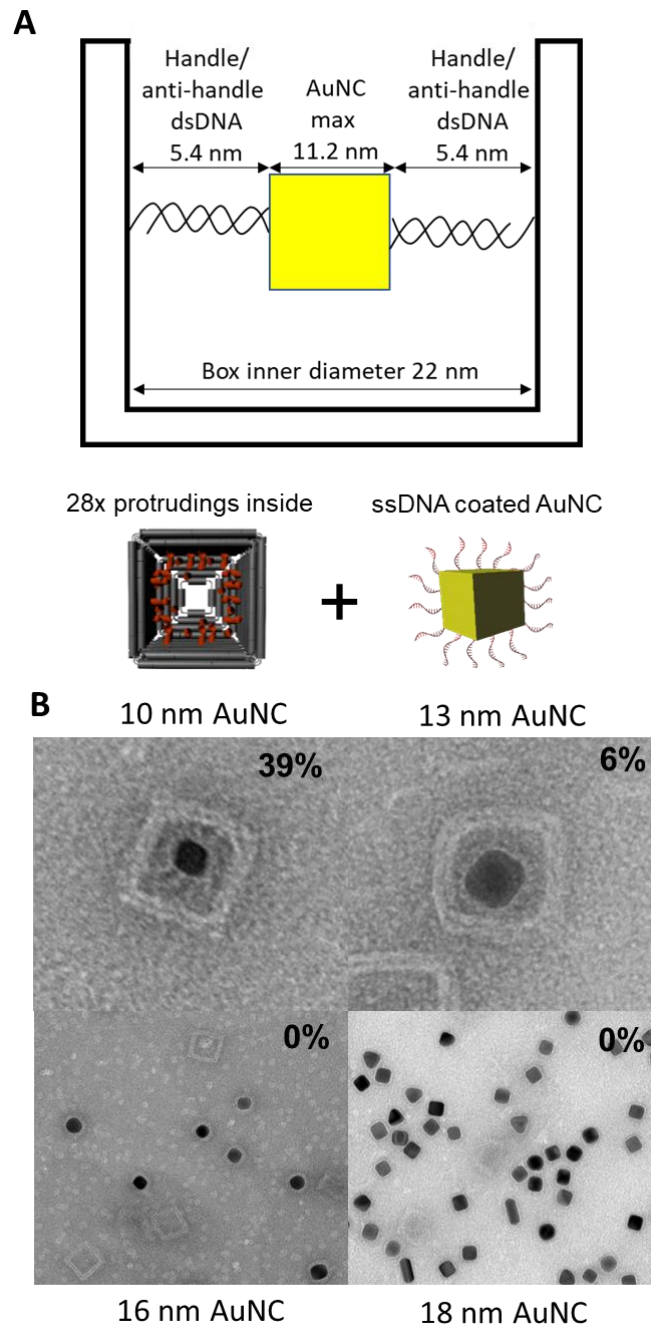


Figure S 5: (A) Hybridization scheme of ssDNA-coated AuNC with maximum dimensions of AuNC fitting in the cavity (dimensions derived by design structure). (B) Experimentally determined yield for the incorporation of AuNC with different edge lengths (10-18 nm) into DNA origami boxes by hybridization. The unsuccessful incorporation of the larger 16 nm and 18 nm AuNC is attributed to steric hindrance and electrostatic repulsion.

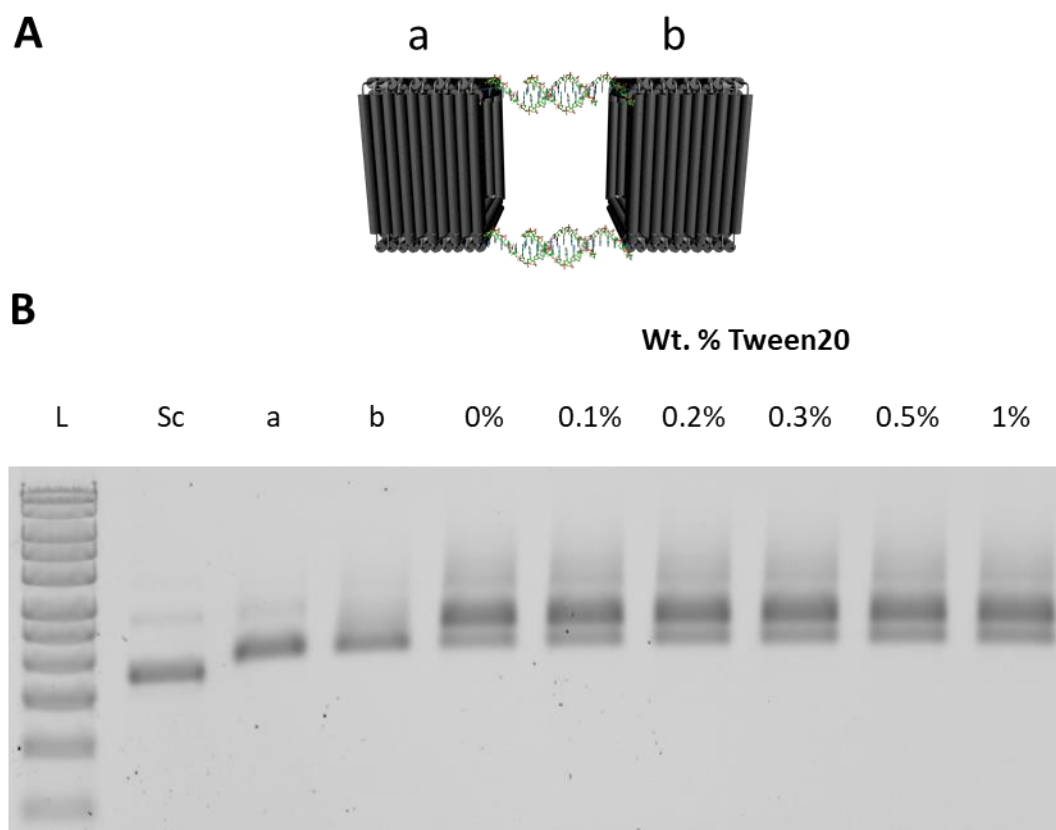


Figure S 6: (A) Dimerization Scheme of Pandora's boxes. Dimerization mechanism is based on four protruding staples located at each corner of box (a) and complementary protruding staples located on another box (b). (B) Different Tween20 concentrations were used while dimerization at 30 °C for 1d. AGE analysis was performed in 1 % agarose gel in 1xTBE[Mg²⁺] [11 mM] for 2 h, 80 V and ice-cooled. The gel was stained by EtBr for imaging after AGE. L denotes the 1 kbp ladder and Sc denotes the scaffold control.

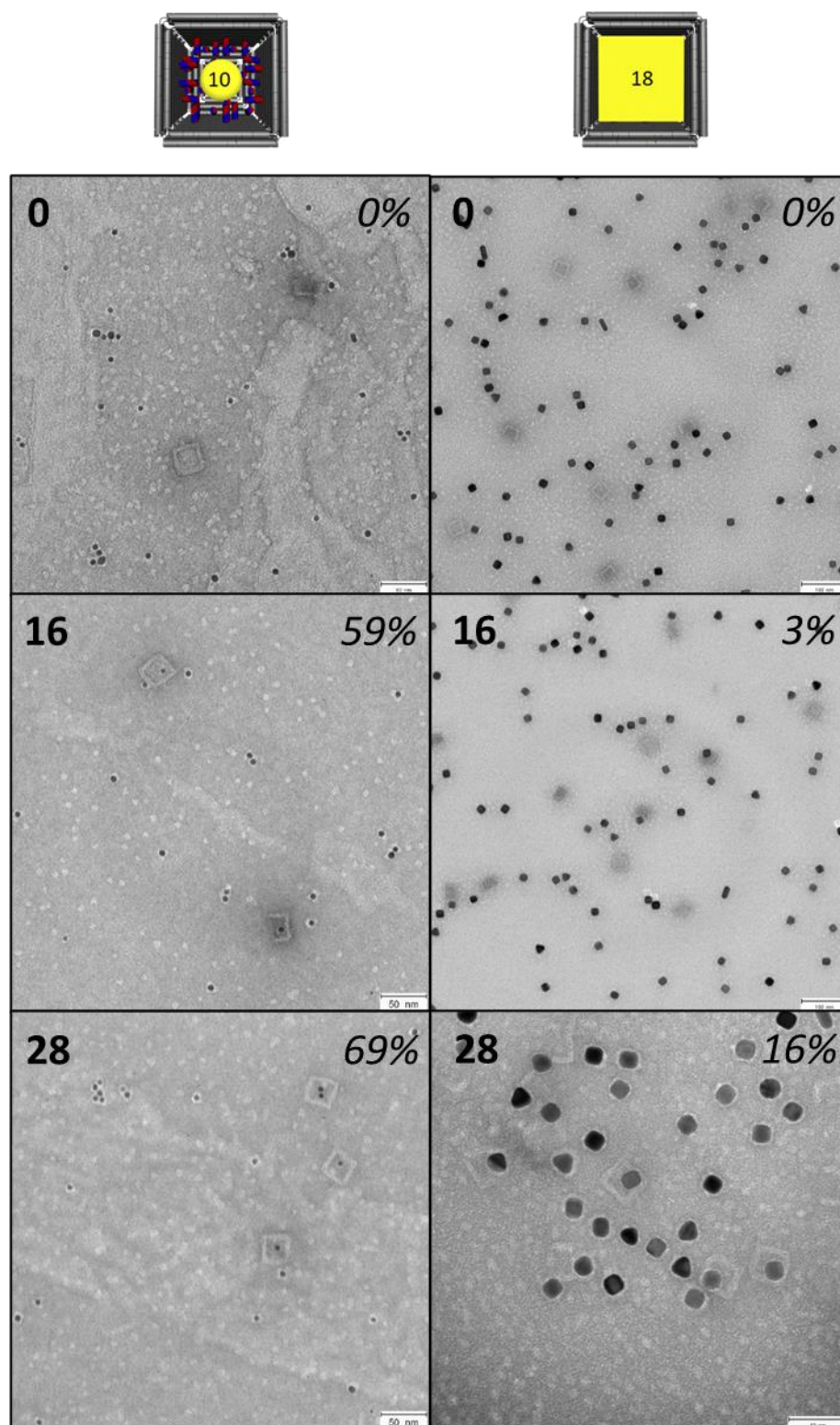


Figure S 7: Incorporation of 8 nm AuNP and 18 nm AuNC into Pandora's box using thiol-chemistry. For conjugation, ten-fold excess of gold nanoparticles was used compared to the molarity of the origami. Representative TEM images of the unpurified colloids after conjugation in $0.5 \times TE[Mg^{2+}]$ [6.25 mM] are shown. For TEM imaging samples were stained with uranyl formate.

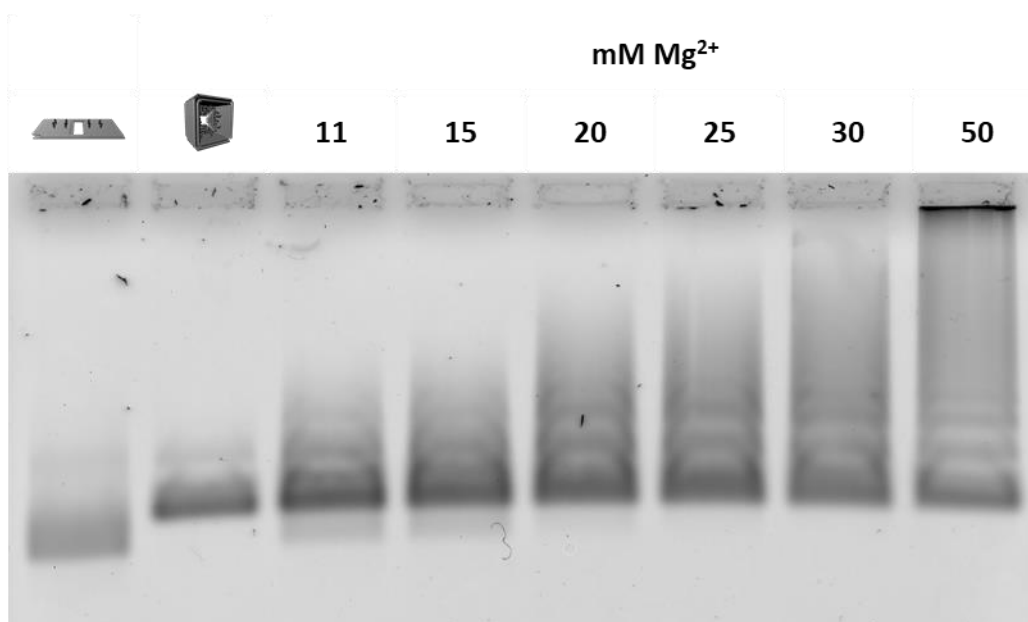


Figure S 8: Mg²⁺-screening of Pandora hybridization onto Zelos. A fourfold molar excess of Pandora was used while incubation for 1 d at 30 °C. Origami were AGE-purified prior to hybridization reaction. The reaction was performed with different Mg²⁺ concentrations to overcome the electrostatic repulsion between the two origami. AGE was performed in 1 % agarose and 1xTBE[Mg²⁺] [11 mM] for 2 h at 80 V and ice-cooled. The gel was stained by EtBr for imaging after AGE.

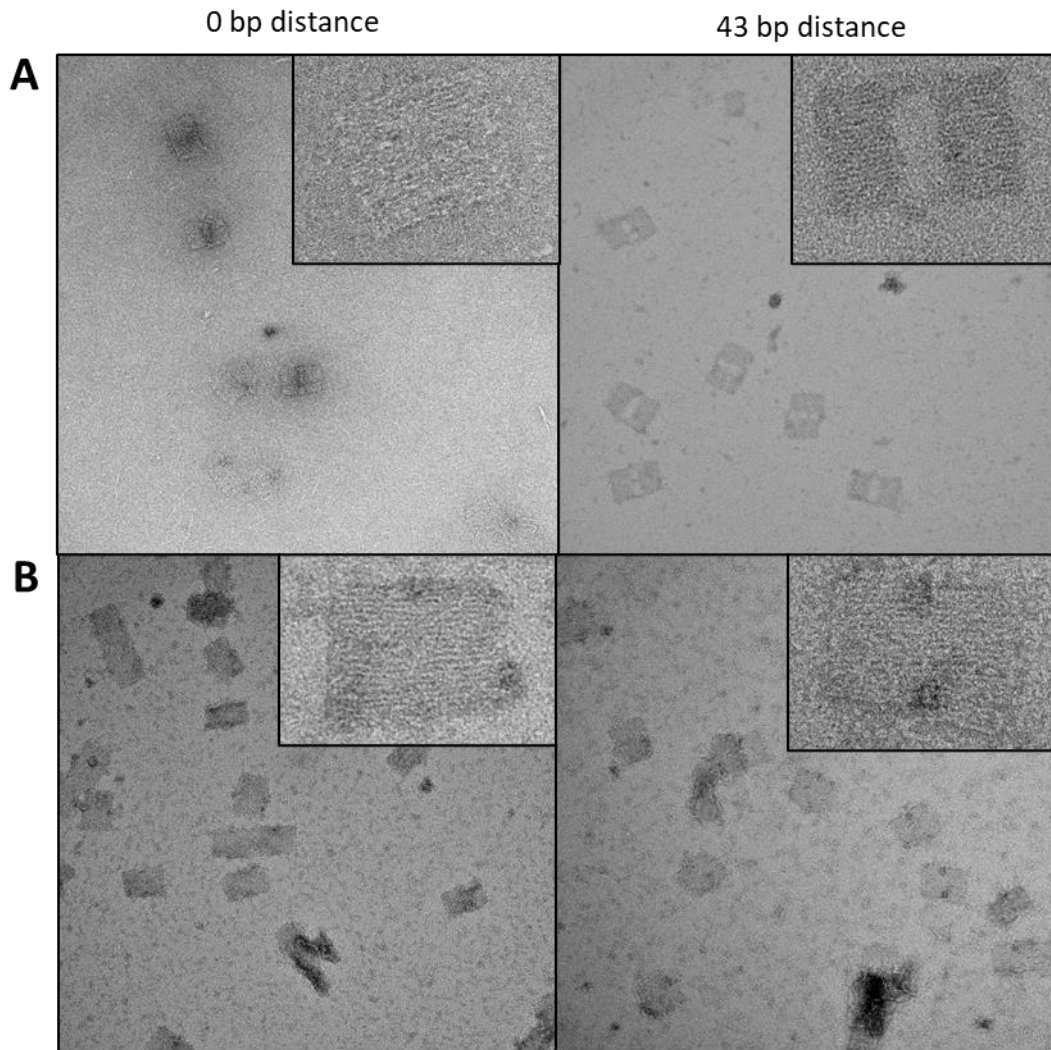


Figure S 9: Zelos assembled with (A) and without (B) overhang edge staple for preventing helical stacking between the inner edges of Zelos. Two different gap distances (0 bp and 43 bp) were assembled and imaged via TEM. Sample A (left and right) serve as negative control while Zelos assembled without overhang edge staple reveals strong helical stacking effects in TEM manifesting in the lack of the 43 bp gap and strong bending of the distance setting helices (B, right).

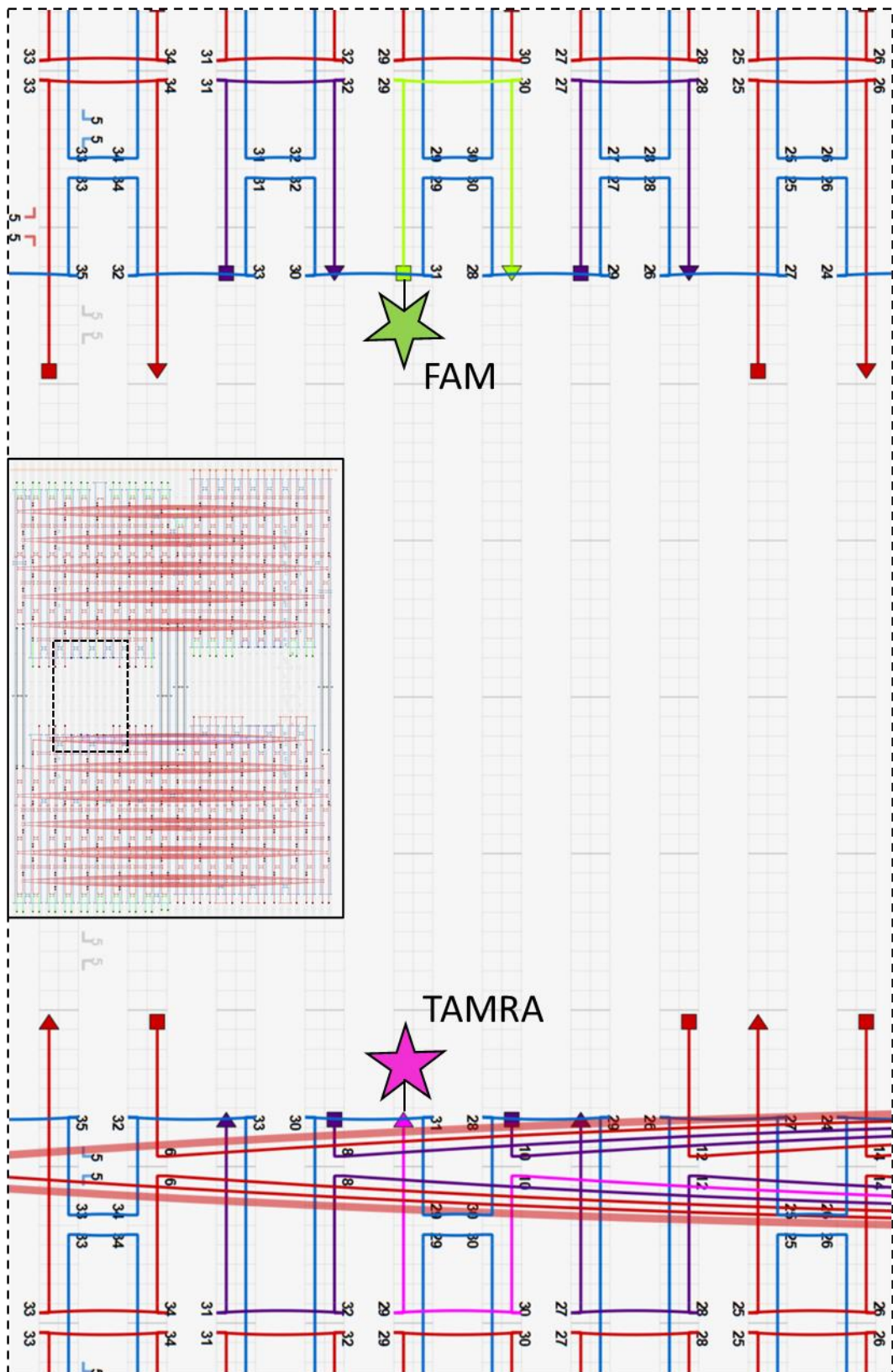


Figure S 10: CaDNAno design of Zelos for FRET spectroscopy. PolyT overhang staples around the FRET pair are exchanged through staples lacking the overhang. Staples are color-coded (red: plate core staples; green: FAM staple; pink: TAMRA staple; dark blue: edge staples without polyT overhang).

II. Lists of Equipment, Materials and Chemicals

Table 4: List of used equipment

Equipment	Company
Precision balance	Sartorius AG
Centrifuge 5424 R; 5430 R; 5810 R	Eppendorf AG
Gel electrophoresis systems	VWR International GmbH
Microwave	Sharp business systems, Deutschland GmbH
Nanophotometer	DeNovix Inc.
Pipettes: Eppendorf Research Plus	Eppendorf AG
Power Source Power Supply, 300 V	VWR International GmbH
Sprout mini centrifuge 12 V	Heathrow Scientific
TEM, EM 910	Carl Zeiss AG
TEM, JEM 1400+	JEOL Ltd.
Thermocyclers	Eppendorf AG
Typhoon FLA 9000	GE Healthcare
UV-Vis, V-730	Jasco
Vortex mixer, VV3	VWR International GmbH
Water purification system	Merck Millipore KGaA
WTW Inolab pH 720	Xylem Analytics Germany Sales GmbH
easiGlow	PELCO

Table 5: List of used consumables

Consumable	Company
Amicon Ultra Centrifugal Filter Units (3, 100 kDa cut-off)	Merck KGaA
PCR Tubes (0.2 mL)	VWR International GmbH
Polypropylene Tubes (15 mL, 50 mL)	Fisher-Scientific
Reaction vessel	Sarstedt AG & Co.
NAP 5, NAP-10 desalting column	GE Healthcare

Table 6: Chemicals & reagents

Chemical/Reagent	Purity	Company
Agarose	MolBio. grade	Biozym
Ascorbic acid	≥ 99.0 %	AppliChem
Boric acid	99.97 %	Sigma-Aldrich
Bromophenol blue sodium salt	MolBio. grade	Sigma-Aldrich
Bis(p-sulfonatophenyl)phenylphosphine dihydrate dipotassium salt	97 %	Sigma-Aldrich
Cetyltrimethylammonium bromide (CTAB)	≥ 96.0 %, ≥ 98 %	Fluka, Sigma-Aldrich
Chloroauric acid-trihydrate	≥ 99.9 %	Sigma-Aldrich
Sodium citrate tribasic-dihydrate	≥ 99 %	Sigma-Aldrich
Deionized water	18 MΩcm	Merck-Millipore

Disodium phosphate-dihydrate	100 %	VWR Chemicals
Ethidium bromide	MolBio. grade	Merck KGaA
Ethylenediamine tetraacetic acid disodium salt dihydrate	MolBio. grade	VWR Chemicals
Glycerin	≥ 99.5 %	ROTH
HCl	37 %	VWR Chemicals
M13mp18 phage genome derivates (p8064)		Tilbit Nanosystems GmbH
Magnesium chloride hexahydrate	≥ 99 %	Sigma-Aldrich
Methanol	≥ 99.8 %	Fisher-Scientific
Monopotassium phosphate	100.1 %	VWR Chemicals
NaOH	ACS	Sigma-Aldrich
Silver nitrate	≥ 99.99 %	Sigma Aldrich
Sodium bromide	≥ 99.5 %	Sigma-Aldrich
Sodium borohydride	≥ 96.0 %	Sigma-Aldrich
Sodium chloride	≥ 99.6 %	Sigma-Aldrich
Sodium dodecyl sulfate	≥ 98.9 %	Sigma-Aldrich
Sodium polystyrene sulfonate (M_w = 70 kDa)	QN 200	Sigma-Aldrich
Tris(2-carboxyethyl)phosphine	MolBio. grade	Sigma-Aldrich
Tween20	MolBio. grade	Sigma-Aldrich

Table 7: Buffer solutions

Buffer/Solution	Composition
PBS (1x)	3.5 mM NaH ₂ PO ₄ , 8 mM Na ₂ HPO ₄ , 50 mM NaCl, pH 8.6
TBE (1x)	89 mM tris base, 89 mM boric acid, 2 mM EDTA, pH 8.0
TBEMg (1x)	40 mM tris base, 20 mM boric acid, 2 mM EDTA, 12.5 mM Mg acetate, pH 8.0
TEMg (1x)	20 mM tris base, 2 mM EDTA, 12.5 mM MgCl ₂ , pH 7.6
1 kb DNA-ladder + gel loading buffer	Carl Roth GmbH + Co. KG

III. List of DNA Sequences

a. Staple Strand Sequences

1. Pandora's Box

Staples of Bottom Core Plate**Start/End**

4[107]6[88]
 2[411]8[523]
 3[544]6[536]
 11[546]1[404]
 0[396]0[386]
 5[236]3[244]
 8[419]7[412]
 6[109]6[110]
 8[547]4[540]
 4[267]6[248]
 1[378]8[388]
 6[522]2[530]
 6[589]6[590]
 9[530]3[543]
 0[236]0[226]
 8[579]7[572]
 3[76]9[91]
 3[384]6[376]
 0[556]0[546]
 6[269]6[270]
 8[387]4[380]
 3[396]9[411]
 3[64]6[56]
 6[42]2[51]
 3[224]6[216]
 1[58]8[68]
 8[67]4[60]
 9[210]3[223]
 5[76]3[84]
 6[202]2[210]
 3[85]11[76]
 5[28]6[43]
 3[565]11[556]
 11[66]1[564]
 9[370]3[383]
 8[259]7[252]
 5[508]6[523]
 3[556]9[571]
 9[51]3[63]
 6[429]6[430]

Sequence

ATTTTGTACAAAAGAAACAGCTGACCTTCATCAAG
 ATGGTAGGTCTGAGAGTTTACCTTTAGAT
 GGTGGGTGAAATTGCTGAGCAAATTGGGCTTGAGATGG
 TTCTGTGCCAACGCTCAACATTTGGGCTTCGCC
 CCGACAAAAAC
 GACCAGGGAACCAGTAAGCAGATAGCCGAACAAAGTGATTT
 GACGCTGAGAAGGAATA
 AGGCTGATGATTTAGCACGGTGTACAGACTTTGCGCAT
 TTGAAAACATAGCAATTACCGTAG
 TTAGCAAACGTATACCAGAAACGAGGCGCAGACGGT
 TGTAGAAACCAATCTGTGCGAATTTTAGATAAAC
 TTAGGCGAATTATTCATTTTCGATAGCTTTTAACTCTAAAT
 AGGCTTAATTTTTTACAAAGCTGCTCATTTTTTGAATA
 AACACCGGAATCATCTTCTGACCCGGCTTA
 CCTGTTTATCA
 CGTCGCTATTAATAACAT
 AGAGAAATCAATTCATCGTAGGAATCATTACC
 AGAGAATAAACTGAAAAGGGATGGGAAGAAAAATCTA
 GAGAATATAAA
 GCCGGAGGAATTTGAGGCGACCTGCTCCATTTACTTA
 AGGGAAGCGCATGAATACCCGCAT
 TTATGTGAATAAAAAAAGGCGTTAAATAAGA
 GAGCGTCTTGATTATTTTTTAAACCGGATATTCATTAC
 ACATTTAACAATTTTCTTCTGCTTCGCAAGACAGAAA
 AATCCAAAACATATAATTAAGAAAGAACTGACCAACTTTG
 AGGCATTTTCGAGCTTACCAACTTTTATTTATAT
 GTGAGTGAATAAGAATTACCACTT
 CCCAATAGCAAGCATGCTATTTTTTATCCC
 AATATGACAAGATGGAAACAGTACAATAAAGCCCATCCTAA
 GAAATAGCTATCTTACCGACAGAGACCATATTATGCACC
 TTTAATTTTATCCTGAATCTAAGTCTTCATCGAGTAAAC
 GCCCTGAGAGAGTTGCAGCAACGTA
 GTACAAATATATTTTAGTTCATGTAATAGTATAAACCAGA
 CGACAAAACAAGCAAGCAAATTTTTACCTTAGG
 AAGAACGCGAGGCGCTCCCGACTTTACAG
 CTGAACACCCTGAACAA
 GGTCACGTTGGTGTAGATGGCAACT
 TAACCCCTTAGAGAAAAAGCCTGTTTAGTATC
 TGCGTTATACCGTGCTACGCGAAAGAAAC
 CGATTTAATCTTTCAGAATCATTGTGAATTTTCTTATG

3[245]11[236] TTTTTGAAGCCTTAAATCATCCTAATTCAAGAACGAGCTA
3[405]11[396] TCATTTGAAATACCGACCGAATGAGAATAATTAATTAAG
2[251]8[363] GGTTGTTTAACTCAATTTTAAAAAGAAT
1[538]8[548] TTTAAACAACGCCAAAATTTATAATTACTAATCC
2[91]8[203] CTACGCCAGTTACAAATTTAACAGTAACC
4[587]6[568] CATATCAAAATTGAAAAACAAGCCCTGACGAGAAACA
4[427]6[408] TACAGTAACAGTAGTTACAATAAGAACTGGCTCATT
5[348]6[363] GATTTGTATCATCGCCTGATGAAAT
11[386]1[244] CAGAGGCGGCTGTCTTTCCTTTTCATTCTACGA
0[76]0[66] ATAGACAGTAA
2[571]8[43] TTTAATGCTGATGCATTTCCAATCTGTA
3[236]9[251] AAACCAGAGGGTATAGAAGGCTTATCCGGTAT
5[556]3[564] TCACAGTAGTAAAGAAGATGATGAAACATTAATTTTTATAT
1[218]8[228] AAAATAATATCCCAAGATTAGTAATCAGATAATT
5[188]6[203] ATTCAACCGATTGAGGGAGGCAGAT
8[99]7[92] AAGAATTGAGTTATAAG
6[362]2[370] CCGAAAACGCAATAATAACGTAGACGGGATAGCAGCCTTGCG
5[396]3[404] GATTCAGGACGTTTCGCCTGATTGCTTTAGTCAATACAAAA
11[226]1[84] ATGTTCCGGTATTAACCAAGTTTCGCACGAACA
8[227]4[220] GAGCGCTAATATAGCCCTTTAAGA
12[583]5[595] GAGAGGCGAGCTGATTGCCCTTCACCGC
13[40]4[36] TAGCCCGATGATGGTGGAGTCTGTAGGGTTAGAACC
26[66]3[75] TGCCGTTGTAGCAATACTTGATTGTTTTCC
4[59]13[51] CTGAACGCTGGTAGGCGAAAATCCTGTTGATA
6[375]26[380] CGTGTGTCAAATTTAAAAGACTCCATTCATATAACAGTTTTTA
13[200]4[196] CACCAGTATCACCGTCTAAACAGTCCACGGAATAAG
6[247]26[253] CAATCATACCCAGCGAATACATAATCTGAAACATGAAAGTTAG
7[253]13[243] AGTGAAAATACTTATACCAAGAGGCAAAAAGAATACTTTC
6[535]26[540] TTTAATTTGCGCATCGTCAGGTTTATAACGGAACGTGCCGGTCT
13[555]5[555] TCCAGCCAGGGTGGTTGCCAGCATCTTTCTTT
4[219]13[211] AACGATATTGACCATTAAGGTGAATTAGCAC
13[361]4[356] CAGATACAGAAAGATGAAGTTTCTTATTACGCAGT
7[93]13[83] AGCTCAATAGAGTTTACCCATATTCCTGATTATCTGAG
12[423]5[435] AGCTTTCAGGCGGATTGACCGTAATGGG
4[539]13[531] ATTTAACCCTGTTTGGGGGACGACGAGTGC
7[413]13[403] CCAACCTTTTAGAACAACTCAACATTAATGTGAACCA
7[573]13[563] CAAATTTGCACCGGGCAACGTTTGCATTTGGGCGTCCG
6[567]26[572] CCAGAACGCAGTGAGAGTAAACAGCGTGGTGCTGGTCTGCACC
12[263]5[275] AAAACGAAAGCGCGAAACAAAGTACAAC
26[226]3[235] ACGTTTCGGAACCTATTATAGGTGGCATAAG
6[215]26[221] AAAGAGGAGAAGGTAACAAAGACATAATGCCCTGCCTAGGG
4[379]13[371] GATTTAAAACGACAACATTATTACAGGTATAA
13[395]5[395] TTTTAGCGAGTAACAACGGAACTAACCCTGCG
26[546]3[555] TTCGACTTGTAGAACGTCAGAAATAAATATA
12[103]5[115] ATTATCATAGCGCCAAAGACAAAAGGGC
26[386]3[395] TGTGATTCCCAATTCTGCGGAAACAATACAT
6[55]26[60] CCAAATCAAGCGGTCCATAATGGACCATCACGCAAATTAATTTT
6[407]26[412] ATACCAGTCTCCGTGGCATCGGGAAACGAGTAGATTTAGTTAAC
13[236]5[235] GAAGACTAAAACACTTTATTGGAAACATCTTT

6[87]26[92] AGTAATCTTAACATATAAATTTCTCTTTGATTAGTAATAATCG
 13[75]5[75] AAGTTAGATGATGGCACCAGCTTGCCATTCATC
 13[521]4[516] GCTTCTGCAGTATCGACATCCTCAACGTCAGATGA

Side Wall Core Staples

Start/End	Sequence
17[212]19[223]	CGGAAAAGCCAGGGTCAGACGATTGGCCTTTAGAGCCCACCCCA
22[219]20[208]	CATTACCCACGTTTTTTGCCTCCCTCAGCAGAACCACGCCGCCA
15[372]22[380]	AAAGCAAAGAGTTGATAATTAAGCAATAACA
26[379]15[371]	AATAAAAAGGAATAGTAAGAGCAACACTTGCA
14[75]26[67]	TTATATCCAGAAATCCTGAGAAG
13[52]24[60]	GGGTTCAAGTGTAGTACAGGAACGGTTTAT
26[59]15[51]	ATAATGAGTGTGGAACAAGAGTCCACTTGGC
19[196]18[200]	CAGAGCCGCCACAGCCGCCA
24[59]17[51]	TTACTACGTGAAAATCAAGTTTTTTGGGAGCT
22[391]14[396]	CAAACCCAAAGCCTCTCAGGGGGCCAGAGAAAAGCCCCATGTT
20[91]19[103]	ATCGTCAGTATTAACACCGC
22[539]20[528]	CATACCCACGACCTCACCGGAAACAACCTTTCTCCACGCAGAA
26[411]15[403]	CTGTGAACGCCAATTCGCATTAATTTTTAAAA
22[59]20[48]	CACGGGGATCAACAATGAAAGCCGGCGCAAGTGTCTGCGCGT
17[84]20[92]	CAGTGAATACGTATATTTTTGAATGGCTAAAC
17[244]20[252]	GCTCCCCTAACATCACCAGTACAAACTATAGT
20[251]19[263]	TAGCATGGGATTTTGCTAAA
22[251]20[240]	TGTACAAAAGGAAAGGAACAACCTAAAGGTTTTCTGTGTAACGAT
15[52]22[60]	CCACATTGCTAACGGGAGGCAGATTCACCGAG
14[235]26[227]	GACTAATCAGTATTGCTAAGTTTTA
17[564]20[560]	CAGTTGAGGATCGCCAGCACGCGTGCCTCTGTGGTGAGTGTAC
13[372]24[380]	CGCCTGCAACTAAGCTTAATTGCTGAATAGAA
20[399]18[387]	ATTCAAAAAAGATTAACCAGACTTTGA
18[66]23[75]	CCTACCCTCAATCAATATCTAATAGATCGAC
17[196]16[200]	GAACCAGAGCCACCCTTATT
19[384]22[392]	TTGCATCAGGGTGAGATAGCTATTCGGCGCAATTCAAAG
17[516]16[520]	CCAAGCTTTCAGCAGGGTTT
24[411]17[403]	CATCAAGATTGTAATCATATGTACCCCGCTGA
17[36]16[40]	CCCCGATTTAGGTCGAGGT
15[212]22[220]	ACTGCCTCGTTCTTTACCAGAACCGCCATCCT
22[571]20[572]	CAAATCGTTAACGCCGGGTTACCTGCAGTCCA
22[91]20[80]	GTAATGGCAAATTGAAAAATCTAAAGCATGAGGCGGCCATTA
20[411]19[423]	GTGTAGACAGTCAAATCACC
26[252]15[243]	GATTAACCGGGTCAGAGGCTTTGAGGACGCGG
13[244]24[252]	CATTGCGGGTTCCAGGCGGATAAGTGCATAG
15[84]22[92]	ATACTGACGCTCAATAAAAGGGACATTCAAGC
13[404]24[412]	ATAGTTAGCTATGGGGCGCGAGCTGAAATTAA
17[360]24[364]	GAATCCCAGACTGGATGCTCCTTGTC
24[379]17[371]	TTAGAAGTTTTGTAATAGTAAAATGTTTCTCA
19[516]18[520]	GTGAGAGATAGATCGGCGAA
14[395]26[387]	AAATGTACATTTATTTTGCTCAACA
18[546]23[555]	ATAGGAACCCGTGAGCCTTATCCGCCTGG

19[224]22[232] GACGTTAGTAAATGAAAATTGCGACACTTTCGCTGAGAAA
26[91]15[83] GCCTATTATCATTAAATCCTTTGCCCGGATA
15[244]22[252] GATCATCACCGTCTCAGAGCCACCACCCCA
15[360]26[364] GAGGCTTATCATAACTGGCTTAGAAGT
20[239]18[227] CTAAGTTTTGTCGCTTGATATTATAAT
15[564]22[572] TACGACTCAATCGGGTAAAGTTTCTTTTCAG
24[219]17[211] CCACTAGCGGTATTTTCGGTCATAGCCCCAC
15[36]14[40] CTATCAGGGCGAATTAAGA
23[76]13[74] CAGTAATCGTCTGAAATGGAACGCCAGATAAAGTTTGTCCTTTAA
13[84]24[92] TAACTGCTGGTACAATATTACCGCCAGCCTAC
22[411]20[400] AGAACTGGAGCATTAAATGCCGGAGAGGGAAGGCCGGAGGTAAAG
13[532]24[540] CGGAGCTGGCAGTGTGATTGCCGTTCCGGTA
17[404]20[412] GAGTGCCTTTATGGATAAAAATTTTAGTAAT
23[236]13[235] CCACACTCAGGAGGTTTAGTGTACTGGTTTTCCGGACAAGGTCATGAG
22[379]20[368] GGTCCTCAAAGATCTATAAACAGTTCATCAGAAGCGCCCGAAA
15[196]14[200] TTGCCTTTAGCGCCATCGAT
15[404]22[412] CAGGCAATAAATAAGCTAAATCGGTTGTCGGG
19[36]18[40] GCTAGGGCGCTGAACGTGGC
17[372]19[383] AATGAGGATTAGTTCGAGCTTCAAAGCGAAGAGGAAAAAGCGGA
15[532]22[540] AGGGCCGTTAGTGGCCTGGTCACTGTTGTCGA
19[64]22[72] GAAGATAAAACAGAGGTCACCTGTATAGACAGGCACGGT
22[551]14[556] TGTGTACACCCTGCGGTCAGGCGATGCAACAATTCCACACGCGC
22[71]14[76] TGCTTTGACAGTCACATAGACCCACCATCAGCCGTCATAAACG
20[571]19[583] GCGCCTGCGCCAGAATGCG
20[79]18[67] AATACCGAACGAACCAGCGCTACCTGAA
19[360]22[364] TATTATAGGAAAACGACGTTTTAAAGAG
13[212]24[220] CATTGCCTTGAGTTGATGATACAGGAGTACCG
22[231]14[236] CAAATAAACCTCAGAAGTTCGGCTTTCATGCGCCGATTTTAAA
24[91]17[83] ATTTATTTGAGGTAGGAGCACTAACAACCTGGT
18[226]23[235] AATTGAAAATCTCAAAAAATACCGATACCG
26[539]15[531] CGTCAACCAGGCTCGCCATTACAGGCTGCCGAA
26[220]15[211] TCAGTACCATTAGAACGTACCAATGAAATCAG
24[571]17[563] TCGCAGCCGGAATTCCTGTGTGAAATTGCTCA
23[396]13[394] CATAACAGGCAAGGCAAATAATGCTCAGAGGCATTACGCTCATT
13[564]24[572] GAAAGTGGTGCCACCAGCTTACGGCTGGGCTT
26[571]15[563] GTCGCCTGTGTTACATTAATTGCGTTAACA
23[556]13[554] TAATCGCCGGGCGCGGTTGCGGCAAACGTGCGCCATAAGCCCGCTT
15[516]14[520] TACGCCAGCTGGGCAACTGT
24[251]17[243] GTGTGTCACCCTTTTCTTAAACAGCTTGAAAG
17[52]19[63] TGACTATAACGTAATGCGCCGCTACAGGCCATCACGAGCGGGCA
18[386]23[395] GAGGCTATCAGGTCATTGCGTTGATAAAGAG
17[532]19[543] GGAGAAAAAATCCTGCTCATTGCGCCAAAAAGAGGTGGTGAA
24[539]17[531] TGAGGGATGTGCTTAAGTTGGGTAACGCAGGT
14[555]26[547] TCACCGGACGCAATCCCTCCGTTTT
20[559]18[547] TGCGCGCTCTCACGGAGCAGTTGCGTGG
19[544]22[552] GGGATAGCTGTGCACTGTTCTTCGGGCCAGATGGCATGGT

Staple Connecting Side Walls

Start/End	Sequence
20[367]20[260]	GACTTCAAATATTTTAGACAGCC
14[39]14[584]	ACGTGGACTCCAATTTGCCTAATGAGT
16[519]16[424]	TCCCAGTCACGATTTAATCGTAAACT
18[519]18[424]	ACGTACAGCGCCTTTCAACCGTTCTAG
12[199]12[104]	ACCGACTTGAGCTTTAGAAGGAGCGGA
20[419]22[524]	TGAGAACCCTCATATATTTAACTTAAATTTCCGT
24[419]26[524]	AGCAAGGTGGCATCAATTTTAAGTTAAACGACCTC
22[363]22[260]	TACCTTTTTTGCCEAATA
12[519]12[424]	GCCTCAGGAAGATTTCTTCCTGTAGCC
26[523]26[420]	CGGCCAGTTTGC AAATGG
22[419]24[524]	TTTGACCAAAAACATTTTTGCCGCACAGGCGATG
16[39]16[584]	GCCGTAAAGCACTTTGTAATCATGGTC
24[523]24[420]	AAGGGTATTTTATAGTAGT
18[39]18[584]	GAGAAAGGAAGGTTTCGGTCATACCGG
26[259]27[359]	GGATATTAAGAGGCTGTTTCTG
16[423]15[515]	AGCATGTCATAAGCAAATATTTAAATTGTTTTTCGCTAT
19[584]19[35]	GCGGGCCGTTTTTGGAGCGGGC
12[359]12[264]	TCATCAGTTGAGTTTAGGCACCAACCT
16[199]16[104]	AGCGTTTGCCATTTAAGGTTATCTAA
20[207]20[100]	GCATTGACAGGTTTCTGATAGC
24[363]24[260]	TTTTTGCTTTGTATAGCC
18[359]18[264]	GAATGACCATAATTTTCAGCGGAGTG
18[423]17[515]	CTGATAAAAACAAGAGAATCGATGAACGTTTGGCCAGTG
26[363]26[260]	ACGGTGTTTTCAAGAGAA
24[43]24[580]	GAGGCCGTTTGT CATTGC
22[203]22[100]	GAAAGCGTTTCTTCTGAC
18[583]17[35]	GGGTTTCTCCGGGTACCGAGCTCGAATTTAAAGGGAG
24[99]26[204]	ATACCATTGCAACAGGTTTATACATGGCTTTAAC
14[423]13[520]	TTGTTAAATCAAAAATAATTCGCGTCTGTTTGCTTCCGGCACC
24[259]25[359]	CGGACGTCGAGAGGGTTTTGGA
26[99]27[199]	AACTACATCACTTGCCTTTTGTA
16[263]15[359]	GAGGTGAACAGCAGCGAAAGACAGCATCTTCCAAAATAGCGA
20[259]21[359]	CTCACAACGCCTGTAGTTTTTCG
14[263]13[360]	AACGGCTAAAAATACGTAATGCCACTACTTTCATTCAACTAATG
14[103]13[199]	AACTCGTATTTGCGGAACAAAGAAACCATTTAGCCAGCAAAAT
19[264]19[359]	CAACTTTCAACATTTCTTTACCCCTGAC
16[359]16[264]	TAGCGTCCAATATTTTCAGCTTGCTTTC
18[199]18[104]	CCCTCAGAACCGTTTCGCTGAGAGCCA
18[103]17[195]	GCAGCAAACAACAGTTGAAAGGAATTGATTTAATCACCG
22[99]24[204]	CTGATGGCCAACAGAGTTTTCAGTCTCTGAACAGT
22[259]23[359]	GGAACCTATTTTCAGGTTTAAAT
19[424]19[515]	ATCAATATGATATTTTCGGAATTT
26[419]27[519]	TCAATTGACCATTAGATTTTAGC
16[583]15[35]	ATAGCTGTGCATAAAGTGAAAGCCTGGTTTAAACCGT
19[104]19[195]	CTGCAACAGTGCTTTACCACCCT
20[527]20[420]	ACAGCGGATCATTTTGCAATGCC
26[579]27[39]	GCAGGTCAGCAGCAACTTTTAAA

14[359]14[264]	CCTCGTTTACCATTTAACGAGGGTAGC
20[579]22[44]	ACGACCAGCGGTGCCGTTTTCCGCCGCGCTTGCTT
22[579]24[44]	GTGTGCTCGTCATAAATTTTTAGAATCAGAGACAG
14[199]14[104]	AGCAGCACCGTATTTAAACAATTCGAC
20[99]22[204]	CCTAATTAGTCTTTAATTTTAGGTTGAGGCAAATG
12[39]12[584]	GTTCCGAAATCGTTTCCAACGCGCGGG
24[579]26[44]	AGGCAGGTGTCCAGCATTTTATTAAAGGGATGCCA
26[203]26[100]	AGTGCCCTTTTAGAACTCA
26[43]26[580]	CCGAGTATTTTTGCCAACG
16[103]15[195]	AATATCTTATTTAGAAGTATTAGACTTTTTAATCAAGT
14[583]13[39]	GAGCTAACGCCAGCTGCATTAATGAATCTTTAAATCAAAGAA
22[43]22[580]	TCCTCGTTTTACTGTT
18[263]17[359]	AGAATAGAGCCTTAATTGTATCGGTTTTTTAAATATTCATT
14[519]14[424]	TGGGAAGGGCGATTTAACGTTAATATT
22[523]22[420]	AAAAAATTTTGTAATACT
20[47]20[580]	AACCACCACATTTTGCATCAG
24[203]24[100]	AAGCGTCTTTTTCATGGAA

Edge Passivating Staple

Start/End	Sequence
12[27]13[27]	GCAAAATTTTTTTTTCCCTTAT
18[187]19[187]	CCACCTTTTTTTTTTCAGAGCC
14[27]15[27]	ACGTCAATTTTTTTTTAGGGCGA
18[507]19[507]	ATGTTATTTTTTTTTCCAGTCC
16[347]17[347]	CTGCGGATTTTTTTTTATCGTCA
12[347]13[347]	ATTTAGGTTTTTTTTAATACCA
14[507]15[507]	TCGGTGCTTTTTTTTTGGGCCTC
16[507]17[507]	CGTTGTATTTTTTTTTAAACGAC
18[27]19[27]	GAAGAAATTTTTTTTGCAGAAAG
14[187]15[187]	ATCAGTATTTTTTTTTGCGACAG
14[347]15[347]	GACGACGTTTTTTTTATAAAAA
16[27]17[27]	TAAATCGTTTTTTTTGAACCCT
12[187]13[187]	CATTTGGTTTTTTTTGAATTAG
12[507]13[507]	TCGCACTTTTTTTTTCCAGCCA
18[347]19[347]	ATCAAAATTTTTTTTTATCAGGT
16[187]17[187]	CTTTTCATTTTTTTTTAATCAA

Fluorophore and Thiolated Staple

Start/End	Sequence
20[399]18[387]	ATTCAAAAAAGATTAACCAGACTTTGA-TAMRA Thiol-GTGGAAAGTGCAATC

2. Zelos Dynamic Platform

Core Staple Strands

Start	End	Sequence
37[92]	0[80]	CGCATGATATAAGTAAATATCCATAGCAAACCC
33[84]	4[92]	ATTTTATTACCTTACATTGGCAGATTAGAA
25[212]	12[220]	CACCAAAGTAAAAAAGCTTAAATTTCTGTAC
12[83]	29[91]	ACCACTAAATCGGAACCCAAGGAGCGGGTT
34[143]	33[143]	TTTTTTAATATATTCCTTATCCAGAGATTTTT
12[251]	29[243]	CAAAGGACAGATACTTAGCCGGAACGAGCGGA
33[212]	4[220]	CGATTCTTCGCTTCGCACTCCAGCCAGGAC
4[187]	36[176]	TCAACCACCAGATTCACAAACAATTTTT
22[227]	19[239]	AGCCACAAAAGGGCGACATTCCAAAAGGCATAACCC
7[100]	30[108]	TTCTTCCAGACGGGCAGAGGCATTTTCGCTAG
11[236]	26[228]	TGCAGGTCAGGATTAGAGAGCTCATTTGGATA
29[116]	8[124]	AAGGCGAGAAAGAACGTGCTTTCCTCGTGCGG
27[176]	10[188]	TTTTTCAGGGAAGCTCTTTTTTTTTTTGGGATTGGCTTAGAGCCTTT
21[92]	16[84]	TGATGCCGAACAAAAGTTACAAACAGAATTG
19[240]	21[251]	TCGTTTACCAGACGACAAAAGAAGTTGAG
4[123]	37[115]	GATATTGCGGGACCTTAAATCAAGATTAAGT
26[267]	15[259]	GCTGATAGCTTCTTTTTTTTTTTTTCGAAAAAATCCCGAAAT
12[276]	26[260]	TTTTTAAAGCGAACCAGACCGACATCGACACCT
30[235]	11[227]	ACTAGCCAAGCTAACGTACAGCGCCATGATGT
29[212]	8[220]	TTATGTCCCGGAGACGTTGTAACGATTT
33[176]	4[188]	TTTTTCCGATGTGCTGTTTTTTTTTTAGGGGACGACGACAGTTATT
8[251]	33[243]	AGTAACAGAGGCCGCTTTTGCGGGATCGCCAT
26[99]	15[107]	AATAGAAAACAAAATTAATTATCGGGAGCCAG
25[92]	12[84]	TCAATATGTGAGTGAATAAAAAGACGCAAAA
8[276]	30[260]	TTTTTGATTCCCAATTCTGCGCCACGGGACCAT
25[252]	12[244]	TTCCAAGAGTAATCTTGACTTGAAAGACTCC
29[252]	8[244]	TCATCGGGTAAAATACGTAACAACGGCTGATT
20[63]	21[55]	GCAATTCATCAATATATTTGGATT
0[79]	38[68]	TCAATCAATATCTGGTTAGGAGCATTTT
11[204]	26[196]	TATACTTTTGATAAGAGGTCGCAGAAACCTGC
8[59]	33[51]	GTGTTGAGAATCGAACGCGCCTGTTTATTAAG
29[220]	8[212]	AGCCCAACCTAAAACGAAAGAGCCGCAATG
4[59]	37[51]	ATTAATCAGATAGCTAACGAGCGTCTTTAAAT
34[267]	7[259]	TTTTGCCAAGCATTTTTTTTTTAAATTATTCGCCATTCAGGC
15[32]	16[32]	TTTTTAACATTGTGCCTGTCATCATTTTTTTT
26[143]	25[143]	TTTTTGAGCAAATTACTTTGAGAAACATTTTT
34[259]	7[276]	CGTTACCGATATATTCGGTTCGAGGGAGAATTAGCATTTTTT
30[227]	11[235]	GGCAGCGAAACAAAGTACAAGCGCAGACAATA
22[107]	19[99]	AGTATCCACACTCAATCCGCCGGGCTATG
26[107]	15[99]	CATAATAGGGTTTTACCGCCTGGCCCTATTG
15[100]	22[108]	GGCGAAACAATAAATTGCGTAGATTTTCGAAA
30[107]	11[99]	AAAAGCACGTATGAAGGGAAGAAAGCGATAAA
0[219]	38[236]	ATCACGTACCAGTACAACTACAACGCCTT
8[83]	33[91]	ACGTTAACCGTTGTAGCACAGAACAACGA
3[108]	34[100]	AGAGCTGACCTGAAAAGCGTACACCAGTCCGCA
38[227]	3[235]	GTGCATTTACCGTTCCAGTATCTGTATGTAAT
15[76]	22[68]	GGGGTGCCTCACTGCCCGCAGCGGAATAACC

Appendix

18[276] 20[260] TTTTTCGAGAGGCTTTTGCAGATAAAAATTCA
33[124] 4[116] TTCCAAGAACGGGTATTAACTCCCGACGAAC
30[259] 11[276] TAAACGCCTGATAAATTGTGCGACCTGCTCATTCCATTTTT
21[84] 16[92] AACTTCATAGCGTGAAATTGTTATCCTCAC
12[243] 29[251] AACAACTAAAGTACGGTGTCCGGAACATGTA
26[235] 15[227] ACCGCCGCCAGCGGCGCCTTTAGTGATCAAA
30[99] 11[107] TGTTATACCGACCGTGTGATTTAGGTTGGCCC
12[115] 29[123] AGAATTTAGAGCTTGACGGGAACGTGGCGTT
38[119] 0[112] GCGGATAATCAGGAGGAGCTCATT
33[92] 4[84] GCATTCGAGAACAAGCAAGTATTCTATGGC
4[251] 37[243] GCTAGAATAGAAGTTAGTAAATGAATTTAGCG
0[207] 1[199] CCGGTTGATAATCAGAATTGACCG
2[276] 3[259] TTTTGTAGACAGTCAAATCACCGGT
3[32] 4[32] TTTTGTAGACTTGAACCTGCGCTACAAATTTTT
7[76] 30[68] CAAAGTACGCCAGAATCCTGTGCGCCGCTTCT
37[212] 0[220] GCAGGCCACGTTAGGTGGAGAGGGTATCA
15[108] 22[100] GGTGTAATGAGTGAGCTAACGCTCACAAAGCA
17[171] 24[176] TTTTGTCTCGCTGCGCAGAAAAATCATTAGCAAGAGAATCAAGTTTTTTT
11[260] 26[268] AGTTTCCATGTTGAACGGTGTACAGACCGCTG
17[32] 16[60] TTTTTTTCGGAACAAAGAAACCACAGAAGGTTTC
9[32] 10[32] TTTTCTTTGCCACCAGTAACCCGAACTTTTT
25[84] 12[92] AACATGCAGCAATAAATCAAAAGAATAAAG
13[32] 14[32] TTTTTAAAAGTCTGTTAAATCTTGAGTTTTTT
29[176] 8[188] TTTTATCGTGGTGAATTTTTTTTTTAAGTTGGGTAACGCCATATT
37[252] 0[240] GGCTTTTAACGGGGTCAAGTGCCTGTAGCAACGGTAA
26[203] 15[195] AAAGAGCGGATCACGATGCTGATTGCCGCTAT
15[196] 22[204] TATAGTAGCGACGCCGGAACGTCACCACCAG
34[107] 7[99] GTACACACGACCCCTTGCTGGTAATATCATA
22[75] 20[64] AGGATATCCTGTTGTTTCATCATATCCATGTACCGCCGGGATG
3[228] 34[236] TGAGGGATTTTGCTTCAACAGTTTCAGAAGG
22[67] 19[79] GAGGATAACGGAATACCAAGAGGATCCAGCTCGAA
11[228] 29[211] TTTAGGTCAATCATAAGCCCTTATTGCGA
33[116] 4[124] GGCTACTATCGGAGTAATAAAAGGGACACAGA
33[220] 4[212] GCGCCTTAATTGTATCGACAGGAGGTAAT
38[75] 3[67] ACGACTAACAACTAGAGCCGTCAATAGACGCC
4[83] 37[91] ACAGAACGAACCACCAGCATGAAAAAGAAG
30[267] 11[259] GTTTACGCAGTTTTTTTTTTTTTATAAGATAACCTCACTGGA
0[91] 38[108] ATATCCCGGAATAGGTGTATCACCGTACGTGC
29[124] 8[116] AAATACCGGAATCATAATTAAGCCAGTATAAA
37[84] 0[92] CAGGTCTAGATTAATAAAGCATCACCTCAA
16[211] 25[219] AACGCAAAGCGGATTGCATGAAGGGTAGAA
26[259] 15[276] TCATAACTTTAATCATTGTGTGCGATTTGTTTTAATTTTT
6[187] 34[176] GGGGCCAGTGAATCGAGCCAGAATTTTT
29[244] 8[252] GATTATCGGCGATTAGAGGTTGAGCCGAACG
19[208] 21[219] GTGCCGGTTAAGAGCAGCGTGGGCCA
8[115] 33[123] CAGGTAATAACATCACTTGCGAACCTCAAGTCT
12[219] 26[236] CTTTATAGGGAACCGAACTGACCAACTAAGA
4[243] 37[251] GGTTAGGTAAAGATTCAAAAATCAATATACAT
15[68] 22[76] CAACATACCAAGAAATTTTGCACGTACAGA
3[100] 34[108] GATATTTGCACCAGGCGTTTTAGCGAACCCAA

Appendix

20[119] 16[124] GCGTGCCTGCAGTATGGCTTTCGCAACATACGAGCCGGAATAAA
19[80] 21[91] TTCGTAATCATGCGGGCGGTTGGGGCA
8[123] 33[115] GAGCATAAGAGACCGACAAAAGGTAAAGAATC
16[251] 25[243] TTCACAACATTAGGCTCATTATACCAAGTGA
8[187] 32[176] TTCAGCCACCACCACCCTCAGAGTTTTT
25[176] 12[188] TTTTTTGCAACGCGGTTTTTTTTTTTTCACGGAAAAAGAGACATTT
22[203] 19[199] CAAACAGAGCACTGGTCAGCAGCAACCGTTACCTGC
11[68] 26[76] GTGCAATCCAATAGCGATAGCTTAGATTCTT
25[244] 12[252] TGGTGCCGCACAAGTTGGGCGGTTGTGTGAAG
7[228] 30[236] CATTAGCAGCGAATCGGAACGAGGGTAGTGCC
12[91] 29[83] GCGGTGAGAAGAACTATATGTAAATGATT
19[100] 21[83] AGCCCGTCCGTGAGCCTCCTCACAGTTAAG
8[211] 33[219] GTCAATTCTACTAATAGTAGCGGGCCAGTT
7[32] 8[32] TTTTTTCGTATGAGGCTCAGTTAAATCTTTTT
33[252] 4[244] CATAGAAAATCTCAAAAAACGGAGTGAAATC
8[51] 33[59] ATAACACCGAGTAAAAGAGTGAAAAACGAAC
11[108] 26[100] CCGACGTGGACTCCAACGTCAGCCCGAGAATC
7[236] 30[228] TCCATTGACCATTAGATACACGGCCAGTCGAA
38[107] 3[99] CGTCAACGCCATTGAGAGCCAGCAGCAAAGAA
25[124] 12[116] TTCACTTTTTAATGGAACTCAAAATCTTAA
16[83] 25[91] CGTAGAGGCGGTTTGCCTGAGAGAGTAACA
37[60] 0[32] TTACTTAACGTCAAAAATGATACAAAATAAATCAACAGTTGAAAGGATTTTT
30[203] 11[195] GCAACCAGTCACATTTGTGAGAGATAGATTAA
8[91] 33[83] AGACGTAATTTAACGACAATAAACACCTA
29[60] 8[52] AATTAGTATAAAGCCAACGCGGCTTAATTTTT
16[59] 25[51] CAGTCCATATCATTACAAAATCGCGCAGTTCA
22[235] 19[227] CCGAACTGTAATAGGGGTGTAGAACGTCAACA
8[243] 33[251] TAGTATAAATCATACAGGCAAGGCTGCGCACG
12[211] 29[219] GCTCATGCTGTAGCTCAACTTTACCAACCA
21[244] 16[252] CGATTTTGCCAGAGTAAAATGTTTAGACAATA
19[228] 21[211] CTATAATTACGAGGCATAGGCCCTGTTAC
26[67] 15[75] AAATGAGCAAAAAGAAGATGATGCTTTGAGCGC
4[91] 37[83] TACGAGAACGCGCAGCTACAATTTTATAAA
7[260] 30[268] AAAGTTAAAGGCTTTGAGGACTAAAGACGGAA
22[127] 16[116] CCGAAGCCCTTTTTAAAGGTTTAAGGGG
29[84] 8[92] TAATGGCGCTAGCGTACTATGGTTGCTTTT
11[100] 26[108] GGGAGGTTATATGTCAATAGTGAATTTAAGTA
37[220] 0[208] TGACCGTATAAACAGTTACTGAGTTTTATGTACC
20[259] 21[243] ACTAATGCAGATACATAACGCAAC
21[220] 16[212] AAGATTTGGGAATTAGAGATGAAACCAGAA
25[116] 12[124] TTAAGATTGCCCGAGTGTGTTCCAGTTGTCC
3[68] 34[76] ATTATTACCAACTAGAAGGCTTATCCGGCCGT
14[187] 26[176] GGCACCTGAATATCAGTTAGCGTTTTTT
21[252] 16[244] GGAGAAGGTGAATTACACCTAACGGAATTGA
38[235] 3[227] GAGTTGAGAGATACCGTTCTAGCTGATATGCC
34[75] 7[67] TTTTTGATTATGCCAGCCATTGCAACACTGT
37[116] 1[119] AACATGCCACGCCAAAAATA
38[99] 3[107] GGGTTTAGACGGGAGAATTAGTTGCTATAAAC
4[276] 34[260] TTTTTATAAAGCCTCAGAGCAGGCAAAGCTTCA
3[260] 34[268] GAGATTCCAGACAGGAACAATAAAGGAATAA

Appendix

22[99] 19[119] GATATAAGACTCCTTATTACGTTCTTCGGGGTCACTGTTGCCCT
4[51] 37[59] TTAAGATAGCCCTAAAACATTAATACATGCCT
25[60] 12[52] ACCTCGTCGCTATTAATTAAGAATCCTTCGTG
32[143] 31[143] TTTTTGATAACAAGTAATATAACCACAATTTTT
34[99] 7[107] CTCAGTAGAAACCAATCAATTAATTCTGTGGA
0[239] 38[228] TCGTAAAAC TAGCATGGCTATTTTAACA
16[219] 25[211] GTTCATCTCTAAAAAGATAGCAGCACGAAA
16[115] 25[123] TGCCGTTTTCTTTTCACCACAACAGCTCAAT
16[91] 25[83] ATAAATAAAGAACGGATTCGCCTGATTGA
16[123] 25[115] GCCTCGTCAGATTAACAGTACCTTTTACACAT
25[220] 12[212] CGATTACCCAAATCAACGTTTCGGTCAATT
8[219] 33[211] CGCACACCAGCAAGACCTCAGAACCGATAC
39[200] 3[195] CCGTAACAATGCCCCCTAATGGGATGGTGTAGATGGGCGCTTTT
10[187] 30[176] CTCCACCAACACACTAAGGAACCTTTTT
0[111] 38[100] TTTTAACCAATGAACCTTGCTAGGGAGA
33[244] 4[252] CGCCCAACTGTTCTGGTGCCGAAACCATAAAA
12[51] 29[59] AACCTCAAGTTTTTTGGGGTAGCGGTCAAGTT
16[243] 25[251] ATCCAAGCCGAAAAGACTTCTAAAAAAATTA
7[204] 30[196] ATCAATAACCTGTTTAGCTAGGGTTTTCAAGA
34[203] 7[195] ATCACAGGAAGAATTACGCCAGCTGGCGTGAA
29[92] 8[84] TGAATAGTATCATATGCGTCCAACATAGGA
33[60] 4[52] AAGACGTAGGAATCATTACCGCAAGCAAGTCT
7[68] 30[76] CCATCTAATGCAGCCATATTTAACAACGTATA
33[52] 4[60] TCCTGCTCATGGATTTTGACGCTCAATCGGCT
0[276] 38[260] TTTTTCTGGAGCAAACAAGAGTCAATGCTAAT
26[195] 15[203] TCATAGGCTTGCCCTGACGACGTAATCAGTCA
1[32] 2[32] TTTTTATTGAGGAAGTTAGAAGTATTTTTTT
7[108] 30[100] TTAGAGCCGATTAAGGGATTTGACGAAGCC
22[259] 19[276] ATTAGGAAGGTAAATATTGAATACCACACCAAATTTTTT
38[67] 3[75] TTGTAGAGAGAATAACATAACCTGAATCAAAA
3[76] 34[68] TACCGACAATTTTTTGAATGTCTGAAAATTT
11[76] 26[68] AAGCGTCTATCAGGGCGATGATCGGCAACTGT
3[236] 34[228] GTGTGTACCAAAAACATTATCTTCCGAAAA
38[259] 3[276] AAGTTTTGATGATACAGGAGTGTCGTCTAAGGCCGTTTTT
0[251] 1[276] GATGATCCACAGACAGCCCTCATAGTTTGTACTGGCTGAGAGTTTTTT
3[204] 34[196] TCATTTGCGGGAGAAGCCTTATCGGCCTGCTT
25[52] 12[60] TTTTCGAGGCGATGATGGTGGTCCGAAGCCC
16[51] 25[59] AAACAGCTGCATTAATGAATTTGCCCAAATT
30[143] 29[143] TTTTTGAATTGTAACAAGAAAAGTTAATTTTT
21[200] 19[207] CATATGGTCATCAGACAGCCAGCG
24[143] 23[143] TTTTTATGAAATACAGGAATATAGCAATTTTT
15[204] 22[176] GAAGAGAATGACCATAAATCCCTCCGGCATCACCAGTAGCACCATTATTTTT
23[176] 14[188] TTTTTCCAGTTTTTTCTTTTTTTTTCCGTTCTTACCCTGATTCC
34[195] 7[203] GCTTTTTCTTAAACAGCTTGCCACCCTCTGGC
16[276] 22[260] TTTTTCTGCGGAATCGTCATATGGATAGCATTTC
21[212] 16[220] CAGCTGCTGGTCATCCTCATAACGGAAACA
21[56] 16[52] ATACAATAAAACGCTTCTGAATAAAGAACCTACGGG
7[196] 30[204] AAGGAGAGCCACCGGAACCGCTCCCTCAGAG
37[244] 0[252] TCATGATATTCACTACAAAGGCTATCAGAATC
26[227] 15[235] TTCAGTAGTAAATTGGGCTTCAGGACGTTTAA

34[227]	7[235]	GGAGCCGACAATGACAACAATCACCCCTCAACA
30[67]	11[75]	TACCTCATCTTCTGACCTAACTGATGCACGTA
11[196]	26[204]	TTGCCCATCTTTGCGTTTTTCATCGGCATTAAC
35[176]	37[191]	TTTTCCACGCGTTTGTTTTTTTTTTTGCCAAAGGATAAAAAATCGTAAACAATCCTCA
3[196]	34[204]	TAGACCTTGATAGCCGCCGCCAGCATTGGTTT
15[260]	17[276]	ATCGTAAGAACTTTACAGGTAGAAAGATCGGAAATTGTCCAATATTTTT
37[52]	0[60]	AGCATTGAGGATTATCTAAAATATCTTCAGT
28[143]	27[143]	TTTTTGCCAAACTACGAGAGTAATAATTTTT
12[123]	29[115]	ACTAATAGGTCTCTTTTTAACCTCCGGCAAAT
4[211]	37[219]	ACTTATATTTTAAATGCAAAATTAATTCTC
30[75]	11[67]	CAAATACAGGGCGGGCGCTGGCAAGTGTGCGAG
4[219]	37[211]	CCTGTTGACAATAAAGGCAGGTCAGAAGC
15[228]	22[236]	AAGATGGGAAGACGTTAATAAAACGAACGTCA
15[236]	22[228]	GAGGCCCTCAAATGCTTTAACGTGCCGGCTTG
31[176]	6[188]	TTTTTAGATTTGATTTTTTTTTTTTTCAAGGGGGCGCGAGCAAAG
34[67]	7[75]	TCATAAAATAATATCCCATCATGTTTCAGCACG
34[235]	7[227]	CTCCCACCGTTGGGAAGGGCGATCGGTGTAG
26[75]	15[67]	GCTTAATCCCTTAGCGGTCCACGCTGGTCCGGC
0[59]	38[76]	TGGCAAACAGCCATATTATTTATCCCAAAGAA
12[59]	29[51]	ACTAGAAAACATCGCAAGACAAAGAACGTATA
11[32]	12[32]	TTTTTGTTATTCAAAATCACAATTTTTTTTTT
36[143]	35[143]	TTTTTGTAATTTGAAGGGTTTGAGCGCTTTTT
37[192]	3[203]	TTAAAGCCAGAATGGAACGATTGGACCC
5[32]	6[32]	TTTTTCAATTCCTACAAATAGACAACTTTTT
30[195]	11[203]	ATACTCATCTTTGACCCCAAGCGTTTGTGAA
4[115]	37[127]	CCTTGTGAGGCGGTGAGTATTGCAACAGCCCTGAAC
29[52]	8[60]	TTTTCGCTGCGCCACCCGCCGCTTAAAGAA
12[187]	28[176]	TTGCACTGTAGCTCATAATCAAATTTTT
39[39]	38[39]	TTTTCCAGTATTTGTTTT

Edge Staple Strands

Start	End	Sequence
37[128]	37[143]	AAAGTCAGAGGTTTTT
27[39]	26[39]	TTTTCCTTATTTCTTTT
21[39]	20[39]	TTTTGATTGATCCTTTTT
8[137]	9[137]	TTTTTTCAGATAGAATTTTT
24[281]	25[281]	TTTTTCCTTAAATTATTTTT
26[281]	27[281]	TTTTTCATAGAGGCGTTTTT
28[281]	29[281]	TTTTTATCCGTCGAATTTTT
30[281]	31[281]	TTTTTCATGATTTTTTTTTT
32[281]	33[281]	TTTTTGGCTTGCTGATTTTT
23[39]	22[39]	TTTTGGGTTTGAATTTT
25[39]	24[39]	TTTTAATTAAGGCGTTTT
33[39]	32[39]	TTTTATAGACAACATTTT
6[137]	7[137]	TTTTTTAGAAGTGAATTTTT
20[280]	21[280]	TTTTTAGGAAGATTTTTT
34[281]	35[281]	TTTTTGAATAATTGCTTTTT
31[39]	30[39]	TTTTAGTAGTCAACTTTT
10[137]	11[137]	TTTTTCCGGCGAAAGTTTTT
19[54]	18[54]	TTTTTATCAGTGATTTTTTT

22[281] 23[281]	TTTTAGTTGTCATCTTTT
37[39] 36[39]	TTTTGCCTACCAGATTTT
38[281] 39[281]	TTTTTAACGAAGCGTTTTT
35[39] 34[39]	TTTTCAATAGCGCCTTTT
16[137] 17[137]	TTTTTAAGTGGCATATTTT
22[143] 22[128]	TTTTTTAGCTATCTTA
4[137] 5[137]	TTTTTGCCAATTCTGTTTTT
14[137] 15[137]	TTTTTACGGGGTGAGTTTTT
2[137] 3[137]	TTTTTCCGCCTAACATTTT
12[137] 13[137]	TTTTTCAAGATGGAATTTT
36[281] 37[281]	TTTTTAGTTTTCTAATTTT

Fuel (xbp) and Anti-Fuel (xbp_rc) Staple for 0, 6, 12, 24 and 43 bp distance

Start	End	Sequence
21[121]_1b_0bp		GCATATGCTAGCAAACGTAGAAAATATCACAATCAATAGAAAATT
21[121]_1b_0bp_rc		AATTTTCTATTGATTGTGATATTTTCTACGTTTGCTAGCATATGC
1[120]_1b_0bp		CGACTTGAATTCGCGTCTGGCTGGGAACAAACGGCG
1[120]_1b_0bp_rc		CGCCGTTTGTCCAGCCAGACGCGAATTCAAGTCG
39[121]_1b_0bp		TGTGCACGTTAGTACCGCCACCCTCACCCAATAGGAACCCATGTA
39[121]_1b_0bp_rc		TACATGGGTTCTATTGGGTGAGGGTGGCGGTTACTAACGTGCACA
20[199]_1b_0bp		GATCCAGCGCAGTGTCACTCGGGGTTTCTGCCAGCACCTTGACT
20[199]_1b_0bp_rc		AGTCAAGGTGCTGGCAGAAACCCCGAGTGACACTGCGCTGGATC
0[190]_1b_0bp		AAGCCCCAAAAACAGTTTTTGTAAATCGTTCAGAC
0[190]_1b_0bp_rc		GTCTGAACGATTTAACAAAACTGTTTTTGGGGCTT
38[199]_1b_0bp		TGCCTATTTGGAACCTATGGGTTTTGCTCAGTACCAACGTA
38[199]_1b_0bp_rc		CAGTACGTTGGTACTGAGCAAACCCATAGGTTCCGAAATAGGCA
18[190]_1b_0bp		AAGAATGCCAACGGCGGTCATTGCAGGCAACGCTTG
18[190]_1b_0bp_rc		CAAGCGTTGCCTGCAATGACCGCCGTTGGCATTCTT
19[120]_1b_0bp		TGAGGTTTCGCGGCTGGTAATGGGCATCAGATGCCGG
19[120]_1b_0bp_rc		CCGGCATCTGATGCCATTACCAGCCGCGAACCTCA
21[121]_1b_6bp		GCATATGCTAGCAAACGTAGAAAATACATTTGTCACAATCAATAGAAAATT
21[121]_1b_6bp_rc		AATTTTCTATTGATTGTGACAAATGTATTTTCTACGTTTGCTAGCATATGC
1[120]_1b_6bp		CGACTTGAATTCGCGTCTGGCCTTCCGTGGGAACAAACGGCG
1[120]_1b_6bp_rc		CGCCGTTTGTCCACGGAAGGCCAGACGCGAATTCAAGTCG
39[121]_1b_6bp		TGTGCACGTTAGTACCGCCACCCTCAGAAAAGCCCAATAGGAACCCATGTA
39[121]_1b_6bp_rc		TACATGGGTTCTATTGGGCTTTTCTGAGGGTGGCGGTTACTAACGTGCACA
20[199]_1b_6bp		GATCCAGCGCAGTGTCACTGCGTACCGGGGTTTCTGCCAGCACCTTGACT
20[199]_1b_6bp_rc		AGTCAAGGTGCTGGCAGAAACCCCGGTACGCAGTGACACTGCGCTGGATC
0[190]_1b_6bp		AAGCCCCAAAAACAGGAAAAATTTTTGTAAATCGTTCAGAC
0[190]_1b_6bp_rc		GTCTGAACGATTTAACAAAAATTTTCTGTTTTTGGGGCTT
38[199]_1b_6bp		TGCCTATTTGGAACCTATTATGCGGGGTTTTGCTCAGTACCAACGTA
38[199]_1b_6bp_rc		CAGTACGTTGGTACTGAGCAAACCCCGCATAATAGGTTCCGAAATAGGCA
18[190]_1b_6bp		AAGAATGCCAACGGCAGCCGGGTCATTGCAGGCAACGCTTG
18[190]_1b_6bp_rc		CAAGCGTTGCCTGCAATGACCCCGGCTGCCGTTGGCATTCTT
19[120]_1b_6bp		TGAGGTTTCGCGGCTGGTAATGGGTAACGGCATCAGATGCCGG
19[120]_1b_6bp_rc		CCGGCATCTGATGCCGTTACCATTACCAGCCGCGAACCTCA
21[121]_1b_12bp		GCATATGCTAGCAAACGTAGAAAATACATCAATTTTGTACAATCAATAGAAAATT
21[121]_1b_12bp_rc		AATTTTCTATTGATTGTGACAAATGTATGATTTTCTACGTTTGCTAGCATATGC
1[120]_1b_12bp		CGACTTGAATTCGCGTCTGGCCTTCTTCTCCGTGGGAACAAACGGCG
1[120]_1b_12bp_rc		CGCCGTTTGTCCACGGAGAAGGAAGGCCAGACGCGAATTCAAGTCG

Appendix

39[121]_1b_12bp TGTGCACGTTAGTACCGCCACCCTCAGAACCGAGCAAGCCCAATAGGAACCCATGTA
39[121]_1b_12bp_rc TACATGGGTTCTATTGGGCTTGCTCGGTTCTGAGGGTGGCGGTACTAACGTGCACA
20[199]_1b_12bp GATCCAGCGCAGTGTCACTGCGCGCTCATAACGGGGTTTCTGCCAGCACCTTGACT
20[199]_1b_12bp_rc AGTCAAGGTGCTGGCAGAAACCCCGGTATGAGCGCGCAGTGACACTGCGCTGGATC
0[190]_1b_12bp AAGCCCCAAAAACAGGAAGATATTAATTTTTGTTAAATCGTTCAGAC
0[190]_1b_12bp_rc GTCTGAACGATTTAACAAAAATTAATATCTTCTGTTTTGGGGCTT
38[199]_1b_12bp TGCCTATTTGGAACCTATTATTCTTAGCGGGTTTTGCTCAGTACCAACGTACTG
38[199]_1b_12bp_rc CAGTACGTTGGTACTGAGCAAACCCCGCTAAAGAATAATAGGTTCCGAAATAGGCA
18[190]_1b_12bp AAGAATGCCAACGGCAGCACCCAGCGGGGTCATTGCAGGCAACGCTTG
18[190]_1b_12bp_rc CAAGCGTTGCCTGCAATGACCCCGCTGGGTGCTGCCGTTGGCATTCTT
19[120]_1b_12bp TGAGGTTGCGGGTGGTAATGGGTAAAGTTAACGGCATCAGATGCCGG
19[120]_1b_12bp_rc CCGGCATCTGATGCCGTTAACTTTACCCATTACCAGCCGCGAACCTCA
21[121]_1b_24bp GCATATGCTAGCAAACGTAGAAAATACATACATAAAGGAAGTTTATTTTGTCAACATC
AATAGAAAATT
21[121]_1b_24bp_rc AATTTTCTATTGATTGTGACAAAATAAACTTCCTTTATGTATGATTTTTCTACGTTTGCT
AGCATATGC
1[120]_1b_24bp CGACTTGAATTCGCGTCTGGCCTTCTGTAGCCTCGGATTCTCCGTGGGAAC
AAACGGCG
1[120]_1b_24bp_rc CGCCGTTGTTCCACGGAGAATCCGAGGCTACAGGAAGGCCAGACGCGAATTC
AAGTCG
39[121]_1b_24bp TGTGCACGTTAGTACCGCCACCCTCAGAACCGCCACCCAGGGATAGCAAGCCCAAT
AGGAACCCATGTA
39[121]_1b_24bp_rc TACATGGGTTCTATTGGGCTTGCTATCCCTGGGTGGCGGTTCTGAGGGTGGCGGTACT
AACGTGCACA
20[199]_1b_24bp GATCCAGCGCAGTGTCACTGCGCGCCTGTGCTCACGGTCATAACGGGGTTTCTGCCAGC
ACCTTGACT
20[199]_1b_24bp_rc AGTCAAGGTGCTGGCAGAAACCCCGGTATGACCGTGAGCACAGGCGCGCAGTGACACTG
CGCTGGATC
0[190]_1b_24bp AAGCCCCAAAAACAGGAAGATTGTATAATTCGATTAATTTTTGTTAAATCGTTCAGAC
0[190]_1b_24bp_rc GTCTGAACGATTTAACAAAAATTAATGCGAATTATACAATCTTCTGTTTTGGGGCTT
38[199]_1b_24bp TGCCTATTTGGAACCTATTATTCTGAAACATTAGGATTAGCGGGTTTTGCTCAGT
ACCAACGTACTG
38[199]_1b_24bp_rc CAGTACGTTGGTACTGAGCAAACCCCGCTAATCCTAATGTTTCAGAATAATA
GGTCCGAAATAGGCA
18[190]_1b_24bp AAGAATGCCAACGGCAGCACCGTCGGTCAGCATCAGCGGGTTCATTGCAGGCAACGCTTG
18[190]_1b_24bp_rc CAAGCGTTGCCTGCAATGACCCCGCTGATGCTGACCGACGGTGTGCCGTTGGCATTCTT
19[120]_1b_24bp TGAGGTTGCGGGTGGTAATGGGTAAAGGTTTCAAATCGTTAACGGCATCAGATGCCGG
21[199]_1b_43bp GCATATGCTAGCAAACGTAGAAAATACATACATAAAGGTGGCAGACACCACGGAAT
AAGTTTATTTTGTCAACATCAATAGAAAATT
1[190]_1b_43bp CGACTTGAATTCGCGTCTGGCCTTCTGTAGCCAGCTTTCATCAACAACCCGTCCGA
TTCTCCGTGGGAACAAACGGCG
39[199]_1b_43bp TGTGCACGTTAGTACCGCCACCCTCAGAACCGCCACCCTCAGCCACCCTCATTTTCAGGG
ATAGCAAGCCCAATAGGAACCCATGTA
20[121]_1b_43bp GATCCAGCGCAGTGTCACTGCGCGCCTGTGCACTCTGTGGTGGCCGTTTTACGGTC
ATACCGGGGTTTCTGCCAGCACCTTGACT
0[120]_1b_43bp AAGCCCCAAAAACAGGAAGATTGTATAAGCAAATTTTTGTTAAATTCGATT
AAATTTTTGTTAAATCGTTCAGAC
38[121]_1b_43bp TGCCTATTTGGAACCTATTATTCTGAAACATGAAAGTATTAAGAAGGATTAGGATTA
GCGGGGTTTTGCTCAGTACCAACGTACTG
18[120]_1b_43bp AAGAATGCCAACGGCAGCACCGTCGGTGGTGCCATCCAAGGTGTCCAGCATCA

19[190]_1b_43bp GCGGGGTCATTGCAGGCAACGCTTG
 TGAGGTTTCGCGGCTGGTAATGGGTAAAGGTTTCTTTGCTCGTGTGTGTTTCAGCAA
 ATCGTTAACGGCATCAGATGCCGG

Fluorophore Staples for FRET

36[138]35[136]_FAM [FAM]GAATTGTAACAAGAAAGTTAA
 4[187]36[183]_TAMRA CTCCACCAACACACTAAGGAACC[TAMRA]

Changed Staple Set for FRET Experiments ((w/o) polyT overhangs)

8[187]32[181] TTC AGC CAC CAC CAC CCT CAG AG
 10[132]11[132] CCG GCG AAA G
 6[132]7[132] TAG AAC TGA G
 32[130]32[131] GTA ATA TAC CAC AAG ATA ACA A
 31[181]6[188] AGA TTT CGA TTC AAG GGG GGC GCG AGC AAA G
 28[130]28[131] TAC GAG AGT AAT AAG CCC AAA C
 29[181]8[188] ATC GTG GTG AAA AGT TGG GTA ACG CCA TAT T
 8[132]9[132] TCA GAT AGA A
 12[187]28[181] TTG CAC TGT AGC TCA TAA TCA AA

b. Scaffold Strand Sequence

p8064

AATGCTACTACTATTAGTAGAATTGATGCCACCTTTTCAGCTCGCGCCCAAATGAAAATATAGCTAAACAGGTTATTGACC
 ATTTGCGAAATGTATCTAATGGTCAAACCTAAATCTACTCGTTCGCAGAATTGGGAATCAACTGTTATATGGAATGAACTTC
 CAGACACCGTACTTTAGTTGCATATTTAAAAACATGTTGAGCTACAGCATTATTCAGCAATTAAGCTCTAAGCCATCCGCA
 AAAATGACCTCTTATCAAAGGAGCAATTAAGGTAATCTCTAATCCTGACCTGTTGGAGTTTGCTTCCGGTCTGGTTCGCT
 TTGAAGCTCGAATTAACGCGATATTTGAAGTCTTCGGGCTTCTCTTAATCTTTTGATGCAATCCGCTTTGCTTCTGAC
 TATAATAGTCAGGGTAAAGACCTGATTTTTGATTTATGGTCATTCTCGTTTTCTGAAGTGTAAAGCATTGAGGGGGATT
 CAATGAATATTTATGACGATTCCGCGAGTATTGGACGCTATCCAGTCTAAACATTTTACTATTACCCCTCTGGCAAACTTCT
 TTTGCAAAAGCCTCTCGCTATTTTGGTTTTATCGTCGTCTGGTAAACGAGGGTTATGATAGTGTGCTTACTATGCCTCG
 TAATTCCTTTTGGCGTTATGTATCTGCATTAGTTGAATGTGGTATTCCTAAATCTCAACTGATGAATCTTTCTACCTGTAATA
 ATGTTGTTCCGTTAGTTTCGTTTTATTAACGTAGATTTTTCTCCCAACGTCCTGACTGGTATAATGAGCCAGTTCTTAAATC
 GCATAAGGTAATTCACAATGATTAAGTTGAAATTAACCATCTCAAGCCAAATTTACTACTCGTTCGGTGTTCCTCGTCA
 GGGCAAGCCTTATTCACTGAATGAGCAGCTTTGTTACGTTGATTTGGGTAATGAATATCCGGTCTTGTCAGATTACTCTT
 GATGAAGGTCAGCCAGCCTATGCGCCTGGTCTGTACACCGTTCATCTGTCTCTTTCAAAGTTGGTCAGTTCGGTTCCTTA
 TGATTGACCGTCTGCGCCTCGTTCCGGCTAAGTAACATGGAGCAGGTCGCGGATTCGACACAATTTATCAGGCGATGATA
 CAAATCTCCGTTGACTTTGTTTCGCGCTTGGTATAATCGCTGGGGGTCAAAGATGAGTGTGTTTAGTGTATTCTTTGCCTCT
 TTCGTTTTAGGTTGGTGCCTTCGTAGTGGCATTACGATTTTTACCGTTAATGGAACTTCTCATGAAAAAGTCTTTAGTC
 CTCAAAGCCTCTGTAGCCGTTGCTACCCTCGTTCGATGCTGCTTTTCGCTGCTGAGGGTGACGATCCCGCAAAAGCGGCC
 TTTAACTCCCTGCAAGCCTCAGCGACCGAATATATCGGTTATGCGTGGGCGATGGTTGTTGTCATTGTGCGGCGCAACTATC
 GGTATCAAGCTGTTAAGAAATTCACCTCGAAAGCAAGCTGATAAACCGATACAATTAAGGCTCCTTTTGGAGCCTTTTTT
 TTGGAGATTTCAACGTGAAAAAATTATTATCGCAATTCCTTTAGTTGTTCTTTCTATTCTCACTCCGCTGAACTGTTGA
 AAGTTGTTTAGCAAAATCCCATACAGAAAATTCATTTACTAACGCTCGAAAGACGACAAAACCTTTAGATCGTTACGCTAAC
 TATGAGGGCTGTCTGTGGAATGCTACAGGCGTTGTAGTTTGTACTGGTGACGAACTCAGTGTACGGTACATGGGTTCTCT
 ATTGGGCTTGTATCCCTGAAAATGAGGGTGGTGGCTCTGAGGGTGGCGGTTCTGAGGGTGGCGGTTCTGAGGGTGGCG
 GACTAAACCTCTGAGTACGGTGATACACCTATTCCGGGCTATACTTATATCAACCCTCTCGACGGCACTTATCCGCCTGG

TACTGAGCAAAACCCCGCTAATCCTAATCCTTCTCTTGAGGAGTCTCAGCCTCTTAATACTTTCATGTTTCAGAATAATAGGT
TCCGAAATAGGCAGGGGGCATTAACTGTTTATACGGGCACTGTTACTCAAGGCACTGACCCCGTTAAAACCTTATTACCAGT
ACACTCTGTATCATCAAAAGCCATGTATGACGCTTACTGGAACGGTAAATTCAGAGACTGCGCTTTCATTCTGGCTTTAA
TGAGGATTTATTTGTTTGTGAATATCAAGGCCAATCGTCTGACCTGCCTCAACCTCCTGTCAATGCTGGCGGCGGCTCTGGT
GGTGGTTCTGGTGGCGGCTCTGAGGGTGGTGGCTCTGAGGGTGGCGGTTCTGAGGGTGGCGGCTCTGAGGGAGGCGGT
TCCGGTGGTGGCTCTGGTCCGGTGATTTTGATTATGAAAAGATGGCAAACGCTAATAAGGGGGCTATGACCGAAAATGC
CGATGAAAACGCGCTACAGTCTGACGCTAAAGGCAAACCTTATTCTGTGCTACTGATTACGGTGTCTATCGATGGTTT
CATTGGTGACGTTTCCGGCCTTGCTAATGGTAATGGTGTACTGGTATTTTGTGGCTCTAATCCCAAATGGCTCAAGTC
GGTGACGGTGATAATTCACCTTAATGAATAATTTCCGTCAATATTTACCTCCCTCCCTCAATCGGTTGAATGTCGCCCTT
TGCTTTGGCGCTGGTAAACCATATGAATTTCTATTGATTGTGACAAAATAAATTTATCCGTGGTGTCTTTCGTTTCTT
TATATGTTGCCACCTTATGTATGATTTTCTACGTTTGTAAACATACTGCGTAATAAGGAGTCTTAATCATGCCAGTCTTTT
GGGTATCCGTTATTATTGCGTTTCCCTCGGTTTCTTCTGGTAACTTTGTTCCGGCTATCTGCTTACTTTTCTAAAAAGGGCTT
CGGTAAGATAGCTATTGCTATTTTATTGTTTCTTGTCTTATTATTGGGCTTAACTCAATTTGTGGGTTATCTCTGATAT
TAGCGCTCAATTACCCTCTGACTTTGTTTCAAGGGTGTTCAGTTAATTTCTCCCGTCTAATGCGCTTCCCTGTTTTATGTTATTCT
CTCTGTAAAGGCTGCTATTTTCAATTTTACGTTTAAACAAAAAATCGTTTCTTATTGGATTGGGATAAATAATATGGCTGT
TATTTTGTAACTGGCAAATTAGGCTCTGAAAGACGCTCGTTAGCGTTGGTAAAGATTCAAGGATAAAATTGTAGCTGGGTGC
AAAATAGCAACTAATCTTGATTTAAGGCTTCAAACCTCCCGCAAGTCGGGAGGTTGCTAAAACGCCTCGCGTTCTTAGA
ATACCGGATAAGCCTTCTATATCTGATTTGCTTGTATTGGGCGCGGTAATGATTCTACGATGAAAATAAAAAACGGCTTG
CTTGTCTCGATGAGTGCAGTACTTGGTTTAAATACCCGTTCTTGAATGATAAGGAAAGACAGCCGATTATTGATTGGTTTC
TACATGCTCGTAAATTAGGATGGGATATTATTTTCTTGTTCAGGACTTATCTATTGTTGATAAACAGGCGGTTCTGCATTA
GCTGAACATGTTGTTTATTGTCGTCGCTGGACAGAATTACTTTACCTTTTGTGCGTACTTTATATTCTTATTACTGGCTCG
AAAATGCCTCTGCCTAAATTACATGTTGGCGTTGTTAAATATGGCGATTCTCAATTAAGCCCTACTGTTGAGCGTTGGCTT
ATACTGGTAAGAATTTGTATAACGCATATGATACTAAACAGGCTTTTCTAGTAATTATGATTCCGGTGTTTATTCTTATTTA
ACGCCTTATTTATCACACGGTCCGATTTTCAAACCATTAATTTAGGTGAGAAGATGAAATTAATAAATAATATTTGAAAA
AGTTTTCTCGCTTCTTGTCTTGCATTGGATTGTCATCAGCATTTACATATAGTTATATAACCAACCTAAGCCGGAGGTT
AAAAAGGTAGTCTCTCAGACCTATGATTTTGATAAATCACTATTGACTCTTCTCAGCGTCTAATCTAAGCTATCGCTATGT
TTTCAAGGATTCTAAGGGAAAAATTAATAATAGCGACGATTTACAGAAGCAAGGTTATTCACTCACATATATTGATTTATGT
ACTGTTTCCATTAATAAAGGTAATTCAAATGAAATTGTTAAATGTAATTAATTTGTTTCTTGATGTTTGTTCATCATCTTC
TTTTGCTCAGGTAATTGAAATGAATAATCGCCTCTGCGGATTTTGTAACTTGGTATTCAAAGCAATCAGGCGAATCCGTT
ATTGTTTCTCCCGATGTAAGGTAAGTACTGTTACTGTATATTCTGACGTTAAACCTGAAAATCTACGCAATTTCTTATTTCT
GTTTTACGTGCAAATAATTTGATATGGTAGGTTCTAACCTTCCATTATTCAGAAGTATAATCAAACAATCAGGATTATAT
TGATGAATTGCCATCATCTGATAATCAGGAATATGATGATAATCCGCTCCTTCTGGTGGTTTCTTGTTCGCAAAATGAT
AATGTTACTCAAACTTTTAAATTAATAACGTTCCGGGCAAAGGATTAATACGAGTTGTCGAATTGTTGTAAAGTCTAATA
CTTCTAAATCCTCAAATGTATTATCTATTGACGGCTCAATCTATTAGTTGTTAGTGCTCCTAAAGATATTTAGATAACCTTC
CTCAATTCCTTCAACTGTTGATTTGCCAACTGACCAGATATTGATTGAGGGTTTGATTTGAGGTTCAAGGTTAGGTTAGTGC
TTTAGATTTTCAATTTGCTGCTGGCTCTCAGCGTGGCACTGTTGCAGGCGGTTAATACTGACCGCCTCACCTCTGTTTTAT
CTTCTGCTGGTGGTTCGTTCCGATTTTTAATGGCGATGTTTTAGGGCTATCAGTTCCGCGCATTAAAGACTAATAGCCATTC
AAAAATATTGTCTGTGCCACGTATTCTACGCTTTCAGGTGAGAAGGGTCTATCTCTGTTGGCCAGAATGTCCCTTTATTA
CTGGTCTGTGACTGGTGAATCTGCCAATGTAATAATCCATTTACAGACGATTGAGCGTCAAATGTAGGTATTTCCATGA
GCGTTTTTCTGTTGCAATGGCTGGCGGTAATATTGTTCTGGATATTACCAGCAAGGCCGATAGTTTGTAGTTCTTACTCA
GGCAAGTGATGTTATTAATAAAGGAAGTATTGCTACAACGGTTAATTTGCGTGATGGACAGACTTTTTACTCGGTGG
CCTCACTGATTATAAAAAACACTTCTCAGGATTCTGGCGTACCCTTCTGTCTAAAATCCCTTAATCGGCCTCCTGTTTAGCT
CCCGCTCTGATTCTAACGAGGAAAGCACGTTATACGTGCTCGTCAAAGCAACCATAGTACGCGCCCTGTAGCGGCGCATT
AGCGCGGCGGGTGTGGTGGTTACGCGCAGCGTGACCGCTACACTGCCAGCGCCCTAGCGCCCGCTCCTTTCGCTTCTTC
CCTTCTTCTCGCCACGTTCCGGCTTTCCCGTCAAGCTCTAAATCGGGGCTCCCTTATAGGTTCCGATTTAGTGCTTT
ACGGCACCTCGACCCAAAAAATTTGATTTGGGTGATGGTTCACGTAGTGGGCCATCGCCCTGATAGACGGTTTTTCGCC
TTTGACGTTGGAGTCCACGTTCTTTAATAGTGGACTCTTGTCCAACTGGAACAACACTCAACCCTATCTCGGGCTATTCTT
TTGATTTATAAGGGATTTTCCGATTTCCGAACCAACATCAAACAGGATTTTCCGCTGCTGGGGCAAACAGCGTGGACCG
CTTGCTGCAACTCTCTCAGGGCCAGGCGGTGAAGGGCAATCAGCTGTTGCCGCTCACTGGTAAAAGAAAAACCACCC
TGCGGCCAATACGCAAACCGCTCTCCCGCGCGTTGGCCGATTCATTAATGCAGCTGGCACGACAGGTTTCCGACTGG

AAAGCGGGCAGTGAGCGCAACGCAATTAATGTGAGTTAGCTCACTCATTAGGCACCCCAGGCTTTACACTTTATGCTTCCG
GCTCGTATGTTGTGTGGAATTGTGAGCGGATAACAATTTACACAGGAAACAGCTATGACCATGATTACGAATTCGAGCTC
GGTACCCGGGGATCCTCAACTGTGAGGAGGCTCACGGACGCGAAGAACAGGCACGCGTGCTGGCAGAAACCCCGGTAT
GACCGTAAAAACGGCCCGCCGATTCTGGCCGAGCACCACAGAGTGACAGGCGCGCAGTGACACTGCGCTGGATCGT
CTGATGCAGGGGGCACCCGGCACCGCTGGCTGCAGGTAACCCGGCATCTGATGCCGTTAACGATTTGCTGAACACACCAGT
GTAAGGGATGTTTATGACGAGCAAAGAAACCTTTACCCATTACCAGCCGAGGGCAACAGTGACCCGGCTCATACCGCAA
CCGCGCCCGCGGATTGAGTGCGAAAGCGCCTGCAATGACCCCGCTGATGCTGGACACCTCCAGCCGTAAGCTGGTTGCG
TGGGATGGCACCACCGACGGTGTGCCGTTGGCATTCTTGGGTTGCTGCTGACCAGACCAGCACCAGCTGACGTTCTAC
AAGTCCGGCACGTTCCGTTATGAGGATGTGCTCTGGCCGGAGGCTGCCAGCGACGAGACGAAAAAACGGACCGCGTTTG
CCGGAACGGCAATCAGCATCGTTAACTTTACCTTCATCACTAAAGGCCGCCTGTGCGGCTTTTTTACGGGATTTTTTAT
GTCGATGTACACAACCGCCAACTGCTGGCGGCAAATGAGCAGAAATTTAAGTTTGATCCGCTGTTTCTGCGTCTCTTTTT
CGTGAGAGCTATCCCTTACCACCGGAGAAAGTCTATCTCTACAAATTCGGGACTGGTAAACATGGCGCTGTACGTTTCG
CCGATTGTTCCGGTGAGGTTATCCGTTCCCGTGGCGGCTCCACCTCTGAAAGCTTGGCACTGGCCGTCGTTTTACAACGTC
GTGACTGGGAAAACCTGGCGTTACCCAACCTAATCGCCTTGCAGCACATCCCCCTTCGCCAGCTGGCGTAATAGCGAAG
AGGCCCGCACCGATCGCCCTTCCCAACAGTTGCGCAGCCTGAATGGCGAATGGCGCTTTGCTGGTTTCCGGCACCAGAA
GCGGTGCCGAAAGCTGGCTGGAGTGCATCTTCTGAGGCCGATACTGTCGTCGTCCTCAAACCTGGCAGATGCACGG
TTACGATGCGCCCATCTACCAACGTGACCTATCCATTACGGTCAATCCGCGTTTGTCCACGGAGAATCCGACGGGT
TGTTACTCGCTCACATTTAATGTTGATGAAAGCTGGCTACAGGAAGGCCAGACGCGAATTATTTTTGATGGCGTTCCTATTG
GTTAAAAATGAGCTGATTTAACAAAAATTTAATGCGAATTTTAAACAAAATATTAACGTTTACAATTTAAATATTTGCTTATA
CAATCTTCTGTTTTGGGGCTTTTCTGATTATCAACCGGGGTACATATGATTGACATGCTAGTTTTACGATTACCGTTCATC
GATTCTTGTGTTGCTCCAGACTCTCAGGCAATGACCTGATAGCCTTTGTAGATCTCTCAAAAATAGTACCCTCTCCGGCAT
TAATTTATCAGCTAGAACGGTTGAATATCATATTGATGGTGATTTGACTGTCTCCGGCCTTTCTACCCTTTTGAATCTTTAC
CTACACATTACTCAGGCATTGCATTTAAAATATATGAGGGTTCTAAAAATTTTATCCTTGCCTTGAATAAAGGCTTCTCCC
GCAAAAGTATTACAGGGTCATAATGTTTTGGTACAACCGATTTAGCTTTATGCTCTGAGGCTTTATTGCTTAATTTTGCTAA
TTCTTGCCTGCTGTATGATTTATTGGATGTT

B. Acknowledgements

First, I would like to thank Prof. Sebastian Schlücker for the opportunity to work in his group during my Master studies as well as my PhD. He revealed to me the fascinating interface between chemistry and biology and gave me the freedom and the support to develop and evolve my project in a new direction and trusted in my abilities.

Furthermore, I would like to thank Prof. Barbara Saccà for fully including me in her working group, she always offered help, time, space, and resources which I was allowed to occupy during my PhD.

Great thanks to all the former and current members of the AG Schlücker and AG Saccà. It was a great pleasure to work with you and many colleagues became good friends during this time.

Special thanks go out to Richard "Ricodico" Kosinski! Without his personal support, zeal, and creativity this PhD would have been different. Also, Oliver Sritharan, Helene Giesler and Michelle Hechler were in every situation helpful and took personal participation in my time and work. I would also like to mention and thank Elisa-Charlott Schöneweiß. Together with Richard, she warmly welcomed me in the AG Saccà, helped me on multiple ways and even during the corona pandemic we had a lot of fun.

To mention all persons who helped me during the last four years is a tough task, but I will try. Thanks go out to Katarina Lohwasser, Roland Grzeschik, Carolin Sanders, Tim Holtum, Jesil Jose, Louisa Waasmann, Thomas Keller, Elzbieta Stepula, Vi Tran, Bernd Walkenfort and Matthias König. I think I asked most of you for something and the discussions with you were fruitful every time. I really learned a lot!

The working (as well as boozing) with members of the AG Saccà lead to impressive results. Thus, I would like to thank Sabrina "Brinka" Gambietz, Andreas "AJ" Jaekel, Pierre"-o" Stegeman, Len(a) Stenke, Sarah Urban and Wolfgang "Pfeiffi" Pfeiffer.

For the administrative support I would like to thank Axel Hoffmann and Jan Neumann.

For the technical support, I would like to thank Dirk Gründer and Jürgen Leistikow who planned and built some complicated devices for my projects and taught me a lot of technical stuff.

I would also like to thank my mother, Heike Fischbach. She conveyed me the affinity to natural sciences at a very early age and never gave up even though I never chose the easy way.

The most important person in my life is my wonderful and charming wife, Viktoria Erkelenz. She is the reason for all my effort since late school and motivated me in every thinkable way to give my best and always going one step further. Without you, I would not be where I am today!

C. List of Publications and Poster Presentations

R. Schirrmann, M. Erkelenz, K. Lamers, O. Sritharan, S. Schlücker, S. Brandau, Gold nanorods induce endoplasmic reticulum stress and autocrine inflammatory activation in human neutrophils, **2022**, *ACS Nano* (**Submitted**)

A. Blümke, K. Ripkens, L. Pedroza, L. Otto, M. Erkelenz, U. Dittmer, S. Schlücker, and M. Ehrmann, The protein quality control factor HTRA1 targets prion-like propagation of aggregated tau, **2022**, *Nature Cell Biology* (**Submitted**)

R. Kosinski, J. M. Perez, E.-C. Schöneweiß, Y. B. Ruiz-Blanco, I. Ponzio, K. Bravo-Rodriguez, M. Erkelenz, S. Schlücker, G. Uhlenbrock, E. Sanchez-Garcia, B. Saccà, The role of DNA nanostructures in the catalytic cycle of a monomeric serine protease, **2021**, *Science Advances* (**Accepted**)

M. Erkelenz, R. Kosinski, O. Sritharan, H. Giesler, B. Sacca, S. Schlücker, Site-specific facet protection of gold nanoparticles inside a 3D DNA origami box: a tool for molecular plasmonics, **2021**, *Chemical Communications*, doi.org/10.1039/D0CC07712G

M. Erkelenz, S. Schlücker, Fundamentals of NanoBioPhotonics for Diagnostics and Therapy, in: Volume 5: Plasmonic Nanoparticles in Diagnostics and Therapy, 2022, *World Scientific*, 3-43, doi.org/10.1142/12236-vol5

M. Erkelenz, S. Wilmsen, K. Lunau, Preference for artificial flowers dependent of its microtexture in honeybees, **2016**, *Entomologie heute* 28: 43-67.

M. Erkelenz, S. Schlücker, Dynamic DNA Origami-Based Gold Nanoparticle Dimerization: Design and Assembly of a Hybrid Platform for Nanophotonics, *CRC 1093: Supramolecular Chemistry on Proteins*, Student and International Symposium, **2021**, Gelsenkirchen, Germany, **Poster**

M. Erkelenz, J. H. Yoon, E. Stepula, V. Tran, M. König, R. Grzeschik, K. Bruderek, S. Brandau, S. Schlücker, Synthesis and Characterization of Small Gold Nanorods for Cellular Uptake by Neutrophil Granulocytes and Use in Photothermal Therapy, *Gordon Research Conferences and Seminars: Cancer Nanotechnology*, **2019**, Boston (MA), USA, **Poster**

M. Erkelenz, R. Kosinski, O. Sritharan, B. Saccá, S. Schlücker, Detection of Protein-Protein Interactions with DNA Origami assisted Dynamic Gold Nanocube Dimerization, *CRC 1093 Symposium, Supramolecular Principles in Biological Systems*, **2019**, Essen, Deutschland, **Poster**

M. Erkelenz, R. Kosinski, E.-C. Schöneweiß, B. Saccá, C. Ottmann, S. Schlücker, Nanopositioning of Supramolecular Ligands on DNA Origami for Multivalent Protein Recognition, *16th World Medical Nanotechnology Congress*, **2018**, Tokyo, Japan, **Poster**

M. Erkelenz, J. H. Yoon, E. Stepula, V. Tran, M. König, R. Grzeschik, K. Bruderek, S. Brandau, S. Schlücker, Synthesis and Characterization of Small Gold Nanorods for Cellular Uptake by Neutrophil Granulocytes and Use in Photothermal Therapy, *116th General Assembly of the German Bunsen Society for Physical Chemistry, Physical Chemistry for Life Sciences*, **2017**, Kaiserslautern, Germany, **Poster + Talk**

M. Erkelenz, S. Wilmsen, K. Lunau, Preference for artificial flowers dependent of its microtexture in honeybees, **2016**, *28. Westdeutschen Entomologentag*, Düsseldorf, Germany, **Poster + Talk**

Publications in preparation:

A. Hackel, R. Madel, S. Vollmer, V. Börger, M. Erkelenz, S. Schlücker, S. Lang, B. Giebel, C. Kirschning, and S. Brandau, Immunological priming upregulates PD-1 ligands on mesenchymal stromal cells and augments therapeutic benefits in experimental GvHD

R. Schirrmann, M. Erkelenz, K. Lamers, O. Sriharan, S. Schlücker and S. Brandau, Modulation of neutrophil functions by gold nanoparticles

D. Curriculum Vitae

Der Lebenslauf ist in der Online-Version aus Gründen des Datenschutzes nicht enthalten.

E. Declaration

Hiermit erkläre ich, gem. § 7 Abs. (2) c) + e) der Promotionsordnung der Fakultät für Chemie zur Erlangung des Dr. rer. nat., dass ich die vorliegende Dissertation selbständig verfasst und mich keiner anderen als der angegebenen Hilfsmittel bedient, bei der Abfassung der Dissertation nur die angegebenen Hilfsmittel benutzt und alle wörtlich oder inhaltlich übernommenen Stellen als solche gekennzeichnet habe.

Solingen, den _____

Unterschrift des Doktoranden

Hiermit erkläre ich, gem. § 7 Abs. (2) d) + f) der Promotionsordnung der Fakultät für Chemie zur Erlangung des Dr. rer. nat., dass ich keine anderen Promotionen bzw. Promotionsversuche in der Vergangenheit durchgeführt habe und dass diese Arbeit von keiner anderen Fakultät/Fachbereich abgelehnt worden ist.

Solingen, den _____

Unterschrift des Doktoranden